JOURNAL OF ENGINEERING RESEARCH & SCIENCES

JENRS

Editorial

In this edition, our journal brings forth a collection of papers showcasing innovative research spanning diverse fields, from architecture and engineering to materials science and biology. Each contribution offers valuable insights into contemporary challenges and presents novel approaches to address them, exemplifying the spirit of interdisciplinary collaboration and innovation.

This paper underscores the pivotal role of Building Information Modeling (BIM) in driving sustainability within the architecture, engineering, and construction (AEC) industry. Through a systematic review, the authors elucidate how BIM tools and processes facilitate environmentally sensitive design, leveraging accelerated performance simulations and green building certification systems. By integrating BIM platforms such as Revit-Insight 360, significant reductions in energy use intensity (EUI) and lifecycle costs are demonstrated, highlighting the potential for widespread mainstreaming of sustainable building practices. However, interoperability challenges remain a hindrance, emphasizing the need for standardized modeling practices and enhanced analytical integration to realize BIM's full potential in guiding sustainable building lifecycles [1].

In the realm of semiconductor manufacturing, the author addresses a critical issue concerning metal corrosion by halogen elements, particularly bromine (Br). While previous studies have focused on fluorine and chlorine contamination, the mechanisms underlying Br-induced aluminium corrosion have received limited attention. Through comprehensive analysis using Auger electron spectroscopy and scanning electron microscopy, the authors unravel the formation of aluminium bromide defects and propose a chain chemical reaction mechanism driving Br-induced corrosion. This study fills a significant gap in our understanding of semiconductor reliability issues, providing valuable insights for mitigating corrosion-related failures in semiconductor devices [2].

Turning our attention to biology, the author delves into the intricate musculature of the Australian lungfish, Neoceratodus forsteri, shedding light on its feeding mechanisms. Through meticulous anatomical examination, the authors elucidate the roles of various muscles associated with jaw movement and hyoid apparatus control, offering a comprehensive understanding of the physiological adaptations facilitating feeding in this ancient fish species. This study enriches our knowledge of vertebrate anatomy and functional morphology, contributing to broader insights into evolutionary adaptations and ecological interactions [3].

Lastly, this paper presents a robust localization algorithm designed for mobile robot navigation in complex indoor environments. The proposed algorithm, named Branch-and-Bound for Robust Localization (BB-RL), integrates global localization, position tracking, and resolution of the kidnapped robot problem within a unified framework. Through innovative approaches such as Finite State Machine (FSM)-based relocalization judgment and loop-closure optimization, BB-RL demonstrates enhanced reliability and accuracy in real-world scenarios. This advancement in robotics promises to revolutionize indoor navigation systems, opening new avenues for autonomous robot deployment in diverse applications [4].

Collectively, these papers represent the forefront of research across various disciplines, offering valuable contributions to their respective fields. As editors, we commend the authors for their dedication to advancing knowledge and fostering innovation, and we look forward to further exploration and collaboration in the pursuit of scientific excellence.

References:

[1]   M. Numan, U. Saadat, M.U. Farooq, "BIM and Sustainable Design: A Review of Strategies and Tools for Green Building Practices," *Journal of Engineering Research and Sciences*, vol. 3, no. 2, pp. 1–7, 2024, doi:10.55708/js0302001.

[2]   H. Younan, L.J. Lois, Z. Lei, L. Binghai, L. Xiaomin, "A Study on the Bromine-induced Corrosion/Defects in Wafer Fabrication," *Journal of Engineering Research and Sciences*, vol. 3, no. 2, pp. 8–14, 2024, doi:10.55708/js0302002.

[3]   A. Kemp, "Jaw and Tongue Muscles in the Australian Lungfish, Neoceratodus forsteri (Osteichthyes: Dipnoi)," *Journal of Engineering Research and Sciences*, vol. 3, no. 2, pp. 15–21, 2024, doi:10.55708/js0302003.

[4]   H. (Yulin) Zhang, Y. Wang, X. Luo, B. Mereaux, L. Zhang, "Robust Localization Algorithm for Indoor Robots Based on the Branch-and-Bound Strategy," *Journal of Engineering Research and Sciences*, vol. 3, no. 2, pp. 22–42, 2024, doi:10.55708/js0302004.

Editor-in-chief

Prof. Paul Andrew

CONTENTS

BIM and Sustainable Design: A Review of Strategies and Tools for Green Building Practices

Muhammad Numan[*][1, 2] (ID)**, Usama Saadat**[1] (ID)**, Muhammad Usman Farooq**[4] (ID)

[1]Civil Engineering Technology, University of Sialkot, Sialkot, 51310, Pakistan

[2]Civil Engineering, University of Engineering & Technology, Lahore, Lahore, 54890, Pakistan

[3]Civil Engineering, The Islamia University of Bahawalpur, Bahawalpur, 63100, Pakistan

[*]Corresponding author: Muhammad Numan, University of Sialkot, +92-302-7204931 & numan.zaheer007@gmail.com

ABSTRACT: Building Information Modeling (BIM) provides a robust foundation for driving sustainability across architecture, engineering and construction (AEC) practices. This paper presents a systematic review of literature elucidating the confluence of BIM tools and processes with accelerated performance simulations and green building certification systems needed to guide environmentally sensitive design. Integrated Revit-Insight 360 is shown to enable 21% lower energy use intensity (EUI) and 8.5% reduced lifecycle costs over baseline for an office building through rapid multi-objective optimization spanning orientation, envelope and HVAC properties. Enhanced integrated platforms perform detailed thermal zoning analysis capturing realistic solar gains and heat storage effects, right-sizing heating equipment by 7.2% over conventional workflows. Further, BIM automation mitigates nearly 50-80% of manual calculations for BEAM Plus, LEED prerequisites and accelerates documentation for certification. However, interoperability issues inhibiting holistic sustainability evaluations persist due to lack of modeling standards. Emerging tools exemplify modular green assessment connecting multi-vendor engines to resolve underlying technical barriers. As BIM object definitions and seamless analytical integration matures, widespread mainstreaming for sustainability is foreseeable. While current measured metrics revolve around energy use, emissions and green certification, future work needs to address social and economic indicators also enabled by data-rich BIMs. Nevertheless, coupled with continuous monitoring for validation, BIM provides the foundation for the AEC industry to progress towards comprehensive sustainable building lifecycles.

KEYWORDS: BIM (Building Information Modeling), Sustainable Design, Green Building Practices, Performance Simulations, Green Building Certification Systems

1. Introduction

Sustainable and green building design has become a strategic priority to mitigate the negative environmental impacts of the building sector. Buildings are responsible for nearly 40% of global energy usage and one third of greenhouse gas emissions annually [1]. As sustainability concerns come to the forefront, there is a paradigm shift in the architecture, engineering and construction (AEC) industry towards holistic building life cycle assessment and integrating resource efficiency across design, construction and operations [2]. To enable buildings to meet sustainability goals, there is growing emphasis on data-driven decision making in early design stages [3].

Building Information Modelling (BIM) has demonstrated immense potential to be the foundation for performing robust sustainability analyses. BIM encompasses the processes and technologies to digitally represent physical and functional characteristics of any built facility across its life cycle [4]. High fidelity BIM models can capture detailed intelligence spanning building geometry, spatial relationships, geographic information, properties of construction materials, as well as project life cycle data in an integrated way [5]. With rich information embedded into semantic BIM objects, multifaceted evaluations can be performed to predict and optimize sustainability performance [6].

The combined strengths of BIM and building performance analysis tools can lead to better informed decisions aligned with green building certification standards. For example, Autodesk Revit allows rapid

energy modelling with Insight 360 to study impacts of design variables including building massing, HVAC zoning, daylighting strategies etc. in iterative fashion [7]. This facilitates data-driven decisions rather than intuitive judgments for greener outcomes. Similar energy simulation abilities have been demonstrated using integrated BIM platforms from vendors like Bentley and Graphisoft through gbXML schemas [8]. Additionally, using quantities tracked within BIM models streamlines the otherwise cumbersome process of documentation for LEED or Green Globes certification [9].

However, sustainability considerations are often an afterthought and BIM capabilities remain underutilized during design stages due to interoperability issues, lack of expertise, higher upfront costs and other barriers [10,11]. As integration between BIM tools and whole building energy/life cycle assessment applications mature, several of these gaps are beginning to narrow. This paper examines the current state of research and practice at the nexus of BIM and sustainable building with emphasis on workflows, analytics, rating systems and implementation case studies. The collective insights pave the path forward for the AEC industry to leverage BIM's data-rich foundation in achieving true sustainability from conception to occupancy.

2. Literature Review

Several studies have investigated BIM applications for energy modelling and simulation to enable data-driven sustainable design. In [12], the authors demonstrated a multi-objective optimization framework leveraging integrated Revit-Insight 360 to assess tradeoffs between cost, energy use and LEED criteria at early stage. Design variants spanning building orientation, wall assemblies, glazing and HVAC systems were rapidly generated and analysed to identify energy-efficient solutions aligning with certification goals. Measured outcomes included return on investment, life cycle cost, annual energy consumption, carbon emissions and targeted LEED credits.

In [13], the researchers established an interoperable workflow connecting Revit, IES VE (Virtual Environment) and Modelica for coupled energy-exergy analyses. The prototyped simulation environment enabled holistic evaluation of building geometry, orientation, construction, HVAC components and control logic on thermal performance. Assessed output metrics spanned heating/cooling loads, air flow rates, exergy destruction and thermal comfort within occupied zones. The integration of BIM-based modelling and simulation tools was shown to create digital environments for sustainable building design.

In [14], the authors reviewed various BIM applications throughout the building lifecycle pertinent to

sustainability practices. Quantified metrics compiled from multiple sources highlight that BIM use led to reduced material waste generation (50-80%) during construction and curtailed lifecycle energy consumption (13-23%) from facility operations. Other benefits included higher achievement of green certification credits, along with shortened project durations and cost savings that recoup initial investments in BIM.

While these case-based analyses demonstrate BIM's potential, In [15] the author, note that model integrity and analytical accuracy is strongly tied to user expertise [15]. A critical review by author [16] also highlights the lack of standards in BIM-based sustainability assessment as a barrier to widespread adoption [16]. As tools mature and data exchange protocols stabilize, BIM is poised to drive sustainability gains across building industry practices.

3. Methodology

This paper aims to systematically review current literature on Building Information Modelling tools, techniques and workflows applied to further sustainability in building design and construction. A comprehensive review is undertaken to synthesize reported findings, critically assess implementation challenges and provide future outlook of this domain.

3.1. Review scope and keywords

Seminal and recent research articles related to application of BIM for sustainable building practices were searched across engineering and architectural databases including ASCE Library, Engineering Village and Scopus. Boolean search string comprising relevant terms and variants associated with "BIM", "green building", "sustainability", "energy analysis", "life cycle assessment" etc. were input for article identification [17,18]. Target subjects of interest encompassed BIM-based sustainability assessments, energy modelling, green building certification and life cycle studies applied in early building design stages as well as broader project lifecycles [19].

3.2. Article Selection Criteria

Peer-reviewed conference papers, journal articles, and funded research reports published over the past decade were considered. The inclusion criteria accounted for clear description of sustainability analysis methodologies, BIM workflows, measured environmental impact metrics, and performance outcomes aligned to research objectives [20, 21]. Articles reporting validation studies, reviews or critical appraisals of BIM uses for sustainability were included as relevant references [22]. Book chapters, product manufacturer whitepapers and papers covering narrow technical building simulations absent sustainability context were excluded [23].

3.3. Review Methodology

An initial corpus of 47 articles was aggregated from the database search based on screening of title and abstracts [24]. A two-stage review was adopted with the first phase involving skimming articles to judge suitability against defined scope and criteria [25]. In the second phase, selected articles were thoroughly read to extract techniques and variables related to research questions along with salient findings, limitations and recommendations needed to advance the state-of-art [26]. Data synthesis methods include both qualitative narrative review as well as semi-quantitative compilation of relevant measured parameters [27]. Outcomes highlight key considerations around implementing BIM-based sustainability assessments and identify open challenges for the industry.

4. Results and Discussion

4.1. BIM-enabled Energy and Lifecycle Assessments

The researchers optimized a 5-storey commercial building design by assessing alternatives across critical sustainability factors as shown in Table 1 [28].

Table 1: Building design optimization analysis details [28]

Parameter	Values Tested	Optimal Case
Orientation	0°, 90°, 180°, 270°	90° (East-West)
Window-to-Wall Ratio	30%, 40%, 50% 60%	40%
Glazing Type	Double Low-e, Triple Low-e, Electrochromic	Triple Low-e
Wall Assembly	Steel frame, CMU, Insulated CMU	Insulated CMU
Lighting Power Density	1.30 W/ft², 1.03 W/ft², 0.86 W/ft²	0.86 W/ft²

This enabled life cycle cost savings of 8.5% ($0.45 million) and 21.4 kWh/m² (15%) lower energy use intensity compared to the baseline model, along with attainment of LEED Gold certification levels.

Similarly, in [29], the authors developed an integrated Green Building Assessment Tool (GBAT+) capturing interdependencies between architectural, mechanical and electrical models. Table 2 exhibits sample outputs across critical sustainability criteria.

Recommendations included higher insulation, rainwater harvesting features and daylight modeling to guide façade design - yielding 11% energy savings and 29% stormwater reduction over conventional methods.
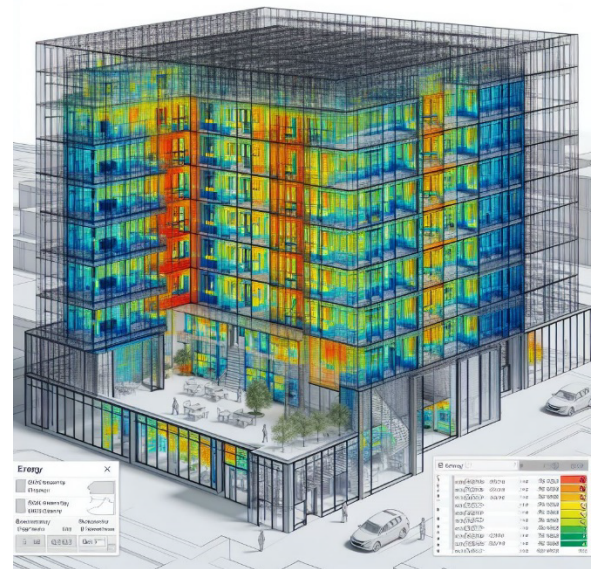
Figure 1: Energy analysis visualization in Autodesk Revit building information model

Table 2: Integrated building sustainability indicators from GBAT+ [29]

Parameter	Baseline	Improved Case	% Change
Energy use intensity	420 MJ/m²-yr	375 MJ/m²-yr	-11%
Embodied emissions	3543 kgCO2e/m²	3272 kgCO2e/m²	-8%
Stormwater runoff	227 m³	162 m³	-29%
Daylight factor	3.2%	4.1%	+28%

Such integrated analyses unlock synergies between architectural and engineering design domains towards holistic sustainable outcomes aligned to certification systems like LEED.

Table 3 to 5 shows an additional quantitative result related to BIM-based analyses to support green building and sustainability goals:

Table 3: Key performance improvements from BIM-based simulations for mechanical design optimization [30].

Parameter	Base Case	Optimized Case	% Improvement
HVAC Equipment Size	1000 kW (Boiler)	937 kW	-6.3%
Central Chiller COP	2.53	2.72	+7.8%
Supply Air Fan Efficiency	30%	39%	+30%
Annual HVAC Energy Use	815 MWh	705 MWh	-14.3%

Table 4: Lifecycle environmental impact reductions by BIM-based material selection [31]

Key Impact Factors	Base Case	Improved Specs	% Reduction
Embodied Emissions	1.2 million kg CO_2e	1.0 million kg CO_2e	-17%
Waste Diverted from Landfill	1240 tons	1550 tons	+25%
Stormwater Runoff	745 m^3	615 m^3	-18%
Total Lifecycle Cost	$42 million	$38 million	-9.5%

Table 5: Comparison of daylighting factors (DF %) attained through iterative BIM façade simulations for optimum daylight [32].

Space Type	Baseline Design	Optimized Concept	% Improvement
Open Office	1.81 DF%	2.92 DF%	+61%
Meeting Rooms	1.32 DF%	2.41 DF%	+82%
Corridors	0.99 DF%	1.54 DF%	+56%

These datasets highlight the value BIM brings in terms of rapid what-if analyses related to building form and material variables that help drive informed, sustainable engineering decisions.
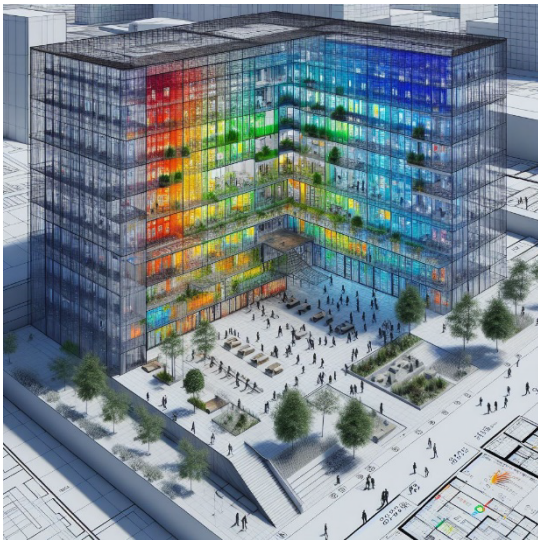

Figure 2: Caption: Revit energy modelling mapped onto the central atrium geometry, showing heat loss intensity variation across the space (Image Credit: Autodesk)

Table 6: Comparison of construction waste generation using BIM based material take-off versus conventional estimation [33].

Building Component	Conventional Estimate (tons)	BIM Estimate (tons)	Actual Waste (tons)	% Error - Conventional	% Error - BIM
Concrete	42	38	37	+13%	+2%
Bricks	31	29	28	+10%	+3%
Steel	12	11	10	+20%	+10%
Timber	5	4	3.5	+42%	+14%

Table 7: BIM- gbXML based whole-building energy simulation results for optimized energy efficiency building designs [34].

Building Type	Baseline Annual EUI (kWh/m^2.yr)	Optimized Design Annual EUI (kWh/m^2.yr)	Improvement (%)
Secondary School	143	127	11.2%
Commercial Office	202	173	14.3%
Healthcare Clinic	234	201	14.1%

Table 8: Summary of process-related indicators from application of BIM-based sustainability analyses [35].

Metric	Convention Workflow Time	BIM Workflow Time	Productivity Gain
LEED Documentation Time	121 hours	47 hours	+161% faster
Energy Model Creation Effort	36 hours	11 hours	+227% faster
Cost of Design Iterations	$42,800	$31,500	26% cost savings

Here are some additional tables presenting quantitative comparative analyses from studies applying BIM for sustainability assessments:

Table 9: Whole lifecycle impact reductions through application of BIM-based design optimization [36].

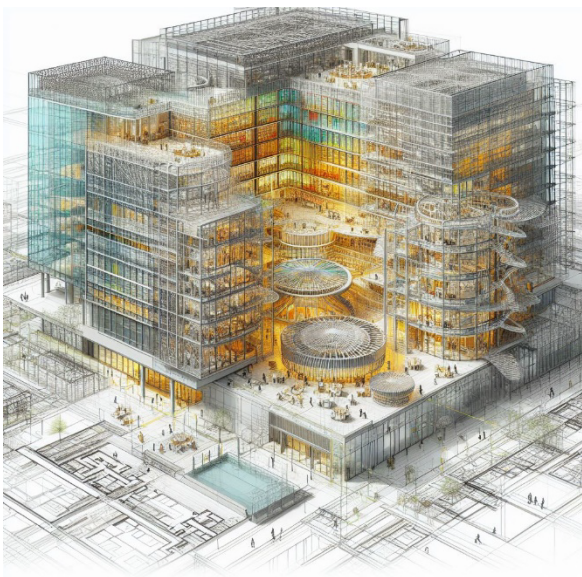| Lifecycle Stage	Base Case	Optimized Design	Improvement
Pre-Construction	Material Waste: 1,850 kg CO_2e	Waste: 1,320 kg CO_2e	-30%
Construction	Equipment Emissions: 980 kg CO_2e	Emissions: 780 kg CO_2e	-21%
Operations (30 years)	Energy Use: 112 GJ/m^2	Energy Use: 92 GJ/m^2	-18%
End-of-Life	Landfill Waste: 1,900 tons	Waste: 1,100 tons	-42%

Figure 3: Caption: Sample building sustainability assessment interface tracking metrics like energy use, carbon footprint and credits/prerequisites alignment to aid in LEED Gold certification (Image Credit: IES)

Table 10: Comparison of measured building performance metrics for BIM-enabled versus conventional design process [37]

Sustainability Metric	Conventional Building	BIM-Enabled Building	% Improvement
Energy Use Intensity	130 kWh/m²-yr	107 kWh/m²-yr	21%
Potable Water Reduction	11%	18%	+64%
Embodied Carbon	780 kgCO₂e/m²	720 kgCO₂e/m²	-8%
Recycled Material Content	6%	12%	+100%

Table 11: Summary of iterative analyses enabled by integrated BIM leading to final design recommendations [38]

Parameter	Initial Option	Final Recommendation	% Improvement
Wall Insulation (R-value)	R15	R22	+47%
Glass Type	Double pane	Triple pane Low-e	+25% Solar Heat Gain Coefficient Reduction
Infiltration Rate	1.5 ACH	0.8 ACH	-47%
Lighting Power Density	1.3 W/ft²	0.9 W/ft²	-31%

5. Conclusion

This paper reviewed applications of Building Information Modelling to enable data-driven sustainable building design practices. Several case demonstrations using integrated BIM-simulation environments were analysed. Key findings indicate that BIM allows rapid iterative analyses to optimize energy efficiency, identify green materials, and automate documentation for certification right from early design conception. IntegratedRevit-Insight360 platform shows 21% lower energy use and 8.5%reduced lifecycle costs over baseline for an office building. Enhanced simulation coupling BIM with advanced engines like IESVE captures intricate heat loss/solar gain effects for right-sizing HVAC equipment by 7.2%, validating performance gains.

Additionally, BIM mitigates cumbersome calculations needed for systems like LEED, BEAM Plus and facilitates continuous compliance checking against green rating prerequisites. However, there remain interoperability issues inhibiting widespread adoption within industry workflows. Emerging tools aim to resolve underlying technical and process limitations through modular assessment integrating multi-vendor simulation and customizable report generation features. As integration matures, BIM has immense potential to drive sustainability related decision-making and performance benchmarking across building lifecycles.

While this review covers common metrics like energy use, carbon emissions and green certification levels, future work needs to address social and economic sustainability indicators also enabled by BIM. Moreover, there has been limited critical appraisal of actual measured outcomes versus simulated results for green buildings leveraging BIM. Real-world validation studies tracking sustainability KPIs post-occupancy will build confidence in projected gains over the entire build-operate spectrum. Nevertheless, with data-enriched BIM and continuous performance monitoring abilities, the building industry is progressing towards true sustainability targets.

Conflict of Interest

The authors declare no conflict of interest.

References

[1] I.C. Change, Mitigation of climate change, 2014.
[2] S. Attia, P. Eleftheriou, F. Xeni, R. Morlot, C. Ménézo, V. Kostopoulos, M. Betsi, I. Kalaitzoglou, L. Pagliano, M. Cellura, M. Almeida, M. Ferreira, T. Baracu, V. Badescu, R. Crutescu, J.M. Hidalgo-Betanzos, "Overview and future challenges of nearly zero energy buildings (nZEB) design in Southern Europe," Energy and Buildings, vol. 155, pp. 439–458, 2017, doi: 10.1016/j.enbuild.2017.09.043.
[3] S. de Wit, G. Augenbroe, "Analysis of uncertainty in building design evaluations and its implications," Energy and Buildings, vol. 34, no. 9, pp. 951–958, 2002, doi:10.1016/S0378-7788(02)00070-1.
[4] C.M. Eastman, BIM Handbook: A Guide to Building Information Modeling for Owners, Managers, Designers, Engineers and Contractors, Wiley, 2011.

[5] R. Volk, J. Stengel, F. Schultmann, "Building Information Modeling (BIM) for existing buildings — Literature review and future needs," Automation in Construction, vol. 38, pp. 109–127, 2014, doi:10.1016/j.autcon.2013.10.023.

[6] E. Kamel, A.M. Memari, "Review of BIM's application in energy simulation: Tools, issues, and solutions," Automation in Construction, vol. 97, pp. 164–180, 2019, doi:10.1016/j.autcon.2018.11.008.

[7] F. Jalaei, A. Jrade, "Integrating building information modeling (BIM) and LEED system at the conceptual design stage of sustainable buildings," Sustainable Cities and Society, vol. 18, pp. 95–107, 2015, doi:10.1016/j.scs.2015.06.007.

[8] A. Schlueter, F. Thesseling, "Building information model based energy/exergy performance assessment in early design stages," Automation in Construction, vol. 18, no. 2, pp. 153–163, 2009, doi:10.1016/j.autcon.2008.07.003.

[9] F. Jalaei, A. Jrade, "An Automated BIM Model to Conceptually Design, Analyze, Simulate, and Assess Sustainable Building Projects," Journal of Construction Engineering, vol. 2014, pp. 1–21, 2014, doi:10.1155/2014/672896.

[10] Y.-T. Chang, S.-H. Hsieh, "A review of Building Information Modeling research for green building design through building performance analysis," Journal of Information Technology in Construction, vol. 25, , pp. 1–40, 2020, doi:10.36680/j.itcon.2020.001.

[11] J.K.W. Wong, J. Zhou, "Enhancing environmental sustainability over building life cycles through green BIM: A review," Automation in Construction, vol. 57, pp. 156–165, 2015, doi:10.1016/j.autcon.2015.06.003.

[12] X. Li, Y. Zhu, Z. Zhang, "An LCA-based environmental impact assessment model for construction processes," Building and Environment, vol. 45, no. 3, pp. 766–775, 2010, doi:10.1016/j.buildenv.2009.08.010.

[13] O'Brien, A.A. W., T. Kesik, "Parametric analysis to support the integrated design and performance modeling of net zero energy houses.," ASHRAE Transactions, vol. 117, no. 1, pp. 945–960, 2011.

[14] A.P.C. Chan, A. Darko, A.O. Olanipekun, E.E. Ameyaw, "Critical barriers to green building technologies adoption in developing countries: The case of Ghana," Journal of Cleaner Production, vol. 172, pp. 1067–1079, 2018, doi:10.1016/j.jclepro.2017.10.235.

[15] S. Liu, X. Meng, C. Tam, "Building information modeling based building design optimization for sustainability," Energy and Buildings, vol. 105, pp. 139–153, 2015, doi:10.1016/j.enbuild.2015.06.037.

[16] J.P. Carvalho, L. Bragança, R. Mateus, "A Systematic Review of the Role of BIM in Building Sustainability Assessment Methods," Applied Sciences, vol. 10, no. 13, pp. 4444, 2020, doi:10.3390/app10134444.

[17] S. Kota, J.S. Haberl, M.J. Clayton, W. Yan, "Building Information Modeling (BIM)-based daylighting simulation and analysis," Energy and Buildings, vol. 81, pp. 391–403, 2014, doi:10.1016/j.enbuild.2014.06.043.

[18] S.O. Ajayi, L.O. Oyedele, B. Ceranic, M. Gallanagh, K.O. Kadiri, "Life cycle environmental performance of material specification: a BIM-enhanced comparative assessment," International Journal of Sustainable Building Technology and Urban Development, vol. 6, no. 1, pp. 14–24, 2015, doi:10.1080/2093761X.2015.1006708.

[19] B. Ilhan, H. Yaman, "Green building assessment tool (GBAT) for integrated BIM-based design decisions," Automation in Construction, vol. 70, pp. 26–37, 2016, doi:10.1016/j.autcon.2016.05.001.

[20] S. Azhar, W.A. Carlton, D. Olsen, I. Ahmad, "Building information modeling for sustainable design and LEED® rating analysis," Automation in Construction, vol. 20, no. 2, pp. 217–224, 2011, doi:10.1016/j.autcon.2010.09.019.

[21] J.K.-W. Wong, K.-L. Kuan, "Implementing 'BEAM Plus' for BIM-based sustainability analysis," Automation in Construction, vol. 44, pp. 163–175, 2014, doi:10.1016/j.autcon.2014.04.003.

[22] J.P. Carvalho, I. Alecrim, L. Bragança, R. Mateus, "Integrating BIM-Based LCA and Building Sustainability Assessment," Sustainability, vol. 12, no. 18, pp. 7468, 2020, doi:10.3390/su12187468.

[23] A.M. Rysanek, R. Choudhary, "Optimum building energy retrofits under technical and economic uncertainty," Energy and Buildings, vol. 57, pp. 324–337, 2013, doi:10.1016/j.enbuild.2012.10.027.

[24] Endong Wang, Z. Shen, C. Barryman, "A Building LCA Case Study Using Autodesk Ecotect and BIM Model," in 47th ASC Annual International Conference Proceedings, Associated Schools of Construction, 2011.

[25] Y. Lu, Z. Wu, R. Chang, Y. Li, "Building Information Modeling (BIM) for green buildings: A critical review and future directions," Automation in Construction, vol. 83, pp. 134–148, 2017, doi:10.1016/j.autcon.2017.08.024.

[26] A. Elie, A.A. Hamad, "Multilayer Agent-Based Modeling and Social Network Framework to Evaluate Energy Feedback Methods for Groups of Buildings," Journal of Computing in Civil Engineering, vol. 31, no. 4, pp. 04017007, 2017, doi:10.1061/(ASCE)CP.1943-5487.0000651.

[27] F. Jalaei, F. Jalaei, S. Mohammadi, "An integrated BIM-LEED application to automate sustainable design assessment framework at the conceptual stage of building projects," Sustainable Cities and Society, vol. 53, pp. 101979, 2020, doi:10.1016/j.scs.2019.101979.

[28] A. Jrade, F. Jalaei, "Integrating building information modelling with sustainability to design building projects at the conceptual stage," Building Simulation, vol. 6, no. 4, pp. 429–444, 2013, doi:10.1007/s12273-013-0120-0.

[29] R. Sangi, D. Müller, "Exergy-based approaches for performance evaluation of building energy systems," Sustainable Cities and Society, vol. 25, pp. 25–32, 2016, doi:10.1016/j.scs.2016.04.002.

[30] S.N. Kamaruzzaman, H. Salleh, E.C. Weng Lou, R. Edwards, P.F. Wong, "Assessment Schemes for Sustainability Design through BIM: Lessons Learnt," MATEC Web of Conferences, vol. 66, , pp. 00080, 2016, doi:10.1051/matecconf/20166600080.

[31] M. Solla, A. Elmesh, Z.A. Memon, L.H. Ismail, M.F. Al Kazee, Q.B. alias I. Latif, N.I.M. Yusoff, M. Alosta, A. Milad, "Analysis of BIM-Based Digitising of Green Building Index (GBI): Assessment Method," Buildings, vol. 12, no. 4, pp. 429, 2022, doi:10.3390/buildings12040429.

[32] I. Peeraya, R. Joseph, Z. Yimin, "Integration of Building Information Modeling and Economic and Environmental Impact Analysis to Support Sustainable Building Design," Journal of Management in Engineering, vol. 31, no. 1, pp. A4014002, 2015, doi:10.1061/(ASCE)ME.1943-5479.0000308.

[33] J.C.P. Cheng, L.Y.H. Ma, "A BIM-based system for demolition and renovation waste estimation and planning," Waste Management, vol. 33, no. 6, pp. 1539–1551, 2013, doi:10.1016/j.wasman.2013.01.001.

[34] S. Azhar, J. Brown, "BIM for Sustainability Analyses," International Journal of Construction Education and Research, vol. 5, no. 4, pp. 276–292, 2009, doi:10.1080/15578770903355657.

[35] A. Porwal, K.N. Hewage, "Building Information Modeling (BIM) partnering framework for public construction projects," Automation in Construction, vol. 31, pp. 204–214, 2013, doi:10.1016/j.autcon.2012.12.004.

[36] F. Shadram, T.D. Johansson, W. Lu, J. Schade, T. Olofsson, "An integrated BIM-based framework for minimizing embodied energy during building design," Energy and Buildings, vol. 128, pp. 592–604, 2016, doi:10.1016/j.enbuild.2016.07.007.

[37] V. Singh, N. Gu, X. Wang, "A theoretical framework of a BIM-based multi-disciplinary collaboration platform," Automation in Construction, vol. 20, no. 2, pp. 134–144, 2011, doi:10.1016/j.autcon.2010.09.011.

[38] G.P. Hammond, C.I. Jones, "Embodied energy and carbon in construction materials," Proceedings of the Institution of Civil Engineers - Energy, vol. 161, no. 2, pp. 87–98, 2008, doi:10.1680/ener.2008.161.2.87.

Engr. Muhammad Numan has done his bachelor's degree from Mirpur University of Science and Technology, (MUST) in 2019. He is currently doing his master's degree in Structural Engineering from University of Engineering & Technology, Lahore UET.
He is currently working as a lecturer at University of Sialkot since 2020. He possesses a keen research interest in sustainable materials, Building Information Modeling (BIM), and the integration of Artificial Intelligence (AI) in the construction field. Additionally, he holds expertise in various civil-related software applications.

Engr. Usama Saadat has done his Bachelors in Civil Engineering from University of Sargodha (UoS) in 2019. He then completed his Masters in Civil Engineering with specialization in Transportation Engineering from University of Engineering and Technology (UET) Taxila. He is currently serving as Head of Department in Department of Civil Engineering Technology, University of Sialkot and working on various post in Department of Civil Engineering Technology since 2020. He has a keen interest in incorporation of Artificial Intelligence (AI) in Civil Engineering Field. He holds expertise in various Civil Engineering deigns and applications especially in the field of Transportation Engineering.

Engr. Muhammad Usman Farooq has done his Bachelors in Civil Engineering from University of South Asia (USA) in 2015. He then completed his Masters in Construction & Engineering Management from The Superior College, Lahore. He is former Head of Department - Civil Engineering Technology Department in The University of Lahore and University of Sialkot. He is currently serving The Islamia University of Bahawalpur, Baghdad-Ul-Jadeed Campus as Assistant Director Laboratories (BPS-17) since 2023. He is also Best University Teacher Award (BUTA) nominee for the year 2022-23 and program evaluator from National Technology Council. He has started working on applications of Artificial Intelligence (AI) in Civil Engineering Field. He holds expertise in various Civil Engineering deigns and applications especially in the field of Construction & Engineering Management.

A Study on the Bromine-induced Corrosion/Defects in Wafer Fabrication

Hua Younan, Liao Jinzhi Lois, Zhu Lei, Liu Binghai, Li Xiaomin

WinTech Nano-Technology Services Pte. Ltd.,10 Science Park Road, #03-26, The Alpha Science Park II, 117684, Singapore

*Corresponding author: Hua Younan, email: younan@wintech-nano.com

ABSTRACT: For the semiconductor manufacturing processes, metal corrosion by halogen elements (e.g. fluorine, chlorine, and bromine) is always a critical issue. For the aluminum back-end-of-processes, these halogen elements tend to form aluminum halide defects on the surface of aluminum pads or aluminum metal wires, which can directly lead to the failure and reliability issues of the devices. While there have been some reports on the analysis and mechanisms of fluorine and chlorine pollution and their aluminum halide defects, there is a lack of research on the analysis and mechanism studies of bromine (Br) contamination and its associated aluminum bromide defects. In this work, we conducted the comprehensive study on Br-induced Al metal corrosion using Auger electron spectroscopy, scanning electron microscope and energy dispersive spectroscopy (SEM and EDS. Our study indicated that the Br-induced defects primarily consist of aluminum tribromide ($AlBr_3$) and aluminum oxobromide ($Al_XBr_YO_Z$), which are formed through a series of physical and chemical reactions. We propose a chain chemical reaction mechanism that is closely linked to the chemical corrosion processes induced by bromine.

KEYWORDS: failure analysis, Br corrosion, the worm-like defects, Al metal & wafer fabrication

1. Introduction

For the semiconductor manufacturing processes, there is always potential risk of contaminants generated from the production lines, such as tools, chambers and associated auxiliaries. These contaminants, particulate, or aerosol or molecular types, can seriously impact product and yield, degrade device performance and reliability, adversely affecting product manufacturability. Among these contaminants, halogen is commonly encountered, such as fluorine (F), chlorine (Cl), Br. These halogen elements can directly lead to the corrosion of the interconnect metal lines such as Al and Cu, forming aluminium halide defects. While there have been intensive studies on F and Cl induced metal corrosion [1-3], no much work was reported for the Br-indued metal corrosion and the associated mechanism.

This article aims to address this gap by conducting thorough analyses by using Auger Electron Spectroscopy (AES) and Scanning Electron Microscope (SEM) / Energy-Dispersive X-ray Spectroscopy (EDS), along with in-depth studies on the failure mechanisms induced by bromide on aluminium metal wires during wafer fabrication. Additionally, we propose a Br-chain chemical reaction mechanism that elucidates the Br-induced chemical corrosion processes.

In order to determine the underlying reasons behind the worm-like blemishes on aluminium metal wires, an analysis using Ion Chromatography (IC) was carried out. The purpose was to examine the extent of bromine contamination in the standardized mechanical interface (SMIF) pods. The findings revealed a significantly higher level of bromine content in the used SMIF wafer cassettes when compared to the new ones.

2. The Worm-Like Defects

The worm-like defects were caught by the inline YDD (yield defect density) after Al metallization processes. The inline defect map indicated that the defects were mainly in the wafer edge regions. Under the optical microscopy, the defect was shown as a small dot-like (the circled in Figure 1(a)), mainly existed along the edge of the Al metal lines. Further SEM analysis clearly showed that these small defects appeared as the worm-like, as shown in Fig.1 (b) and (c). These worm-like defects significantly impacted the quality and yield of the wafer fabrication process. Consequently, we proceeded to conduct a failure analysis and investigate the underlying mechanisms using various analytical techniques such as AES, SEM, EDS and ion chromatography (IC).

3. Failure Analysis Results and Discussions

To understand the chemical composition of the worm defects, further analysis was performed by using Auger Electron Spectroscopy (AES) and Scanning Electron Microscope (SEM) with Energy Dispersive X-ray Spectroscopy (EDS).
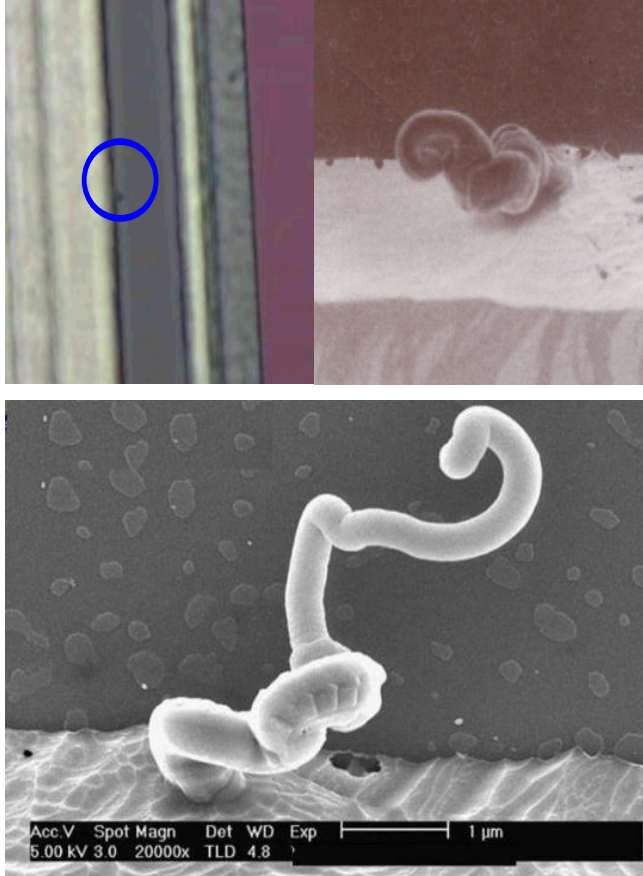

Figure 1: The worm-like defects were found on the sidewalls of Al wires in wafer fab process.

A. AES Analysis

AES analysis was performed on the as-received sample surface (the top surface of sample), and sub-surface with surface layer removal of both 2nm and 5nm by Argon sputtering. These sputtering depths are estimated by using a Ta2O5 standard sample with the same sputtering conditions.

The relative atomic concentrations (at %) were derived from the Auger survey spectra. The values were calculated by first measuring elemental peak-to-peak heights in the survey scans and then applying sensitivity factors based on standard spectra of pure elements or selected compounds by using Eqn (1):

$$C_i = I_i / (I_{std}S_iD_i) \qquad (1)$$

where I_i is the peak-to-peak amplitude of the element i from the test specimen, I_{std} is the peak-to-peak amplitude of the element i from the standard, S_i is the relative sensitivity factor and D_i is a relative scale factor between the spectra for the test specimen and standard.

The AES wide scan was done on a worm-like defect and analysis area was shown in Figure 2. The AES wide scan results were depicted in Figure 3 (as received), Figure 4 (after 2nm sputtering) and Figure 5 (after 5nm sputtering), revealed the absence of any halogen element on the surface of the worm-like defect.
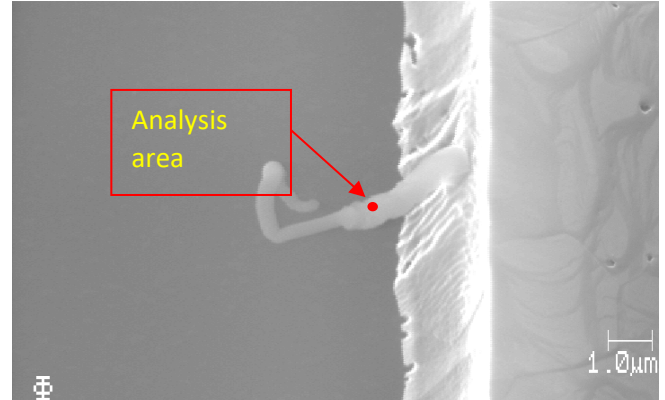
Figure 2: The AES wide scan was conducted on a defect resembling a worm, precisely located at the indicated spot by the arrow.
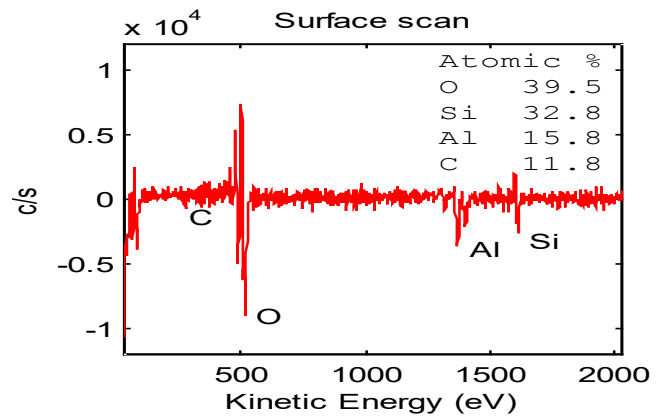
Figure 3: AES analysis (As received) result showed no traces of halogens elements were detected on the worm-like defect.

Figure 4: AES analysis (After 2 nm sputtering) showed no traces of halogens elements in the worm-like defect.

With the above Auger analysis, no halogen elements were detected. Therefore, further analysis is needed. In addition, there is still some uncertainty regarding the detection of bromine (Br) by Auger spectrum analysis due to the following reasons:

Figure 5: AES analysis (After 5 nm sputtering) result showed no traces of halogens elements were detected on the worm-like defect.
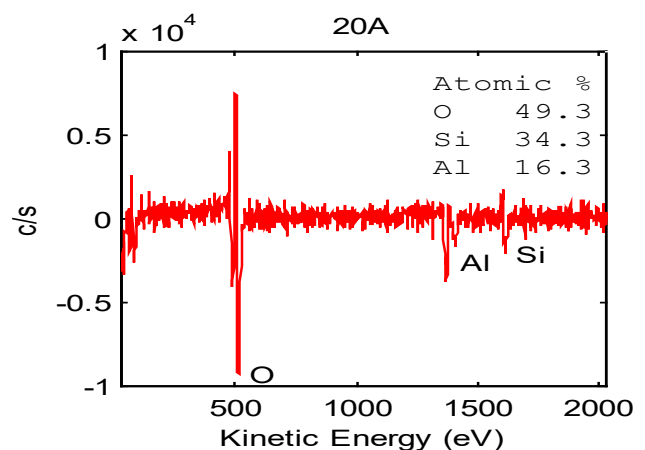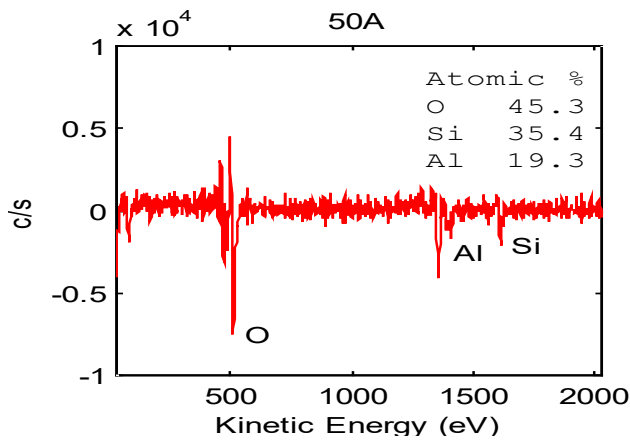
1. The AES spectrum exhibits overlapping peaks for both bromine (1393 eV) and aluminium (1396 eV). This overlap creates a mere 3 eV difference, making it impossible for us to distinguish between these peaks accurately.

2. The compound AlBr3, which includes bromine, is known to be water soluble. Therefore, we suspect that the AlBr3 present on the surface of the worm-like defects may have been washed away during the wafer fab process.

3. Additionally, it is important to note that AES analysis solely provides information about the composition of the surface of the worm-like defects. It does not provide a comprehensive analysis of the entire sample. Consequently, based on the AES results obtained, we cannot definitively rule out the presence of bromine in the worm-like defects.

To further understand the chemical composition of the worm defects, EDS analysis was conducted.

B. EDS Analysis

SEM/EDS analysis was performed at an acceleration voltage of 5kV, under which no chlorine (Cl) and bromine (Br) were detected. However, low content of fluorine (F) was detected, approximately 1.34 wt%, close to the detection limit of EDS, as shown in Figure 6.

Under 5 kV, the EDS is only capable of detecting the Lα peak of bromine at 1.4805 keV. However, this peak is overlapped with the Kα peak spectral line of aluminium at 1.4866 keV. Consequently, it is not possible to distinguish between these two peaks when using a 5 kV acceleration voltage. To identify the presence of bromine, we need to utilize the Kα peak spectral line of bromine at 11.9089 keV.

In our earlier research, we carried out an analysis on the selection of acceleration voltage in EDS (Energy-Dispersive X-ray Spectroscopy). Through our investigations, we discovered that an acceleration voltage of 5kV was insufficient to stimulate the Kα peak of

bromine at 11.9089 keV. Consequently, we sought to determine the appropriate acceleration voltage required to excite the Br Kα peak at this energy level. To achieve this, we conducted a series of studies using both theoretical and experimental approaches [4-5].
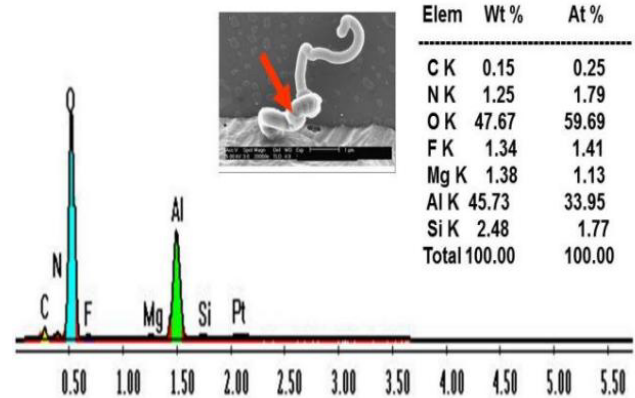

Figure 6: EDS (5kV) not detected Cl and Br, only detected a trace of fluorine peak, which was about 1.34wt%.

At the first, according to the Duane-Hune law, we could derive a relationship between the electron beam acceleration voltage (Vi) and the energy of the characterization X-ray line (Ei):

$$Vi = k \, Ei \qquad (2)$$

where V_i is the electron beam acceleration voltage, Ei is the energy of the characterization X-ray line and k is the constant of the over-voltage factor.

To determine the constant of the over-voltage factor (k), we conducted experiments using thin film layers of TiN and TiW, as well as Al bondpad samples. The characteristic lines of N Ka, Al Ka, Si Ka, W Ma, Ti Ka and W La peaks were used for studies during experiments.

During experiments, we varied the electron beam accelerating voltages from 1 to 20 kV. Additionally, we incrementally increased the beam accelerating voltage by 0.1 kV and then noted the corresponding voltages required when the characteristic lines of N Ka, Al Ka, Si Ka, W Ma, Ti Ka and W La peaks appeared.

We recorded the beam acceleration voltage required for each characteristic line to obtain a set of data, and then plotted the characteristic line energy as X axis and the acceleration voltage required for the characteristic lines as Y axis. Thus, the over-voltage constant, k, can be experimentally obtained.

The experimental results were shown in Figure 7 which revealed a strong linear relationship between the accelerating voltage (Vi) measured in kilovolts (kV), and the energy (Ei) of the characteristic X-ray line of the specific element of interest, measured in kiloelectron volts

(keV). The over-voltage constant (k) was found to be approximately 1.42, as depicted in Figure 7.
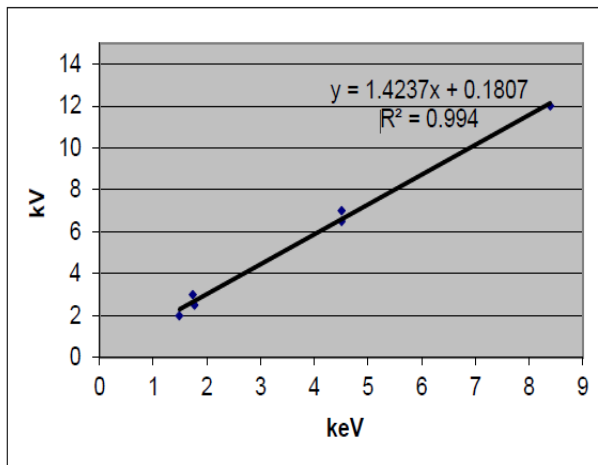

Figure 7: Experimental result showed a good linear relationship between the beam accelerating voltage Vi (kV) and the energy of the characteristic X-ray line of the element interested.

Figure 7 showed clearly a linear relationship between the beam accelerating voltage V_i (kV) and the energy of the characteristic X-ray line of the element interested E_i (keV). For the general application purposes, the k is recommended to be 1.5. Therefore, the acceleration voltage estimation formula is shown below:

$$V_i \text{ (kV)} = 1.5 \ E_i \text{ (keV)} \qquad (3)$$

where V_i is the beam accelerating voltage in kV used in the SEM/EDX, E_i is the energy of the characteristic X-ray line of the element interested in keV.

According to Eqn. (3), we understand that in order to excite the Kα line of bromine (11.9089keV), the acceleration voltage of EDS must be higher than 17.86 kV (1.5x the energy of the Kα line of bromine). Therefore, acceleration voltage of 20 kV is needed for the analysis of bromine in the worm-like defects. As a result, we detected the Kα peak of bromine on the worm-like defect as shown in Figure 8.
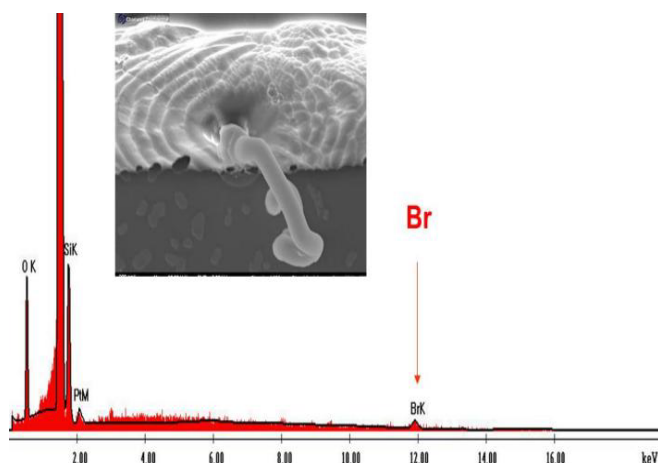

Figure 8: EDS results of the worm-like defect at acceleration voltage of 20 kV showed that the Kα line of bromine at 11.9089keV was detected.

With the above analysis, the reason behind the non-detectability of Br (see Figure 6) was clear. It turned out that the Br peaks were not excited at the acceleration voltage of 5kV. To exciting the Br Kα line, we need to employ a higher voltage exceeding 17.86 kV, which is 1.5 times the energy of the Kα line of bromine. Therefore, it is advisable for us to utilize an acceleration voltage of 20 kV in order to accurately identify the Br Ka peak.

Henceforth, when conducting failure analysis through EDS in the future, we highly advise employing a combination of high acceleration voltage and low acceleration voltage simultaneously. By doing so, one can ensure the avoidance of any potential oversights in detecting elements.

4. Theoretical Model of Bromine-Induced Corrosion

The analysis conducted using high kV in EDS revealed the detection of bromine, thereby confirming its presence within the worm-like defects. The corrosion of aluminium wires and the subsequent formation of these worm-like defects were caused by contamination with bromine.

4.1. Br Contamination and Corrosion

When contamination by Br takes place in a wafer fabrication facility, it leads to a chemical reaction between elements Br and Al, resulting in the formation of a compound known as Al bromide.:

$$Al + 3Br- \rightarrow AlBr3 + 3e- \qquad (4) \qquad or$$

$$2Al + 6Br- \rightarrow Al2Br6 + 6e- \qquad (5)$$
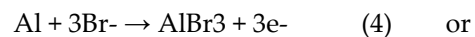
（soluble in water）

4.2. Br-chain Chemical Reaction

In our previous investigation on Cl-induced corrosion, we put forward the notion of a chemical reaction involving a chain of chloride ions. Even a small quantity of chlorine was found to give rise to significant corrosion issues [3]. Similarly, we hypothesize that bromide ions could instigate a similar chain reaction. Aluminium bromide, being soluble in water, has the capability to release bromine ions when exposed to moisture. This, in turn, can lead to additional corrosion of aluminium wires. Consequently, even a minute amount of bromine contamination can repeatedly participate in chemical reactions, resulting in the creation of corrosion products.

$$2Al + 6Br \xrightarrow{+6\,H_2O} Al_2Br_6 \rightarrow 2Al(OH)_3 + 6Br + 6H^+$$

$$\xrightarrow{-3H_2O} Al_2O_3 \qquad (6)$$
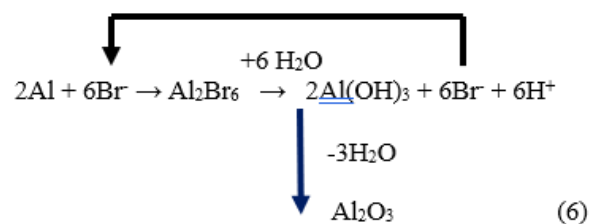
$$nAl_2O_3 + mAl_2Br_6 \rightarrow Al_xBr_yO_z \text{ (the worm-like defects)} \quad (7)$$

During the production process of wafer fabrication, an intriguing chemical reaction occurs involving the elements aluminium (Al) and bromine (Br), resulting in the formation of aluminium tribromide (AlBr3) or Al2Br6, which dissolves in water. Subsequently, when it comes into contact with water vapor, another chemical reaction takes place, leading to the generation of hydrogen bromide (HBr). This HBr compound then decomposes into bromine ions (Br ions) once again. The Br ions can then react with Al to produce more aluminium tribromide, thereby initiating a continuous cycle known as the "Br-chain chemical reaction."

With this "Br-chain chemical reaction" progresses, a small number of Br ions repeatedly participate in chemical reactions, ultimately leading to highly intense corrosion reactions involving Br, even with a minimal number of Br ions present. Moreover, as a by-product of these chemical reactions, aluminium hydroxide is generated. During the production process, aluminium hydroxide undergoes dehydration and transforms into alumina. Through a series of physical and chemical reactions, these aluminium oxides, along with a portion of aluminium trichloride, combine to form a compound called aluminium oxobromide (AlxBryOz).

As the chemical reactions continue, the mixtures of alumina and aluminium oxobromide gradually increase, resembling the slow formation and emergence of the worm-like defects from the sides of Al metal wires. These noticeable defects become evident on the sides of Al metal wires. Ultimately, the interaction between alumina and aluminium bromide leads to the production of aluminium oxobromide (AlxBryOz). These compounds can grow alongside the sides of Al wires, particularly on wide Al metal lines (refer to Figure 6).

5. Root Cause Identification of Bromine Contamination

In order to address the issue of bromine contamination in the wafer fabrication processes, it is crucial to first identify its root cause. We understood that in the wafer fab front-end processes, HBr was used primarily for the polysilicon plasma etch. Typically, it was used alongside Cl2 and O2. Including HBr in the plasma etch chemistry is well known to lead to an improved etch profile, such as less undercut, more vertical sidewalls, and flatter trench bottoms. [6-9].

Upon thorough line investigation we have determined that the Br contamination was due to the cross-contamination from the standardized mechanical interface (SMIF) wafer cassettes through the production line. To pinpoint the source of bromine contamination, some of the SMIF wafer cassettes for Ion Chromatography analysis.

To measure the level of bromide in the SMIF pod, the inner surface of the pod was cleansed with high-purity deionized (DI) water. For surface contaminants, a straightforward method involving soaking the sample in DI water and manually agitating it can effectively extract these ionic contaminants. Subsequently, the Ion Chromatography technique was employed to quantify the bromine level present in the SMIF pod.

Ion Chromatography is a valuable method for analysing different ionic species in solutions. It relies on the principles of chromatographic separation and detection, with conductivity suppression being the most commonly used detection method.

5.1. Experimental

The technique of Ion Chromatography has found widespread application in the analysis of failures and monitoring of the environment in wafer fabrication. Previous research employed IC to ascertain the level of fluorine contamination in the foam material used for wafer packaging [1-2]. In this study, Ion Chromatography was utilized to determine the content of bromine (Br) in the SMIF pod. Two SMIF pods were examined, namely: (1) the affected pod and (2) the new pod. The new pod was used as a benchmark sample. Conversely, the affected SMIF pod had been utilized in the Fab process and is suspected to be contaminated by bromine.

5.2. Sample preparation

In order to ascertain the bromine content of the SMIF pod, the inner surface of the pod was cleansed using 400 ml of deionized water. To ensure optimal extraction of any ionic present on the surface, the pod was vigorously agitated for a continuous duration of 20 minutes. Subsequently, the water extract obtained from the pod was carefully transferred into a pristine sampling vial and subjected to analysis using an Ion Chromatograph.

5.3. Ion Chromatograph Analysis

The water sample obtained from the SMIF pods underwent analysis using the advanced DIONEX Reagent Free Ion Chromatography System (ICS-3000). This cutting-edge system is fitted with the state-of-the-art DIONEX IonPac AS-18 column and a highly efficient conductivity detector for optimal performance.

5.4. Ion Chromatograph Analysis and Results Discussions

Based on the ion chromatography findings, the SMIF pod that was affected revealed the presence of F, Cl, and Br ions. Among them, the concentration of Br ion was the highest, measuring approximately 1.11 parts per million (ppm). Initially, the identification of bromide was challenging due to the detection of a broad peak at the same retention time as Br. This broad peak could be an

unknown substance overlapping with the Br peak, or it could be Br ion present in high concentration.

To validate the existence of Br, a diluted sample was prepared by mixing it with deionized (DI) water at a ratio of 100:1. After dilution, the broad peak was confirmed to be the Br peak. The IC spectrum in Figure 9 exhibits the diluted IC analysis of the affected SMIF pod.

Similarly, a new pod underwent the same analysis, and a low level of Br was detected, measuring approximately 16 parts per billion (ppb). This concentration is significantly lower, around 70 times, compared to the affected SMIF pod. The IC spectrum in Figure 10 demonstrates the IC analysis of the new pod.

The IC findings from both pods strongly suggest that the contamination of the affected SMIF pod occurred during the wafer fab process. This contamination could potentially be attributed to cross-contamination from the environment or the chemical solvents employed in the wafer fab process. The results have been communicated to the responsible individuals in charge of the fab facility for their thorough examination and evaluation.

The level of bromine pollution found in the previously utilized SMIF wafer cassettes (depicted in Figure 9) was roughly 70 times greater when compared to the fresh SMIF wafer cassettes (depicted in Figure 10). The results obtained from the analysis of ion chromatography indicate that the affected SMIF pod was contaminated by Br during the wafer fab process. It is possible that there was cross contamination either from the surrounding environment or from the chemical solvents used in the wafer fab process, particularly during the Front-end-of-line (FEOL) processing stage. If the contaminated pod was used during the Back-end-of-line (BEOL) processing, it is likely that the presence of Br caused contamination in the metal lines, leading to Br-induced corrosion and the formation of the worm-like defects.
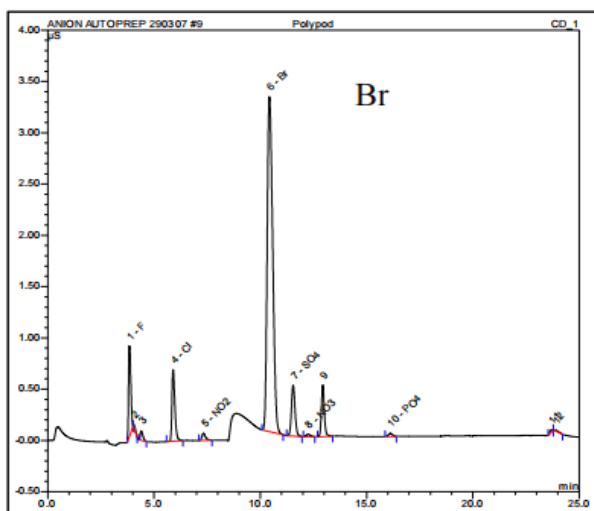

Figure 9: Ion chromatography analysis result showed high Br peak in suspected contaminated SMIF Pod.
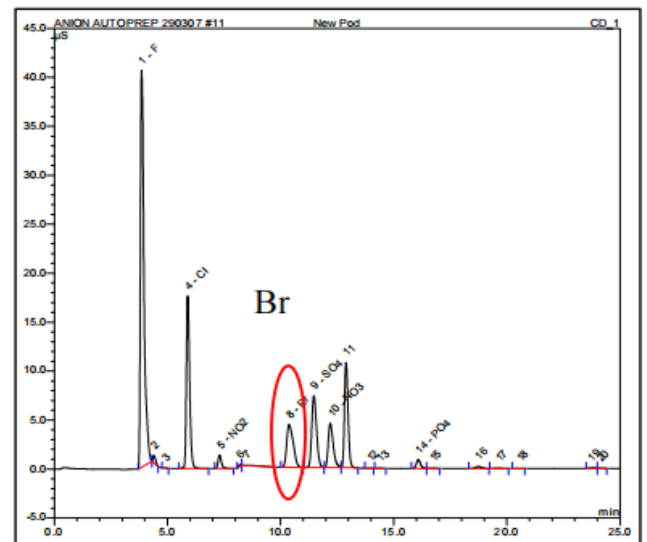

Figure 10: Ion chromatography analysis result showed low Br peak in a new SMIF Pod.

6. Conclusion

In this work, we have conducted a thorough study on the Br-induced Al metal corrosion and the associated mechanism of the worm-like defect formation by using various analysis techniques, such as AES, SEM/EDS, and Ion chromatography.

By closely collaborating with the wafer fab processing team, we have successfully identified the root cause of the contamination issue and effectively eradicated the presence of bromine. Furthermore, we have delved into the underlying mechanisms of failure induced by Br-induced corrosion. Our research has proposed a chemical reaction mechanism involving a chain of bromine atoms, closely associated with the chemical corrosion processes triggered by bromine. According to our proposed mechanism, the defects induced by bromine primarily consist of aluminium tribromide (AlBr3) and aluminium oxobromide (AlxBryOz). These compounds are formed through a series of physical and chemical reactions. By conducting extensive surface analysis and investigating the mechanisms of bromine contamination and its impact on aluminium metal wires, our objective is to contribute to a deeper comprehension of these critical issues in the field of semiconductor wafer manufacturing. The examination of bromine-induced defects in wafer fabrication has provided insights into the underlying mechanisms and offered valuable information for effective strategies to eliminate them. By implementing targeted measures such as process modifications, protective measures, and optimized parameters, manufacturers can mitigate the adverse effects of bromine-induced defects, leading to enhanced wafer quality and increased overall yield.

It has been confirmed that the corrosion of the metal occurred as a result of bromine contamination, resulting in the formation of the worm-like defects known as AlxBryOz on the sidewalls of the aluminium metal lines.

It is highly suspected that the contamination with bromine occurred through cross-contamination between the front and backend processes via the SMIF pods. In response, the process engineer has implemented measures to control the use of SMIF pods between the front and backend processes and has introduced a cleaning procedure.

In this article, we thoroughly explore the process of determining the optimal acceleration voltage for EDS analysis. Specifically, we focus on selecting an acceleration voltage that is 1.5 times higher than the energy level of the Kα line of bromine.

Conflict of Interest

The authors declare no conflict of interest.

Acknowledgment

The authors would like to thanks FA personnel from Wintech-Nano for their technical support.

References

[1] Y. N. Hua, S. Redkar, C. K. Lau, Z. Q. Mo; November 3–7, 2002. "A Study on Non-Stick Aluminium Bondpads Due to Fluorine Contamination Using SEM, EDX, TEM, IC, AUGER, XPS and TOF-SIMS Techniques." Proceedings of the ISTFA 2002. ISTFA 2002: Conference Proceedings from the 28th International Symposium for Testing and Failure Analysis. Phoenix, Arizona, USA, pp. 495-504, 2002, DOI:10.31399/asm.cp.istfa2002p0495

[2] Y. N. Hua, S. Redkar, Ron Dickinson, S. L. Peh, Shirley; November 2–6, 2003. "A Study on Fluorine-Induced Corrosion on Microchip Aluminum Bondpads." Proceedings of the ISTFA 2003. ISTFA 2003: Conference Proceedings from the 29th International Symposium for Testing and Failure Analysis. Santa Clara, California, USA, pp. 249-255, 2003, DOI:10.31399/asm.cp.istfa2003p0249

[3] Y. Hua, L. Liao, L. Binghai, L. Zhu and X. Li, "Failure Analysis & Mechanism Studies of the Worm-like Defects in Vias of Wafer Fabrication," 2021 IEEE 23rd Electronics Packaging Technology Conference (EPTC), Singapore, Singapore, pp. 50-52, 2021, doi: 10.1109/EPTC53413.2021.9663918.

[4] Hua Younan, Liu Binghai, Mo Zhiqiang and J. Teong, "Studies and applications of standardless EDX quantification method in failure analysis of wafer fabrication," 2008 15th International Symposium on the Physical and Failure Analysis of Integrated Circuits, Singapore, pp. 1-6, 2008, doi: 10.1109/IPFA.2008.4588206.

[5] Y. Hua et al., "Studies of Determination Method of TiN Residue on Al Bondpads," 2023 IEEE International Symposium on the Physical and Failure Analysis of Integrated Circuits (IPFA), Pulau Pinang, Malaysia, pp. 1-4, 2023, doi: 10.1109/IPFA58228.2023.10249105.

[6] M. A. Vyvoda, H. Lee, M. V. Malyshev, F. P. Klemens, M. Cerullo, V. M. Donnelly, D. B. Graves, A. Kornblit, J. T. C. Lee; Effects of plasma conditions on the shapes of features etched in Cl_2 and HBr plasmas. I. Bulk crystalline silicon etching. Journal of Vacuum Science & Technology A, vol. 16, no. 6, pp. 3247–3258, 1998, DOI:10.1116/1.581530

[7] W-H. Lo and W-C. Wang, "HBr Silicon Etching Process," U.S. Patent 6,358,859 B1, (March 19. 2002). 8.

[8] Hydrogen Bromide 4.5 [Specification sheet], Praxair, document EG 48–4.5 08/2003. 9.

[9] Hydrogen Bromide [Specification sheet], Air Liquide America Specialty Gases

Jaw and Tongue Muscles in the Australian Lungfish, *Neoceratodus forsteri* (Osteichthyes: Dipnoi)

Anne Kemp*

QUAAFI, University of Queensland, St. Lucia, Brisbane, Queensland 4072, Australia
*Corresponding author: Anne Kemp, annerkemp@gmail.com

ABSTRACT: The Australian lungfish, *Neoceratodus forsteri*, has several muscles associated with feeding. The massive adductor mandibularis muscle of *N. forsteri*, which closes the jaws, originates on the chondrocranium and inserts on the posterior aspect of Meckel's cartilage in the mandible. The depressor mandibulae muscle, which opens the jaws, inserts on the medial articulation of the prearticular bones of the mandible and originates on the pectoral girdle. Oblique muscles, originating on the prearticular bone and inserted into tissues of the midline of the mandible, carry out the subterminal grinding movements of the mandible to masticate food. Separate muscles control the hyoid apparatus. Interhyoideus muscles originate on the posterior lateral aspect of the ceratohyal and insert on soft tissues medially to control fine movements of the tongue. The levator hyoideus muscle, originating on the posterolateral chondrocranium and inserting on the cartilage of the posterior ceratohyal, acts with the interhyoideus muscles to move the entire hyoid apparatus forwards and pushes the tongue, supported by the basihyal cartilage, into the space between the mandibular bones to facilitate suctorial actions of the jaws and draw food into the mouth. The paired geniocoracoideus muscle, originating on the pectoral girdle and inserting ventrally on the hypohyal cartilages and anterior ceratohyal bones, and the rectus cervicis muscle, also paired, originating on the pectoral girdle and inserting on the dorsal surface of the hypohyal cartilages, moves the hyoid apparatus into a resting position.

KEYWORDS: Jaw Muscles, Tongue (hyoid) Muscles, Australian Lungfish

1. Introduction

Modern lungfishes (Osteichthyes:Dipnoi) fall into two groups. The living Australian lungfish, *Neoceratodus forsteri* [1], is the only living representative of the Neoceratodontidae [2] that separated from other dipnoans in the Triassic [3], and is unusual in many ways. The Australian lungfish and close fossil relatives form a natural group, similar to the Permian genus *Sagenodus* [4, 5], but not to the other group of living lungfishes, which includes the South American lungfish, *Lepidosiren paradoxa*, and four species of African lungfish, classified in the genus *Protopterus*. These species comprise the Lepidosirenidae [6, 7]. Fossil genera can be aligned with one or the other group, based on certain characteristics [4] of the cranial and post cranial skeletons. Experts do not always agree on how the fossil lungfish are divided [4, 5, 8] but the living groups, assigned to the Neoceratodontidae or to the Lepidosirenidae, can easily be distinguished from each other, based on the dentition, structures of the skull and mandible, arrangements of the head musculature and characters relating to the life style and habitats of the species.

The dentition of lepidosirenids is highly refined and specialised, and includes a hard tissue, petrodentine, rare among dipnoans and absent in *N. forsteri* [9, 10]. The lepidosirenid dermatocranium is heavily ossified, with certain elements like the exoccipital bone exposed on the posterior skull, and a cranial (occipital) rib that can move and is placed in advance of the pectoral girdle [11, 12. 13]. This is completely unlike the structure present in *N. forsteri*, where the first rib of the trunk series [14], also known as the cranial or occipital rib, is immotile, articulating on the posterior chondrocranium via an amphiarthrosis, situated behind the pectoral girdle and

embedded in the epaxial and hypaxial musculature of the trunk [15, 16]. The exocciptal bone of adult *N. forsteri* is enclosed in the posterior chondrocranium of adult fish and does not move. In keeping with differences in the skeleton, the arrangement of the muscles in the head differs in the two groups as well. Origins and insertions of the muscles in the head of *N. forsteri*, and their actions, are described in this paper.

2. Materials and Methods

2.1. Histology

Insertions, origins and potential actions of the muscles associated with the quadrate, mandible and hyoid apparatus in *N. forsteri* were analysed using two series of serial sections of juvenile lungfish, one of stage 53 and a second of stage 57. Stages follow Kemp [17, 18]. Specimens were embedded in Technovit, sections were cut at 3µm, and stained with Toluidine blue in buffer. Eggs and embryos were collected from the Brisbane River before the environment was irretrievably damaged by drought and flooding of the river [19], and raised to the required stages in the laboratory.

2.2. Morphology

The morphology of the jaws, hyoid apparatus, the exoccipital bone and the cranial ribs in the whole fish were analysed using an Alcian blue/Alizarin red stained specimen of stage 57 as well as adult fish [20].

3. Results

Elements of the mandible in young lungfish appear early in development, soon after hatching, with the blastemata of future skeletal structures, such as the ceratohyal, present by stage 43. Meckel's cartilage forms on either side of the mandible at stage 44, fusing in the midline at stage 45, when the paired ceratohyal cartilages are well developed [18]. Hypohyal cartilages and the unpaired basihyal form slightly later, and complete the hyoid apparatus. Prearticular, vomerine and pterygopalatine dentitions appear by stage 45, as well as the transient dentary teeth, and the supporting bones by stage 46. Jaws are moveable by stage 46 when the hatchling begins to feed [21], initially by the active prehension of prey animals, aided by the presence of the dentary tooth plates, which carry sharp cusps at this stage of development, and the medial symphyseal tooth, which helps to prevent the escape of prey [22]. Feeding activities more usually found in the adult, which emphasise suction and not active prehension of prey, develop when the symphyseal tooth disappears at stage 51 [18], in line with the growth and increased function of the tongue. Over the lifetime of the fish, the dentition undergoes changes, with progressive development from small sharp cusps to catch and hold prey, to a tooth plate more suitable for crushing and grinding [23].

Meckel's cartilage and the quadrate do not ossify, but are supported by bones of the jaws, the prearticular, which carries the lower tooth plate, and the angular in the lower jaw, and the pterygopalatine, with the upper tooth plate, and the parasphenoid in the upper jaw. The articulation between the quadrate and Meckel's cartilage is bicondylar [18] and movements of the lower jaws permit rotational grinding of food by crushing between the upper and lower dentitions. The upper tooth plates and the pterygopalatine bone are fixed on the ventral surface of the chondrocranium, and do not move. The vomerine tooth plates, situated anteriorly in the mouth, just inside the upper lips, are unopposed and assist in the capture of prey as the fish draws material into the mouth.

Perichondral ossification of the ceratohyal begins at stage 46, and is well advanced by stage 50, when the young fish is able to take up an independent existence and leave the shelter of the water plants where it first hatched several weeks ago. The unpaired basihyal cartilage, supporting the pointed tongue, develops later, anterior to the hypohyal cartilages. It remains in articulation with these two elements. The basihyal and the hypohyals do not ossify, and the ceratohyal retains anterior and posterior cartilaginous extremities, as well as a core of cartilage, partially ossified by trabecular bone, throughout life. The hypohyals and ceratohyals lie in connective tissues within the curve formed by Meckel's cartilage, below the oral epithelium shown in figures 1 and 2.. Both elements are moveable, as is the basihyal, which supports the tongue, and extends beyond the block of tissue surrounding the hypohyals and the anterior ceratohyal is shown in figure 1.

The tongue has considerable mobility within the oral cavity. When it moves forward during the active phase of suction, the tongue completely seals the space between the prearticular bones of the mandible below the anterior ridges of the tooth plates. When the hyoid apparatus is at rest, and not involved in suctorial movements, the whole element is drawn back by powerful muscles, and lies behind Meckel's cartilage.

The coracoid, a cartilaginous, medial, unpaired element of the pectoral girdle, and involved in the origin of the depressor mandibulae and part of the geniocoracoideus muscles, forms early, along with the clavicle and cleithrum, thin curved bones that make up a major part of the pectoral girdle [24]. The occipital rib behind the pectoral girdle appears at stage 50. This element, the first of the ribs of the trunk and the largest in the series, is originally laid down in cartilage, and later ossifies perichondrally, while retaining cartilage at each extremity. The second rib of the trunk series is also enlarged compared with more posterior ribs. Trunk ribs, including the occipital rib, articulate with processes of cartilage on the posterior chondrocranium and the

notochord. The joints are amphiarthroses and the ribs may support the musculature but they cannot move independently [15]. Muscles surround the ribs, but are not attached.

The lower tooth plates are ankylosed to the prearticular bone on the inner surface of Meckel's cartilage in the mandible, supported by the angular and the splenial bones on the outer surface of Meckel's cartilage. Between the two prearticular bones is a wide gap. The most anterior ridge of the upper tooth plates fits within the gap dorsally during mastication, but does not occlude it. The hyoid apparatus of *N. forsteri* consists of five elements, all based on cartilage and all in articulation. The paired ceratohyal is large, sheathed in bone but retaining a core of cartilage, which extends beyond the bone at both ends. The posterior extension of this element carries the muscles that work to move the hyoid apparatus forwards, and the anterior extension articulates with the small spherical hypohyals, also paired, consisting entirely of cartilage. The single medial basihyal, also entirely composed of cartilage, articulates between the two hypohyals. When the hyoid apparatus is moved forwards, the tongue completely seals the gap between the two prearticular bones.

Development of the muscles that control jaw and hyoid movements proceeds alongside the appearance of skeletal elements. They begin to separate from the anterior myotomes by stage 41 [25, 26] and are functional when the hatchling starts to feed at stage 46. The muscle responsible for the opening of the mouth is the depressor mandibulae, a long, flat muscle, clearly visible, running ventrally along the floor of the oral cavity is shown in figure 1 and 2. It originates on the coracoid cartilage and on the clavicle, and inserts on the prearticular bones, covering the symphysis between the two bones. As it passes along the floor of the oral cavity, it lies close to but ventral to the geniocoracoideus muscle is shown in figure 1 and 2. Originating medially on the prearticular bones on either side, behind the tooth plates and reaching almost as far as the articulation with the quadrate, is a series of intermandibularis muscles is shown in figure 1 and 2, which have oblique fibres and insert on tissue in the mid line of the ventral oral cavity below the depressor mandibulae. Sub-terminal rotational grinding movements of the lower jaw tooth plates during mastication are carried out by the intermandibularis muscles. They are attached to the prearticular bones behind and below the tooth plates on each side, and reach back along the mandible close to the articulation with the quadrate is shown in figure 1 and 2. These muscles are responsible for the complex masticatory movements of the lower jaw dentition, mediated by the bicondylar articulation of the jaws. The upper jaw and the upper tooth plates are incapable of movement.
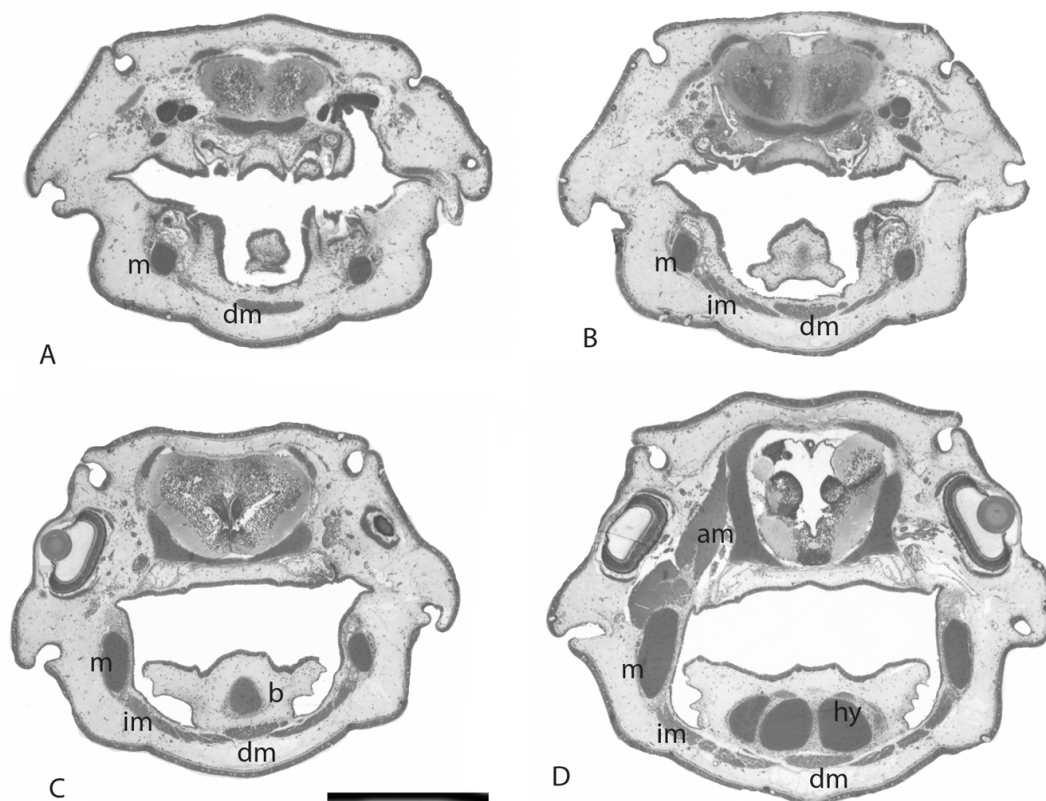

Figure 1: Sections of the stage 53 juvenile showing the muscles that operate the mandible. am adductor mandibularis muscle, b basihyal, dm depressor mandibularis muscle, im intermandibularis muscle, hy hypohyal, m mandible. Scale bar = 0.5 mm.

The mouth is closed by the action of the paired, massive adductor mandibulae muscles, which originate on the dorsolateral chondrocranium, and reach as far anteriorly as the posterior surface of the orbit is shown in figure 1 and 2. This muscle extends from the chondrocranium on each side and extends almost to the edge of the posterior chondrocranium is shown in figure 2A, close to the insertion of the epaxial muscles of the trunk. It is not attached to any osseous component of the head, only to the chondrocranium. This muscle is inserted on the posterior aspect of Meckel's cartilage is shown in figure 1 and 2. Behind the adductor mandibulae are the anterior epaxial muscles of the trunk, also originating on the chondrocranium is shown in figure 2A.
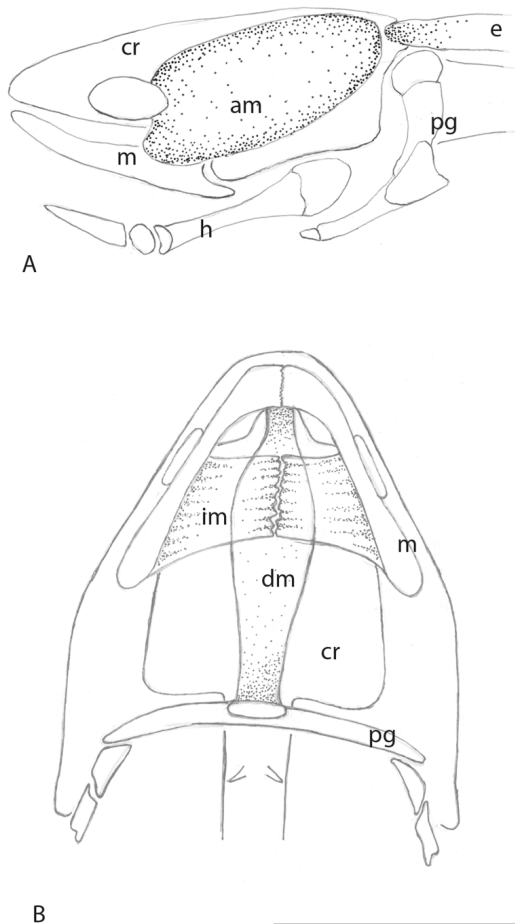

Figure 2: Muscles that operate the mandible. A. the single large muscle that closes the mouth. B. Muscles that open the mouth and permit grinding movements of the lower jaw. am, adductor mandibularis muscle, cr chondrocranioum, dm, depressor mandibularis muscle, e, epaxial muscle. h, hyoid, m, mandible, im, intermandibularis muscles, pg, pectoral girdle. Scale bar = 1 cm.

Muscles associated with the hyoid apparatus are larger than the muscles attached to the prearticular bones. The interhyoideus muscles, also in blocks and with oblique fibres, originate on the lateral surface along the shaft of the ceratohyal, and are inserted medially in tissues that surround the ceratohyal is shown in figure 3 and 4. These muscles are associated with the levator hyoideus muscle, which originates on the chondrocranium below the otic capsules, passes behind the opercular bones and inserts on

connective tissues surrounding the lateral surface of the posterior ceratohyal cartilage is shown in figure 3 and 4. A series of strips of muscle extend behind the levator hyoideus, and pass posteriorly within the operculum, to make up the constrictor hyoideus muscles is shown in figure 3 and 4. Interhyoideus muscles may contract to move the ceratohyal from side to side, and these muscles, aided by the levator hyoideus and the constrictor hyoideus muscles that extend from the interhyoideus is shown in figure 4, push the whole hyoid apparatus forwards, a movement that causes the basihyal to be inserted into the gap between the prearticular bones and Meckel's cartilage, sealing the space completely. This action facilitates suction of material into the oral cavity. In effect , the hyoid apparatus is enclosed by muscles, almost a single element but with two parts is shown in figure 4. Slow movements of the opercular folds to maintain a flow of water over the gills arise from separate contractions of the constrictor hyoideus, and movements of these muscles aid the action of the levator hyoideus. Levator hyoideus and constrictor hyoideus muscles pass behind the opercular bones and are not attached to these bones.

The geniocoracoideus muscle, which retracts the hyoid apparatus, is a massive paired muscle that is inserted on the base of the hypohyals and the anterior ceratohyal. Ventrally this muscle originates on the pectoral girdle, behind the insertion of the depressor mandibulae is shown in figure 4. Above the hypohyals and the shaft of the ceratohyal is the rectus cervicis muscle is shown in figure 4, attaching dorsally on each side of the hyoid apparatus. The geniocoracoideus and the rectus cervicis draw the hyoid apparatus back, and hold it in a resting position.

The process of suction, of food, air, water or mud, into the oral cavity is as follows. The constrictor hyoideus, the interhyoideus, and levator hyoideus muscles contract, and push the hyoid forwards, pressing the tongue, supported by the basihyal, into the gap in the mandible between the prearticular bones. The depressor mandibulae contracts, lowers the mandible and opens the mouth. Material is drawn into the oral cavity. The constrictor hyoideus, interhyoideus and the levator hyoideus muscles relax and the geniocoracoideus and rectus cervicis muscles contract, drawing the hyoid apparatus back into the resting position. The adductor mandibularis contracts, closing the mouth. Intermandibularis muscles move independently to break up the items of food.

Muscles surrounding the cranial rib are not attached to the rib, which cannot move. The only influence the cranial rib can have on the oral cavity and the hyoid apparatus is to anchor the elements of the oral cavity and hyoid apparatus, in conjunction with the pectoral girdle and the hypaxial musculature. This rib is not involved in suctorial actions of the jaws and hyoid apparatus.
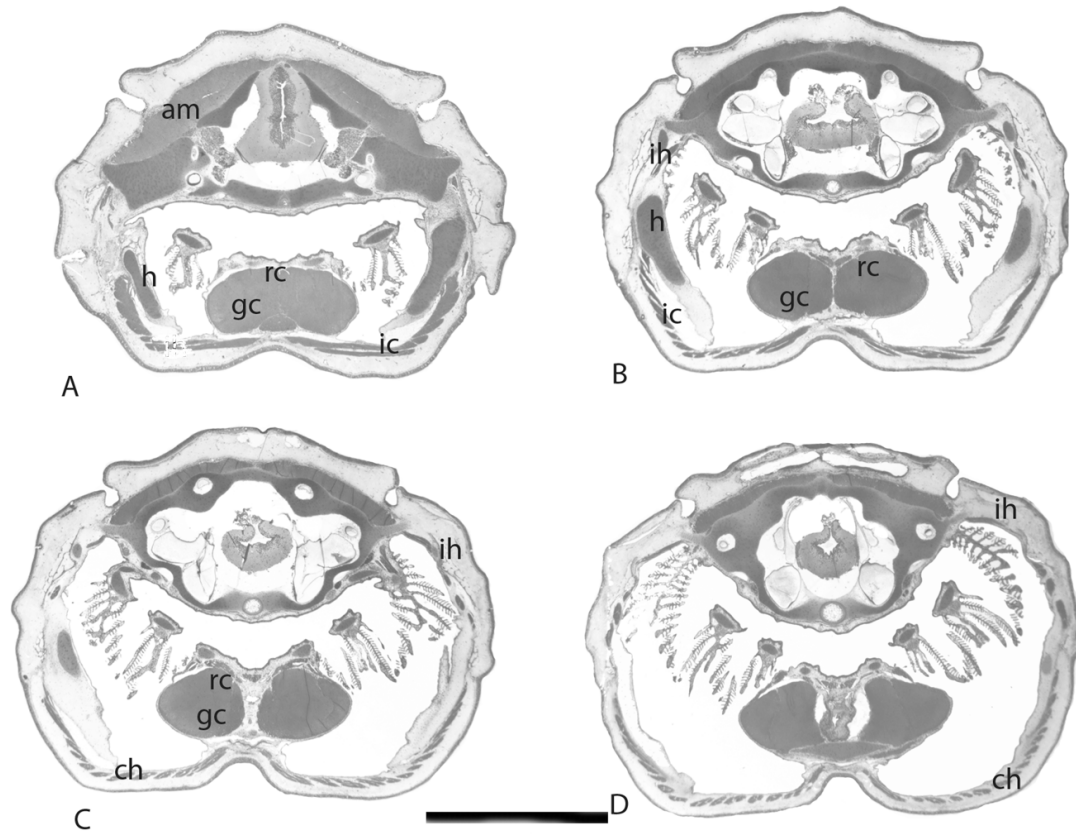
Figure 3: Sections of the stage 57 juvenile showing muscles that operate the hyoid apparatus. am, adductor mandibularis muscle, ch constrictor hyoideus, gc geniocoracoideus, h hyoid (ceratohyal), ic interceratohyal muscle, ih interhyoideus muscle, rc rectus cervicis. Scaler bar = 1 cm.

4. Discussion

Fossil dipnoans should not be seen as fundamentally different from living lungfish, and comparisons of functional anatomy among the different groups will enhance understanding of all dipnoans and their environments. There are many similarities in both ancient and living lungfish, as well as many differences, and comparisons can be both helpful and revealing. It is, after all, an ancient lineage, beginning in the Devonian and still with living representatives [7, 24, 27, 28].

The two groups of living lungfishes, neoceratodontids and lepidosirenids, are not the same, and similar differences can be traced in their closest fossil relatives, even as far back as the Palaeozoic [4, 8, 29, 30]. Mostly, the discrepancies relate to the structure of the skull and the dentition, but they can also be found in the muscular systems of the two groups [31, 32]. The skulls and jaw bones of *N. forsteri*, *L. paradoxa* and species of *Protopterus* contain the same elements, such as a cartilaginous chondrocranium, calvarial bones, tooth plates ankylosed to the jaw bones, a hyoid arch skeleton, pectoral girdle and cranial ribs [11, 12, 13, 15, 18, 33]. However, the arrangement, distribution and function of these elements differs in the two groups. Names of the elements of the skull roof differ depending on the interests of the authors describing the structures, with some using names that were originally designed for other vertebrates [8, 13, 26,
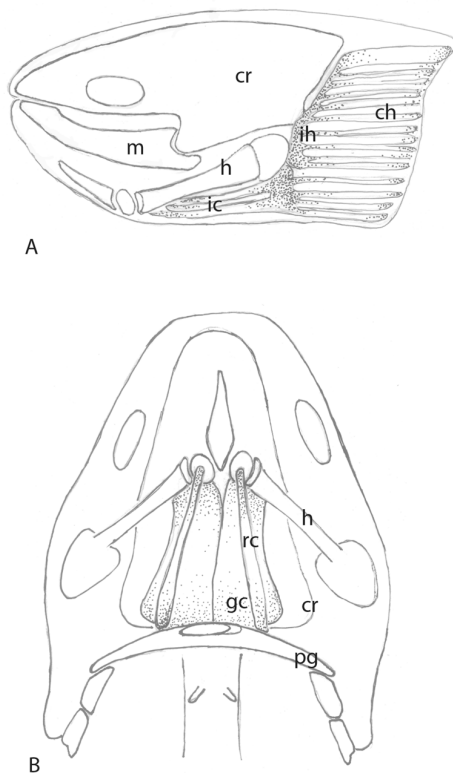

Figure 4: Muscles that operate the hyoid apparatus. A. Muscles that move the hyoid apparatus forwards. B. muscles that move the hyoid apparatus posteriorly into a resting position.

30, 31]. Other authors adopt a system of letters and names more appropriate for dipnoans [18, 33, 34].

The degree of ossification of the skull bones in the two major groups of living lungfishes differs, as does the shape and to a certain extent the function of the elements. In *N. forsteri*, the skull is essentially composed of a cartilaginous chondrocranium, with a calvarium consisting of thin bones in articulation with each other, separate from the chondrocranium, and the adductor mandibularis which closes the jaws, and the most anterior of the epaxial muscles, both originating on the posterior chondrocranium. The upper tooth plates are attached to the pterygopalatine bone, supported by the parasphenoid, and the vomer, situated just inside the upper lip, carries the small vomerine tooth plates. An ascending process from the pterygopalatine bone articulates with a lateral bone of the calvarium, designated the JLM bone [18], or the supraorbital bone [31]. This represents the only articular link between the calvarial bones and the underlying chondrocranium in this species. Meckel's cartilage, the major element of the mandible, remains cartilaginous throughout the life of the fish, as does the quadrate, an extension of the persistent chondrocranium.

According to Bemis [31], *Neoceratodus forsteri* does not have a depressor mandibulae muscle, to open the mouth, but this is not the case. Analysis of serial sections shows that a depressor mandibulae muscle is present, in the oral cavity between the two rami of the prearticular bone that carries the tooth plates, lying below the geniocoracoideus muscle, inserting in a more anterior position on the prearticular bones and originating on the bones of the pectoral girdle. This is not in the same position as the depressor mandibulae in *Lepidosiren* and *Protopterus* [31].

The living Australian lungfish is exceptional in that some of the muscles of the jaws and tongue are inserted only into soft tissues, not on bone or cartilage. Muscles in the jaw in *N. forsteri* appear to be rudimentary [25. 26] but the movements that are carried out are surprisingly versatile. Two muscles operate to open and close the jaws, the depressor mandibulae and the adductor mandibularis, and the lower tooth plates carry out subterminal grinding using small mandibular muscles attached to the prearticular bone. Large and powerful muscles in the throat move the hyoid apparatus back into a resting position, and a series of muscles attached to the ceratohyal push the tongue forwards to seal the gap between the lower jaw bones when the fish carries out suctorial movements of the oral cavity. In addition, movements of the operculum depend on the actions of the constrictor hyoideus muscles behind the ceratohyal, and associated with the interhyoideus muscle, to facilitate respiration by drawing water over the gills.

Lepidosirenids utilise different structures and mechanisms. The articulation between the upper and lower jaws is restrictive, not bicondylar as it is in *N. forsteri*, and is only capable of moving up and down. They have no basihyal, and no gap between the tooth plates of either the upper or lower jaws. Muscles of lepidosirenids include the same elements found in *N. forsteri* but the arrangements differ [31, 32], as do the size and relative importance of the muscles.

5. Conclusions

1. Two muscles operate to open and close the jaws in *N. forsteri*, the depressor mandibulae and the adductor mandibularis, and the lower tooth plates carry out subterminal grinding using small intermandibular muscles attached to the prearticular bone.

2. A series of muscles attached to the ceratohyal push the tongue forwards to seal the gap between the lower jaw bones when the fish carries out suctorial movements of the mouth. These include the muscles attached to the ceratohyal bone, as well as elements of the interhyoideus and the constrictor hyoideus muscles. Large and powerful muscles in the throat, the geniocoracoideus and rectus cervicis muscles, move the hyoid apparatus back into a resting position.

3. In addition, movements of the operculum depend on the actions of the constrictor hyoideus muscles behind the ceratohyal, and associated with the interhyoideus muscle, to facilitate respiration by drawing water over the gills.

References

[1] G. Krefft, "Description of a gigantic amphibian allied to the genus *Lepidosiren*, from the Wide-Bay District, Queensland." Proceedings of the Zoological Society of London Volume 1870, pp. 221 – 224. 1870.

[2] R. S. Miles, "Dipnoan (lungfish) skulls and the relationships of the group: a study based on new species from the Devonian of

Australia." Zoological Journal of the Linnean Society. 61, 1–328. 1977.

[3] L. Cavin, V. Suteethorn, E. Buffetaut, H. Tong, H., A new Thai Mesozoic lungfish (Sarcopterygii, Dipnoi) with an insight into post-Palaeozoic dipnoan evolution. Zoological Journal of the Linnean Society, Volume 149, pp. 141–177. 2007.

[4] A. Kemp, L. Cavin, G. Guinot, "Evolutionary history of lungfishes with a new phylogeny of post-Devonian genera." Palaeogeography, Palaeoclimatology, Palaeoecology, Paleontology. 4, 457–470. 2017.

[5] H.-P. Schultze, J. Chorn, "The Permo-Carboniferous genus Sagenodus and the beginning of modern lungfish." Contributions to Zoology. Volume 67, pp. 9–70. 1996.

[6] R. Owen, "Description of the Lepidosiren annectens." Transactions of the Linnean Society, Volume 18, pp. 327-361. 1839.

[7] H.-P. Schultze, "Fossilium Catalogus 1: Animalia, pars 131, Dipnoi." Kugler Publications, Amsterdam, New York. 1992.

[8] T. J. Challands, et al., 2019. "A lungfish survivor of the end-Devonian extinction and an Early Carboniferous dipnoan radiation." Journal of Systematic Palaeontology, https://doi:10.1080/14772019.2019.1572234. 2019.

[9] L. Lison, "Recherches sur la structure et l'histogenese des dents du poisons dipneustes." Archives de Biologie. 52, 279-320. 1941.

[10] A. Kemp, "Petrodentine in derived dipnoan dentitions." Journal of Vertebrate Paleontology, Volume 21, pp. 422-437. 2001.

[11] W. E. Agar, "The development of the skull and visceral arches in Lepidosiren and Protopterus." Transactions of the Royal Society of Edinburgh, Volume 45, pp. 49-64. 1906.

[12] T. W. Bridges, "On the morphology of the skull in the Paraguayan Lepidosiren and in other Dipnoids." Transactions of the Zoological Society of London, Volume 14, pp. 325-376. 1898.

[13] K. E. Criswell, "The comparative osteology and phylogenetic relationships of African and South American lungfishes (Sarcopterygii: Dipnoi)." Zoological Journal of the Linnean Society. Volume 174, pp. 801-858. 2015.

[14] H. S. Baird, "The occipital bones of the Dipnoi." Proceedings of the Royal Society of Victoria. 35 (N.S.), Part II,115-116. 1923.

[15] A. Kemp, "Adaptations to life in freshwater for Mioceratodus gregoryi, a lungfish from Redbank Plains, an Eocene locality in southeast Queensland, Australia." Alcheringa: An Australasian Journal of Palaeontology, Volume 42, pp. 305-310. 2018.

[16] A. Kemp, "Osteogenesis in the Australian lungfish. Neoceratodus forsteri (Osteichthyes:Dipnoi)." Australian Journal of Zoology. https://doi.org/10.1071/ZO22004. 2022.

[17] A. Kemp, "The embryological development of the Queensland lungfish, Neoceratodus forsteri (Krefft)." Memoirs of the Queensland Museum, Volume 20, pp. 553-597. 1982.

[18] A. Kemp, "Ontogeny of the skull of the Australian lungfish, Neoceratodus forsteri (Osteichthyes: Dipnoi)." Journal of Zoology. Volume 248, pp. 97-137. 1999.

[19] A. Kemp, "Changes in the freshwater environments of the Australian lungfish, Neoceratodus forsteri, in south east Queensland, and implications for the survival of the species." Proceedings of the Royal Society of Queensland, Volume 124, pp. 121 - 135. 2020.

[20] W. L. Kelly, M. Bryden, "A modified differential stain for cartilage and bone in whole mount preparations of mammalian foetuses and small vertebrates." Stain Technology, Volume 58, pp. 131-134. 1983.

[21] A. Kemp, "The role of epidermal cilia in development of the Australian lungfish, Neoceratodus forsteri (Osteichthyes: Dipnoi)." Journal of Morphology, Volume 228, pp. 203-221. 1996.

[22] A. Kemp, "Marginal tooth bearing bones in the lower jaw of the Recent Australian lungfish, Neoceratodus forsteri (Osteichthyes:Dipnoi)." Journal of Morphology, Volume 225, pp. 345- 355. 1995.

[23] A. Kemp, "Growth and hard tissue remodelling in the dentition of the Australian lungfish, Neoceratodus forsteri (Osteichthyes: Dipnoi)." Journal of Zoology, Volume 257, pp. 219-235. 2002.

[24] E. Jarvik, "Basic structure and evolution of vertebrates." Volume I. Academic Press, New York. 1980.

[25] F. H. Edgeworth, "On the development of the hypobranchial, branchial and laryngeal muscles of Ceratodus, with a note on the development of the quadrate and epihyal." Quarterly Journal of Microscopical Science, new series, Volume 67, pp. 325-368. 1923.

[26] F. H. Edgeworth, "The Cranial Muscles of Vertebrates." Cambridge: Cambridge University Press. 1935.

[27] R. H. Denison, "Early Devonian lungfishes from Wyoming, Utah and Idaho." Fieldiana: Geology, Volume 17, pp. 353 – 413. 1968.

[28] W. Gross, "Ueber Crossopterygier und Dipnoer aus dem Baltischen Oberdevon im Zusammenhang einer vergliechenden Untersuchung des Porencanalsystems palaozoicher Agnathen und Fische." Kungliga Svenska Vetenskaps Akademiens Handlingar. Volume 5, pp. 1-140. 1956.

[29] T. J. Challands, et al. "Mandibular musculature constrains brain – endocast disparity between sarcopterygians." Royal Society Open Science, 7, 200933. http://dx.doi.org/10.1098/rsos.200933. 2020.

[30] J. D. Pardo, et al. "An exceptionally preserved transitional lungfish from the Lower Permian of Nebraska, USA, and the origin of modern lungfishes." PLoS ONE 9, e108542. 2014.

[31] W. E. Bemis, "Feeding systems of living dipnoi: anatomy and function." Journal of Morphology, supplement 1 , 249-275. 1987.

[32] W. E. Bemis, G. V. Lauder, "Morphology and function of the feeding apparatus of Lepidosiren paradoxa (Dipnoi)." Journal of Morphology, Volume 187, pp. 81- 108. 1984.

[33] A. Kemp, "Skull Structure in Post-Paleozoic Lungfish." Journal of Vertebrate Paleontology, Volume 18, pp. 43-63. 1998.

[34] A. S. Romer, "The dipnoan cranial roof." American Journal of Science. Volume 32, pp. 241-256. 1936.

Robust Localization Algorithm for Indoor Robots Based on the Branch-and-Bound Strategy

Huaxi (Yulin) Zhang[1], Yuyang Wang[2], Xiaochuan Luo[*,3], Baptiste Mereaux[4], Lei Zhang[5]

[1]LTI, Université de Picardie Jules Verne, Saint Quentin, 02100, France

[2]Shanghai Research Institute for Intelligent Autonomous Systems, Tongji University, Shanghai, 201210, China

[3]College of Information Science and Engineering,Northeastern University, Shenyang, 110819, China

[4]Independent Researcher, Saint Quentin, 02100, France

[5]euroDAO S.A.S., Saint Quentin, 02100, France

[*]Corresponding author: Xiaochuan Luo, Northeastern University, Shenyang, 110819, China, Contact Email: luoxch@mail.neu.edu.cn

ABSTRACT: Robust and accurate localization is crucial for mobile robot navigation in complex indoor environments. This paper introduces a robust and integrated robot localization algorithm designed for such environments. The proposed algorithm, named Branch-and-Bound for Robust Localization (BB-RL), introduces an innovative approach that seamlessly integrates global localization, position tracking, and resolution of the kidnapped robot problem into a single, comprehensive framework. The process of global localization in BB-RL involves a two-stage matching approach, moving from a broad to a more detailed analysis. This method combines a branch-and-bound algorithm with an iterative nearest point algorithm, allowing for an accurate initial estimation of the robot's position. For ongoing position tracking, BB-RL uses a local map-based scan matching technique. To address inaccuracies that accumulate over time in the local maps, the algorithm creates a pose graph which helps in loop-closure optimization. Additionally, to make loop-closure detection less computationally intensive, the branch-and-bound algorithm is used to speed up finding loop constraints. A key feature of BB-RL is its Finite State Machine (FSM)-based relocalization judgment method, which is designed to quickly identify and resolve the kidnapped robot problem. This enhances the reliability of the localization process. BB-RL's performance was thoroughly tested in real-world situations using commercially available logistics robots. These tests showed that BB-RL is fast, accurate, and robust, making it a practical solution for indoor robot localization.

KEYWORDS Branch-and-bound, Global localization, Position tracking, Robot kidnapping

1. Introduction

The growing demand for mobile robots in tasks such as repair, transportation, and cleaning necessitates the development of efficient techniques for robot localization [1]–[5]. Particularly in known environments, robots should be able to localize themselves within a prebuilt map, enabling them to position themselves based on data collected from various sensors. The problem of localizing mobile robots in indoor environments can be categorized into three sub-problems: position tracking, global localization, and the kidnapped robot problem [6, 7]. This paper proposes a fast, robust, and accurate algorithm to achieve indoor localization of mobile robots, effectively solving the three localization sub-problems simultaneously in real-world applications.

Recent advancements in indoor robot localization research have shown significant progress, yet challenges remain in simultaneously addressing three critical localization issues. The first issue involves global localization. Often, an initial pose is determined by observing the robot's approximate position in the environment to reduce compu-

tational effort and maintain localization stability. Despite this, without an initial estimate, achieving desirable global localization remains difficult.

The second issue is position tracking. Here, the challenge lies in the timely elimination of accumulated errors. To address this, two main strategies are employed. The first is simultaneous localization and mapping (SLAM), which involves frontend scan matching and backend optimization. While effective, SLAM methods are computationally demanding and rely on loop-closure detection to correct errors. The second strategy involves odometry, such as visual or LiDAR odometry, which calculates the robot's relative pose incrementally using adjacent data. However, these methods are prone to error accumulation over time, making them suitable primarily for short-term tracking.

Finally, the third issue is the kidnapped robot problem. This occurs when a robot, initially well-localized, is unexpectedly moved to an unknown location. This problem can be split into two scenarios: real kidnapping, where the robot is physically relocated by external forces such as

human intervention or an accident, and perceived kidnapping, which results from localization failures. Addressing this issue effectively remains a challenge for most existing approaches.

Considering these aspects, we propose a robust and accurate robot localization algorithm, which consists of three parts: global localization, position tracking, and relocalization judgment.

- The *global localization algorithm*, which is used to determine the robot's initial pose, can be divided into two stages. In the coarse matching stage, the branch-and-bound algorithm based on depth-first search (DFS) is used to promptly identify the absolute position of the robot on the map without any initial estimate. In the fine matching stage, the iterative nearest point algorithm is used to perform iterative optimization to determine the optimal initial pose of the robot. This algorithm can rapidly converge anywhere on the map, and the robot pose exhibits global optimality.

- The *position tracking algorithm* is used for the continuous localization of the robot when the initial pose is known. A local map-based scan matching method is used to estimate the relative pose of the robot and simultaneously build a local map. Moreover, a global pose graph optimization algorithm is used to eliminate the accumulated errors between local maps. Additionally, to ensure that the computing time is nonintractable, a DFS-based branch-and-bound algorithm is used to accelerate the process of identifying the loop constraints.

- The *relocalization judgment algorithm* is used to address the problem of robot kidnapping and eliminate the accumulated errors of the robot. We propose an FSM-based relocalization judgment method based on confidence calculation and dual-threshold judgment to effectively monitor the localization status of the robot. When the calculated confidence is less than the minimum threshold, the global localization algorithm is invoked for localization recovery.

The main contributions of this research can be summarized as follows:

1. *Development of a Two-Stage Global Localization Algorithm*: We introduce a novel two-stage global localization algorithm that combines the broad search capabilities of the branch-and-bound algorithm with the local optimization efficiency of the iterative closest point algorithm. This ensures the robot quickly identifies the globally optimal initial pose without relying on any preliminary estimates.

2. *Establishment of a Position Tracking Algorithm*: Our research incorporates a position tracking algorithm that integrates frontend local map-based scan matching with backend pose graph optimization. This approach provides a highly accurate state estimation of the robot, crucial for precise navigation.

3. *Creation of an FSM-based Relocalization Judgment Algorithm*: We have developed an innovative FSM-based

relocalization judgment algorithm that utilizes an inflated occupancy grid map to minimize the impact of sensor measurement noise. This algorithm is adept at efficiently detecting instances of robot kidnapping, thereby safeguarding against localization failures in diverse scenarios and ensuring swift and effective localization recovery.

4. *Proposal of a Joint Localization Algorithm*: The research culminates in a comprehensive joint localization algorithm capable of concurrently addressing the challenges of global localization, position tracking, and robot kidnapping in indoor settings. The efficacy of this algorithm has been rigorously validated using commercial logistics robots, demonstrating its successful application in real-world environments.

2. Related work

Consistent and efficient localization is a core concept of indoor robot navigation, as knowledge of the robot position is crucial in deciding future actions [8]. In recent years, several researchers have focused on indoor robot localization [9]. However, most of the existing approaches focus on solving a specific problem of localization (such as global localization), which is fundamentally different from the motivation of our work.

Localization refers to the procedure of determining the robot pose with respect to its environment by using various noisy sensors. According to the type of measurement data, the sensors used in the process of robot localization can be divided into two classes: proprioceptive sensors and exteroceptive sensors. Proprioceptive sensors (such as encoders and IMUs) measure the robot motion by using deduced reckoning to calculate the relative robot displacement [10]–[12]. Since such sensors consider the instantaneous speed or acceleration to estimate the robot state, the integrated error in the localization process increases in a nonbounded manner over time. Hence, such sensors are usually used in combination with exteroceptive sensors that can determine the absolute positions to enhance the robot's ability in managing uncertainties [13]–[16]. Proprioceptive sensors address position tracking issues due to their inability to sense environmental information.

In addition to the methods based on proprioceptive sensors for localization, several approaches use exteroceptive sensors to recognize the environment around a robot to estimate the robot location. Among these methods, SLAM is widely used. In terms of the primary type of adopted sensor, the SLAM algorithm can be divided into two classes: visual SLAM and LiDAR SLAM. Visual SLAM aims to address the pose estimation of cameras with visual information. This method has evolved from the use of monocular cameras [17] to stereo cameras [18] and depth cameras [19]. The classic variants of monocular SLAM include ORB-SLAM [20], DSO [21], LSD-SLAM [22], and SVO [23]. Certain researchers, [24] adapted ORB-SLAM to a fisheye camera, tightly coupled visual information and IMU data to robustly estimate the camera pose and used the multimap technology to effectively solve the problem

of localization failure. In another study [25], a rolling-shutter camera and IMU were tightly coupled to minimize the photometric error to estimate the robot pose. Other researchers [26, 27, 28] used deep neural networks to eliminate the scale ambiguity of monocular cameras and extract high-level semantic features to enhance the system robustness and accuracy. The classic variants of stereo SLAM include ORBSLAM2 [29], ORBSLAM3 [30], PL-SLAM [31], and SOFT2 [32]. An event camera [33] was used to address the problems of high dynamics and low light, and the depth estimation of multiple viewpoints was merged in a probabilistic manner to build a semidense point cloud map. Notable research on RGB-D SLAM includes that on the RTAB-MAP [34], bundle fusion [35], and Kintinuous [36]. Moreover, a lightweight semantic network model was proposed [37], which integrates multiple technologies such as VIO, pose graph optimization, and semantic segmentation, to achieve the high-precision reconstruction of the three-dimensional environment. Deep learning techniques have also been employed in visual SLAM to extract features, enhancing the algorithm's ability to interpret and understand the visual information as in LIFT-SLAM [38] and Object-Fusion [39]. Because depth cameras can directly obtain the depth information of the environment, their use has been widely considered [40]. However, processing of the depth data is computationally expensive, and it is difficult to satisfy the real-time operation requirements of the CPU. Moreover, the frontend odometry aspects of visual SLAM can only estimate the relative pose of the robot, and back-end loop-closure detection can only achieve relocalization in similar scenes. Therefore, this approach cannot realize global localization.

LiDAR SLAM can be divided into 2D LiDAR SLAM and 3D LiDAR SLAM according to the type of LiDAR used. The classic 3D LiDAR SLAM algorithms include LOAM [41], HDL graph slam [42], and SuMa++ [43]. LOAM exhibits a high performance on the KITTI dataset, and thus, many improved versions of this algorithm have been proposed. In [44], the distinctive edge features and planar features were extracted to achieve two-step Levenberg–Marquardt optimization. In [45], the LiDAR and IMU data were tightly coupled. The IMU preintegration factor was introduced in the pose graph optimization to update the bias of the IMU, and the accumulated errors were corrected through loop-closure detection. Moreover, excellent schemes for 2D LiDAR SLAM have been proposed in recent years. The classic filter-based algorithms include Fast SLAM [46] and Gmapping [47], and graph-based algorithms include Karto SLAM [48] and Cartographer [49]. Cartographer, developed by Google engineers, has been proven to be a complete SLAM system that integrates localization, mapping, and loop-closure detection. At the frontend of this algorithm, the relative pose of the robot is calculated using the scan-to-submap matching method, which has a significantly lower accumulated error than the scan-to-scan matching method [50]. Additionally, compared with the scan-to-map matching method [51], it is considerably less computationally intensive and can run in real time. Similarly, since the origin of the robot localization is determined when initializing the algorithm, LiDAR SLAM is essentially an odometry

technique and cannot solve the problems of global localization and robot kidnapping. To realize indoor localization, 2D LiDAR has been widely used due to its cost and accuracy. Certain researchers [52] and [53] attempted to enhance the accuracy of their localization system by using the extended Kalman filter to achieve multisensor fusion. However, these approaches cannot solve the problems of global localization and robot kidnapping. In [54], a quasistandardized 2D dynamic time warping (QS-2DDTW) method was proposed to solve the problem of robot kidnapping. The approach uses scan data for two consecutive ranges to obtain the geometric shape similarity of the environment to determine the robot state. Nevertheless, this approach cannot solve the position tracking problem. However, other studies [55]–[59] addressed the three major localization problems by using the adaptive Monte Carlo localization algorithm. Notably, using only ultrasonic sensors, the localization accuracy of the order of decimeters can be achieved.

In addition to the two types of exteroceptive sensors for localization, several wireless devices (such as WiFi, UWB, Bluetooth, and RFID) can be deployed indoors to realize reliable localization. In [60] and [61], the Kalman filter was used to fuse IMU and UWB data to obtain a relatively accurate robot pose. However, these approaches could not solve the problems of global localization and robot kidnapping. In addition, high accuracy localization was achieved using commercial WiFi devices [62]. The robust principal component analysis for extreme learning machine algorithm (RPCA-ELM) could suppress the effect of measurement noise in the localization process. In [63] and [64], to enhance the robustness of localization, UHF radio frequency identification technology was adopted. However, the system accuracy depended on the RFID tag, and global localization could not be realized at arbitrary positions. Furthermore, localization was realized in [65] and [66] by deploying a set of photoresistor sensors on a robot to collect information regarding an LED array in the environment. However, high-precision position tracking could not be realized. In addition, a robot localization system based on asynchronous millimeter-wave radar interference was proposed [67], which used the interference between multiple millimeter-wave radars with known positions in the environment to calculate the position of the robot. However, the system exhibited limited localization accuracy.

In summarizing the state of the art in indoor robot localization, it is clear that researchers have made significant strides using a variety of methodologies and sensor technologies. From SLAM implementations—both visual and LiDAR-based—to sophisticated sensor fusion techniques leveraging proprioceptive and exteroceptive sensors, including the use of wireless technologies like WiFi, UWB, Bluetooth, and RFID to enhance localization capabilities, each method aims to address specific facets of the complex challenge of localization, focusing on global localization, position tracking, or resolving the kidnapped robot problem.

Despite these advances, a comprehensive solution that simultaneously addresses all three critical challenges of indoor robot localization remains elusive. Existing studies tend to focus on optimizing specific aspects of localization rather than offering a unified algorithm capable of han-

dling global localization, precise position tracking, and the kidnapped robot scenario in an integrated manner. This gap in the research landscape underscores the innovative potential of the proposed BB-RL algorithm, which aims to provide a holistic approach to the multifaceted problem of autonomous indoor navigation. By doing so, BB-RL aspires to establish a new method in the field, offering a more robust, accurate, and comprehensive solution to indoor robot localization than currently available methods.

Some literature mentions studies that attempt to address all three major localization challenges simultaneously using the Adaptive Monte Carlo Localization algorithm [55]–[59]. These studies illustrate the potential of multi-sensor fusion and intelligent algorithms to enhance indoor localization accuracy and robustness. However, despite offering a composite solution, these approaches may still face limitations in practical application, such as dependency on specific types of sensors, the impact of environmental complexity on localization accuracy, and challenges in maintaining high precision in dynamic and unknown environments.

The Self-Adaptive Monte Carlo Localization (SA-MCL) method represents an advancement in addressing the inherent challenges of robot localization, including global localization, position tracking, and the "kidnapping" problem, where a robot is moved to an unknown location. Previous studies have shown that by employing the adaptive Monte Carlo localization algorithm, significant strides can be made in solving these three major localization challenges. These methods, however, are predominantly based on 2D environments and utilize ultrasonic sensors for sensing.

Transitioning from 2D to 3D environments introduces new challenges for the Monte Carlo Localization (MCL) algorithm. In [68], the authors propose a pure 3D MCL localization algorithm to address these challenges directly. Meanwhile, other approaches, such as the one by [69], adapt 2D MCL for localization in 3D maps. These methods illustrate the diversity of strategies being explored to solve localization problems in three-dimensional spaces using the MCL framework in 3D Map. The demand for computational resources and memory usage significantly increases in 3D Monte Carlo localization due to the necessity to process and track a much larger number of particles to accurately estimate a robot's pose in three-dimensional space. Each particle's position, orientation, and weight must be maintained, leading to escalated memory requirements as the particle count increases. Furthermore, without prior knowledge of the robot's approximate location, distributing particles effectively throughout the three-dimensional space to ensure comprehensive coverage and, by extension, the accuracy of the localization process, presents a considerable challenge. This challenge underscores the complexity of initializing the algorithm in 3D spaces, which is vital for the successful application of Monte Carlo localization methods in more complex environments.

In [70], the authors developed a branch-and-bound (BnB)-based 2D scan matching technique utilizing hierarchical occupancy grid maps of varying sizes. While this approach provides accurate and fast global localization on 2D maps, its processing time significantly increases when applied to 3D maps. In [71], the authors advanced this

research by introducing a BnB-based method for 3D global localization, which more effectively addresses the challenges of extending the work of [70] to three-dimensional environments. However, these studies primarily focus on global localization issues without offering an integrated solution.

In summary, despite attempts to address the three major localization challenges simultaneously and the existence of various methods focusing on solving specific issues, there remains a significant research gap in developing an accurate and robust comprehensive localization system. This highlights the importance and innovative value of proposing new algorithms, such as the BB-RL algorithm introduced in this paper, aimed at enhancing the performance of indoor robot localization. The BB-RL algorithm seeks to overcome the limitations of existing solutions through innovative techniques and methods, providing a more comprehensive and effective solution to meet the demands of complex indoor environments for robot navigation.

3. System overview

3.1. Hardware setting

The hardware settings are shown in Figure 1. The adopted autonomous mobile robot (AMR) is a commercial differential wheeled logistics robot, model IR300, which is equipped with an Intel NUC8BEH minicomputer as the computing platform of the robot; two SICK TIM561 LiDAR for range measurements, which are deployed diagonally on the left front and bottom right of the robot and have a measurement frequency of up to 10 Hz; an inertial measurement unit model LMPS-be1, which is used for high-frequency linear acceleration and angular velocity measurement and can exhibit a measurement frequency of up to 200 Hz; two wheel encoders, which are used to measure the wheel speed with a measurement frequency of up to 50 Hz.

3.2. System architecture

The system architecture of the proposed algorithm is shown in Figure 2. The algorithm is composed of three parts: global localization, position tracking, and relocalization judgment.

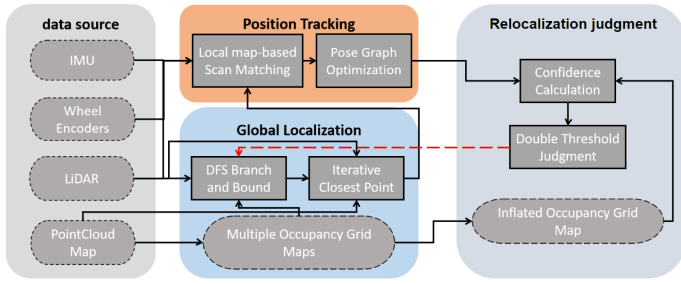Figure 1: IR300 robot, manufactured by Sunspeed Robotics Ltd, Co.

Figure 2: System architecture

In the localization process, we first obtain the robot's initial pose in the environment through the global localization algorithm, which is a two-stage matching algorithm composed of a branch-and-bound algorithm and an iterative closest point algorithm. After determining the robot's initial pose, we implement the position tracking algorithm, which uses the initial pose as the robot's initial state to realize local map-based scan matching. To effectively eliminate the accumulated errors between local maps, we maintain a global pose graph at the backend of the algorithm. When a valid loop closure is detected, the algorithm is implemented to correct the accumulated errors. Finally, we use a single thread to implement the relocalization judgment algorithm to monitor whether the robot can be located correctly when the position tracking algorithm is used. When the confidence of the current localization result is less than the set dual-thresholds, the global localization algorithm is called to reinitialize the algorithm.

4. Global Localization

Global localization, as an indispensable part of our algorithm, is mainly used to determine the robot's initial pose and ensure localization recovery when the robot is kidnapped. When the algorithm is implemented, we first convert the prebuilt point cloud map into multiple occupancy grid maps with different resolutions. Subsequently, we use the DFS-based branch-and-bound algorithm to accelerate the matching of the current LiDAR data with the occupancy grid maps. Finally, the iterative nearest point algorithm is used to continue the optimization on the computational results of the DFS-based branch-and-bound algorithm and ensure rapid convergence to obtain the optimal pose of the robot.

4.1. Global search using the branch-and-bound algorithm

We formulate global localization as a search problem on the occupancy grid map. The linear and angular search window sizes can be easily determined according to the map size. To ensure the search accuracy, we set the linear step size as the grid size. The angular step size can ensure that the farthest LiDAR point s_{max} moves once without exceeding the map resolution r. Thus, the angular step size ε can be estimated using the following equation:

$$\varepsilon = \arccos\left(1 - \frac{r^2}{2s_{max}^2}\right) \tag{1}$$

Furthermore, the integral number of steps covering the set linear and angular search window sizes can be computed as:

$$s_x = \left\lceil \frac{S_x}{r} \right\rceil, s_y = \left\lceil \frac{S_y}{r} \right\rceil, s_\theta = \left\lceil \frac{S_\theta}{\varepsilon} \right\rceil \tag{2}$$

where S_x and S_y are the linear search window sizes in the x- and y-directions, respectively. S_θ is the angular search window size. s_x and s_y are the integral numbers of the linear steps in the x- and y-directions, respectively, and s_θ is the integral number of the angular steps. If the center of the occupancy grid map is assumed to be the origin of the search process, the search set can be defined as:

$$W = \left\{-\frac{1}{2}s_x, ..., \frac{1}{2}s_x\right\} \times \left\{-\frac{1}{2}s_y, ..., \frac{1}{2}s_y\right\} \times \left\{-\frac{1}{2}s_\theta, ..., \frac{1}{2}s_\theta\right\} \tag{3}$$

Because the time to search an occupancy grid map increases exponentially with increasing map size, we apply the branch-and-bound algorithm to accelerate the search process. In practical applications, we build a global search tree to determine the initial pose for a given occupancy grid map, where each node in the tree represents a search result. The map search process is converted into node transversal in the search tree, and the target is to identify the leaf node with the best score.

In contrast to the breadth-first search-based branch-and-bound algorithm, which traverses most of the nodes in the search tree to identify the leaf node with the best score, we use the DFS-based branch-and-bound algorithm to promptly evaluate the nodes by performing a layer-by-layer search on multiple occupancy grid maps with low to high resolutions and prune the intermediate nodes that do not meet the boundary conditions and all the corresponding subnodes. Therefore, only a few nodes need to be traversed to identify a leaf node with the best score. The flow of the algorithm is illustrated in Figure 3.

Schematic of the DFS-based Branch-and-Bound Method (Search Tree Depth $d = 3$). The root node is implicitly divided into different subnodes to form a set N_0, and a node n_0 is extracted to illustrate the algorithmic process.

First, we use the prebuilt point cloud map to create multiple occupancy grid maps with high to low resolutions. Specifically, we first rasterize the point cloud map according to the required highest resolution r_0. The probability value of each grid is averaged according to the number of point clouds in the grid, and the resulting occupancy grid map is denoted as map_0. Subsequently, according to the depth d of the global search tree, map_0 is downsampled $d - 1$ times. The resolution of $map_i, i = 1, ..., d-1$ obtained by each downsampling is doubled to $2^i r_0$. Finally, we save these maps from low to high resolutions.
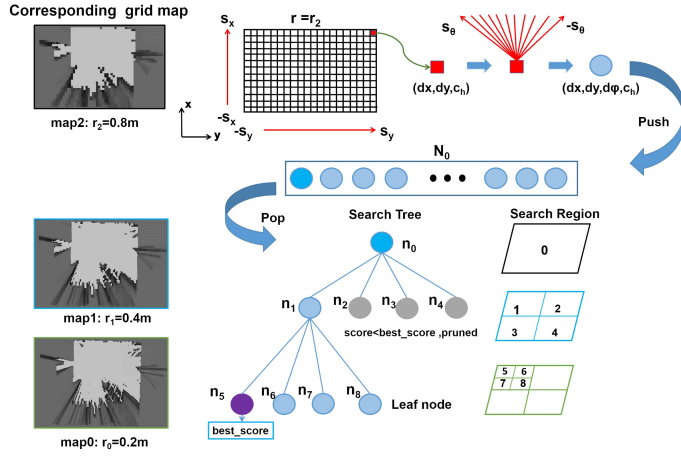
Figure 3: Schematic of the DFS-based branch-and-bound method (search tree depth d 3). The root node is implicitly divided into different subnodes to form a set N_0, and a node n_0 is extracted to illustrate the algorithmic process.

Second, we consider the search strategy. In the global search tree, the root node corresponds to the set of all possible solutions. We do not explicitly express this node but only branch it into a series of child nodes, which can be denoted as the set N_0 of all possible solutions searched on map_{d-1}. The leaf nodes represent a possible solution searched on map_0. Each node n_i in the tree is represented as a tuple of integers:

$$n_i \quad dx, dy, d\varphi, c_h \tag{4}$$

where dx and dy represent the position offsets in the x- and y-directions relative to the origin of the search process, respectively. $d\varphi$ is the rotation offset relative to the positive direction of the search process, and c_h represents the height of the search tree in which the node is located. Each node in the search tree is defined as a search area with a certain boundary.

Each node with $c_h > 1$ can branch into four child nodes of height $c_h - 1$:

$$N_n \quad \{2dx, 2dx \ 1\} \times \{2dy, 2dy \ 1\} \times \{d\varphi\} \times \{c_h - 1\} \tag{5}$$

For each leaf node with c_h 0, branching cannot continue to generate new nodes. Thus, the search pose corresponding to the leaf node is a possible solution. When the leaf node with the best score is found, the optimal solution to the problem can be expressed as

$$\xi_n^* \quad r_0 dx, r_0 dy, \varepsilon d\varphi \tag{6}$$

Finally, the upper bound calculation strategy is implemented. An excellent upper bound can help promptly identify the optimal solution to the problem. To ensure the accuracy of the upper bound, when building multiple occupancy grid maps with low to high resolutions, the probability value of each grid in $map_i i \quad 1, ..., d - 1$ is the maximum probability value of the corresponding $2^i \times 2^i$ grids in map_0. Therefore, the grids on the occupancy grid map with a lower resolution have a higher probability value:

$$S core n \quad \sum_{i1}^{N} F_{Multimap}^{c_h} T_{\xi_n} s_i \tag{7}$$

where $F_{Multimap}^{c_h}$ transforms the LiDAR point to the map frame to obtain the probability of the corresponding grid according to the prebuilt multiple occupancy grid maps. The search process is essentially a table lookup process, and thus, the computational complexity of the algorithm is always maintained in a constant range. The specific steps of the algorithm are shown in Algorithm 1.

Algorithm 1: Branch-and-bound Algorithm Based on Depth First Search.

Input: current period t, current scan S_t, point cloud map m_p

Parameters: search tree depth d, search window sizes S_x, S_y, S_θ, occupancy grid map highest resolution r_0

Output: robot initial guess ξ_n^*

Convert point cloud map m_p to multiple occupancy grid maps;
$s_x \leftarrow \lceil S_x r_{d-1} \rceil$;
$s_y \leftarrow \lceil S_y r_{d-1} \rceil$;
$\varepsilon \leftarrow \arccos 1 - r_0^2 2 s_{max}^2$;
$s_\theta \leftarrow \lceil S_\theta \varepsilon \rceil$;
$best\_score \leftarrow 0$;
$c_h \leftarrow d - 1$;
for $j_x \leftarrow -s_x$ **to** s_x **do**
    for $j_y \leftarrow -s_y$ **to** s_y **do**
        for $j_\theta \leftarrow -s_\theta$ **to** s_θ **do**
            $n \leftarrow j_x, j_y, j_\theta, c_h$;
            Push n into N_0;
        end
    end
end
initialization;
Initialize a priority queue N to save each node in N_0 according to the score;
while $N \neq empty$ **do**
    Pop the node n with the beat score from N;
end
if $S core n > best\_score$ **then**
    if n *is a leaf node* **then**
        $\xi_n^* \leftarrow \xi_n$;
        $best\_score \leftarrow S core n$;
    end
    else
        Split $n \rightarrow N_n$:
        $\{2dx, 2dx \ 1\} \times \{2dy, 2dy \ 1\} \times \{d\varphi\} \times \{c_h - 1\}$;
        Compute the score of each node in N_n;
        Store each node in N_n into N according to the score;
    end
end

4.2. Optimization of the initial pose using the iterative nearest point algorithm

Although the pose ξ_n^* specified by the DFS-based branch-and-bound algorithm has global optimality, the final search accuracy is inevitably limited by the highest resolution of the occupancy grid map. Hence, we use the iterative closest

point algorithm to further optimize ξ_n^*.

The iterative nearest point algorithm calculates the rigid transformation matrix between the two sets of point clouds in an iterative manner. We convert the matching problem between the two sets of point clouds into a nonlinear least squares problem and iteratively compute the rigid transformation matrix around the initial value ξ_n^*. We assume that the robot pose in the iterative process is $\xi (x, y, \varphi)$, the point in the point cloud map is p_i', the current LiDAR point is p_i, and the error function e is defined as

$$e(\xi) = \arg\min \frac{1}{2} \sum_{i=1}^{N} \left\| p_i - \exp(\xi^\wedge) p_i' \right\|_2^2 \tag{8}$$

where $\exp(\cdot)$ represents the exponential mapping of $so3 \to SO3$. We can use iterative algorithms (e.g., Gauss–Newton and Levenberg–Marquardt) to solve this problem. The Jacobian matrix of the iterative update process can be expressed as follows:

$$\frac{\partial e}{\partial \delta \xi} = \left[-I \quad \exp(\xi^\wedge) p_i'^\wedge \right] \tag{9}$$

The convergence speed of the iterative nearest point algorithm is affected by the maximum number of iterations and the robot pose difference calculated by two consecutive iterations. When the algorithm is used on hardware-constrained robot platforms, and it is necessary to consider the operating efficiency and localization accuracy, the convergence conditions can be alleviated. Our algorithm provides a satisfactory initial guess. Additionally, the number of point clouds involved in the matching is small. Hence, the convergence condition can be met after several iterations.

5. Position Tracking

The position tracking algorithm is of significance in enhancing the performance of the localization algorithm, especially in challenging circumstances such as those involving map expiration or environmental changes due to dynamic obstacles. In this paper, we use a scan matching method that aligns the current LiDAR data with the local map. The local map contains a certain number of LiDAR frames, which are expressed in an occupancy grid map. The map is updated continuously with each new LiDAR data. When the local map is built, it is added to the backend pose graph for optimization. The accumulated errors are corrected with the introduction of loop constraints to ensure the accuracy of the position tracking algorithm.

5.1. Frontend local map-based scan matching

The matching process involves inserting the current LiDAR data into the appropriate position in the local map. We formulate this process as a local nonlinear optimization problem, in which the LiDAR pose is optimized relative to the current local map. The problem is solved using the Gauss–Newton method. By iteratively optimizing the error function, a LiDAR pose with the highest probability is identified. In the optimization problem, T_ξ denotes the transformation matrix that transforms the LiDAR data into the local map. The error function can be expressed as:

$$E(\xi) = \arg\min \sum_{i=1}^{N} \left[1 - F(T_\xi s_i) \right]^2 \tag{10}$$

where $F : R_2 \to R$ represents a bicubic interpolation function that smooths the sum of the probability values of each LiDAR point in the local map. Specifically, we assume that $T_\xi s$ is defined as a point x, y in the two-dimensional plane. In this case, the bicubic interpolation function is:

$$F(x, y) = \sum_{i=1}^{3} \sum_{j=0}^{3} f(x_i, y_j) W(x - x_i) W(y - y_j) \tag{11}$$

where $f(x_i, y_j)$ is the probability of the four neighborhoods x_i, y_j around the point x, y, and $W(\cdot)$ represents the weight of the x_i, y_j interpolation on x, y, computed as:

$$W(x) = \begin{cases} (a + 2)|x|^3 - (a + 3)|x|^2 + 1 & for |x| \le 1 \\ a|x|^3 - 5a|x|^2 + 8a|x| - 4a & for 1 < |x| < 2 \\ 0 & otherwise \end{cases} \tag{12}$$

where a takes values in the range $[-0.75, -0.5]$. Solving $E(\xi)$ is a local nonlinear optimization problem. Thus, a satisfactory initial guess is critical. Before scan matching, we use a two-stage pose prediction method to obtain this initial guess. First, we use the extended Kalman filter (EKF) algorithm to fuse the wheel odometry and IMU data. The process uses these two types of data as observation information to update the state of the moment, as in [12].

Second, we use a multilocal-map-based scan matching method to further optimize the fusion result. The specific process is shown in Algorithm 2.

In the beginning, we perform a 2× downsampling on the local map to generate multiple local maps with resolutions ranging from high to low. Subsequently, we intend to find a LiDAR pose that maximizes the probabilities at the current LiDAR data in the lowest resolution local map. The initial pose is provided by the fusion result. Moreover, to ensure the matching accuracy, the pose obtained by matching against this local map is used as the initial value of the subsequent matching. This process is repeated until the matching against the highest resolution local map is realized, and the optimal initial guess is obtained.

After identifying the appropriate position, we insert the LiDAR data into the local map. This process updates the probability value of the corresponding grid. Each insertion of the LiDAR data is equivalent to adding an observation, and the result of the observation is saved using a hit set and miss set. According to the ray-tracing model, we use the projected LiDAR point as the hit point and save the grid point closest to this hit point in the hit set. Each grid point passing through the rays between the hit point and LiDAR data origin is saved in the miss set.

When the grid in the local map has never been observed previously, the probability is zero. When the grid is observed for the first time, it is assigned a probability value determined by its set (hit set or miss set). Each subsequent observation is based on the following formula to update the probability value of the grid:

Algorithm 2: Multilocal-map-based Scan Matching.

Input: current local map map_t, current scan S_t
Parameters: search window sizes S_x, S_y, S_θ, downsampling times num
Output: ekf predicted pose ξ_t^{ekf}, current predicted matching pose ξ_t^{mul}

initialization;
2 times downsampling the current local map map_t to form a set $\{map_t^1, map_t^2, ..., map_t^{num}\}$;
$count \leftarrow 0$;
$best\_score \leftarrow 0$;
while $count \le num$ **do**
    $r_{cur} \leftarrow$ resolution of $map_t^{num-count}$;
    $s_x \leftarrow \lceil S_x r_{cur} \rceil$;
    $s_y \leftarrow \lceil S_y r_{cur} \rceil$;
    $\varepsilon \leftarrow \arccos 1 - r_0^2 2 s_{max}^2$;
    $s_\theta \leftarrow \lceil S_\theta \varepsilon \rceil$;
    for $j_x \leftarrow -s_x$ to s_x **do**
        for $j_y \leftarrow -s_y$ to s_y **do**
            for $j_\theta \leftarrow -s_\theta$ to s_θ **do**
                $score \leftarrow_{k1}^{K} FT_{\xi_t^{ekf} r_{cur} j_x, r_{cur} j_y, r_{cur} j_\theta} h_k$;
                if $score > best\_score$ **then**
                    $\xi_t^{ekf} \leftarrow \xi_t^{ekf} r_{cur} j_x, r_{cur} j_y, r_{cur} j_\theta$;
                    $best\_score \leftarrow score$;
                end
            end
        end
    end
    $count \leftarrow count 1$;
end
$\xi_t^{mul} \leftarrow \xi_t^{ekf}$;

$$S \quad S^- \quad LogMeas \tag{13}$$

where S is the probability value of grid s after observation z, S^- is the probability value of grid s before observation, and $LogMeas$ represents the measurement model of the update process, which can be defined as

$$S \quad logOdds \mid z \tag{14}$$

$$S^- \quad logOdds \quad log\frac{ps \quad 1}{ps \quad 0} \tag{15}$$

$$LogMeas \quad log\frac{pz \mid s \quad 1}{pz \mid s \quad 0}, z \in \{0, 1\} \tag{16}$$

where the $logOdd$ function converts the product operation between the probability values into an addition operation, $ps \quad 1$ is the probability that grid s is occupied before the observation, and $ps \quad 0$ is the probability that grid s is free before the observation. According to the value of z, $LogMeas$ has two states. The specific value is determined by the sensor characteristics.

5.2. Backend pose graph optimization

The local map-based scan matching method can only decrease the short-term accumulated errors. However, the built local maps also accumulate errors over time, which can be optimized by building a global pose graph in the backend. In this process, we first use LiDAR frames that satisfy both rotation and translation conditions as key frames. Subsequently, we add all the keyframes and local maps to the pose graph as nodes to be optimized. Finally, the estimated trajectory is smoothed according to the constraints between the keyframe nodes and local map nodes. The optimization process of the pose graph is shown in Figure 4.

After a new loop constraint is constructed in the backend of the algorithm, we optimize the pose graph. We formulate the optimization process as a nonlinear least squares problem, in which the error term describes the error between the measured and estimated values. We consider the keyframe i and local map j as examples. The pose of keyframe i in the world frame is ξ_i^s, and the pose of local map j in the world frame is ξ_j^l. The error term can be expressed as

$$e_{ij} \quad z_{ij} - h\xi_i^s, \xi_j^l \tag{17}$$

where z_{ij} is the relative pose measured between keyframe i and local map j, calculated through loop-closure detection. $h\xi_i^s, \xi_j^l$ is the relative pose estimated between keyframe i and local map j, which represents the result of the local map-based scan matching.

The algorithm involves two types of constraints, namely, internal and loop constraints. The internal constraints are generated by keyframes and local maps that have subordination relationships. Specifically, the keyframes are inserted in the local map. In contrast, the loop constraints are generated by keyframes and other local maps, that is, the keyframes are associated with historical local maps. When more local maps are added to the pose graph, the time to identify the loop constraints gradually increases. Therefore, a DFS-based branch-and-bound algorithm is used to accelerate the search for loop constraints.

The process of loop-closure detection is similar to that of the DFS-based branch-and-bound algorithm used in global localization, except that the search range is changed from a global map to historical local maps. Hence, the search window no longer contains the prebuilt map but a partial area inside the local map. Because the frontend provides the current pose estimation ξ_{front} of the robot, we use the pose as the search origin to traverse the search space around it. The result ξ_{loop} is defined as

$$\xi_{loop} \quad \xi_{front} \quad r_0 dx, r_0 dy, \varepsilon d\varphi \tag{18}$$

If k represents the constraint between local map i and keyframe j, the error function can be expressed as

$$argmin_{k1}^{K} e_k^T \xi_k^s, \xi_k^l \Sigma_k^{-1} e_k \xi_k^s, \xi_k^l \tag{19}$$

where Σ_k^{-1} is the information matrix of the error term formed by keyframe i and local map j. The objective of optimizing the error function is to adjust ξ^s and ξ^l to minimize the trajectory errors formed by all nodes. Since no constraint relationship exists between each local map and keyframe in the pose graph, in solving the nonlinear optimization problem, considerable time is not required to calculate the Hessian matrix and only the pose increment needs to be solved via the Cholesky decomposition.
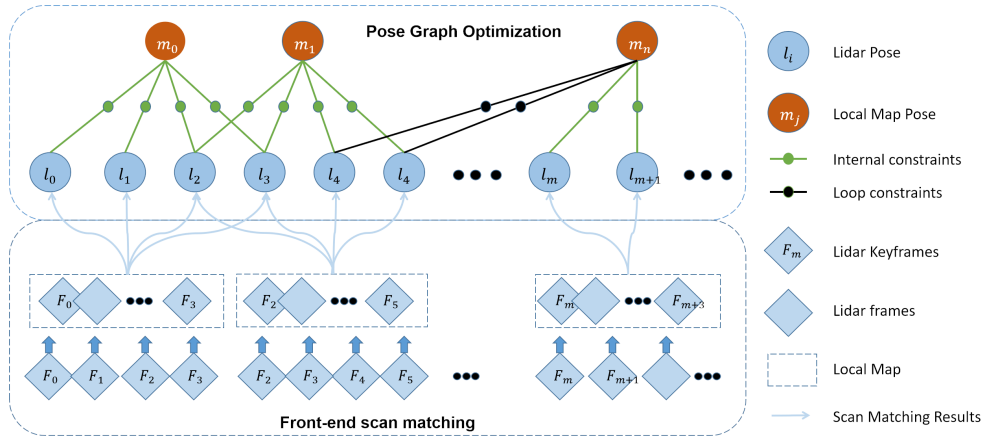
Figure 4: Schematic of the optimization of the backend pose graph.

6. Relocalization judgment

In numerous practical application scenarios, such as in warehouse logistics, robots are required to accomplish specific tasks within extensive workspaces. Due to the inability to form loop closures within short periods, robots tend to accumulate errors gradually. Furthermore, challenges arise when incorrect observational data leads to 'robot kidnapping', making it arduous to achieve localization recovery solely through position tracking algorithms.

In light of these challenges, we introduce an FSM (Finite State Machine)-based relocalization judgment algorithm. This algorithm initiates by acquiring the confidence level of the robot's current pose through the alignment of current LiDAR data with an inflated occupancy grid map. Subsequently, based on pre-set dual-threshold conditions, we assess the necessity to engage the global localization algorithm for timely localization recovery.

6.1. Confidence calculation and dual-threshold judgment

We use a method similar to the calculation of scores in scan matching to verify the pose ξ_{pt} obtained by the position tracking algorithm. In contrast to the point cloud registration algorithm that adopts the Euclidean distance to calculate the matching score between the two point clouds, we use the pose ξ_{pt} to project the current LiDAR data S onto the occupancy grid map and calculate the sum of the probability values of each LiDAR point s_i falling on the corresponding grid:

$$Score(\xi_{pt}) = \frac{1}{N} \sum_{i=1}^{N} M(T_{\xi_{pt}} s_i) \qquad (20)$$

where $T_{\xi_{pt}}$ converts the current LiDAR data S from the LiDAR frame to the map frame, and $M(\cdot)$ is used to calculate the probability value of each LiDAR point projected onto the occupancy grid map.

In this process, the occupancy grid map is converted from the prebuilt point cloud map. The resolution of this map is the same as that of the local map generated by the position tracking algorithm.

In practical applications, since there are relatively few valid points in the LiDAR frame, the measurement error of each valid point affects the confidence calculation results.

Considering this aspect, we use an inflated occupancy grid map instead of the original occupancy grid map to suppress the impact of LiDAR measurement errors.

In contrast to the cost map used to set the expansion areas to avoid robot collisions, we use the inflated occupancy grid map to reduce the error caused by noisy LiDAR measurements. When designing the inflated occupancy grid map, we first set the expansion radius r_{inf} according to the sensor range accuracy and extend it outward from the obstacle to obtain the expansion area according to r_{inf}. The grid probability in the expanded area is

$$P_{inf}(x, y) = e^{-k\delta d} \qquad (21)$$

where δd is the distance between grid x, y and the obstacle, and k is the scale factor. When k is large, the grid probability $P_{inf}(x, y)$ decreases rapidly. The probability of $P_{inf}(x, y)$ is limited to the range $[0, 1]$. The process of generating an inflated occupancy grid map is shown in Figure 5. We update the confidence calculation formula as follows:

$$Score(\xi_{pt}) = \frac{1}{N} \sum_{i=1}^{N} M^{InfMap}(T_{\xi_{pt}} s_i) \qquad (22)$$
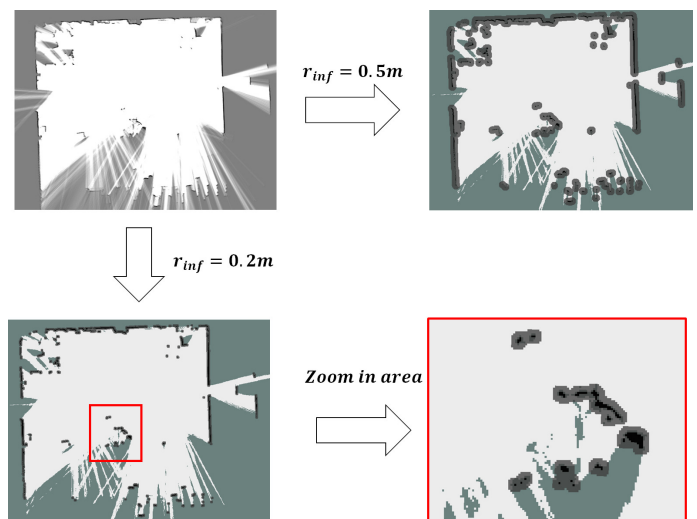

Figure 5: Process of generating an inflated occupancy grid map.

After calculating the confidence according to the above

formula, we use the dual-threshold judgment to evaluate the pose ξ_{pt}.

1. When the confidence is greater than the set threshold T_{h2}, the LiDAR data are projected inside the expansion area of the map, and the errors of the confidence calculation are generated by the noisy LiDAR measurements.

2. When the confidence is between the two thresholds T_{h1} and T_{h2} $T_{h2} > T_{h1}$, the accumulated errors exceed expectations, and the robot kidnapping problem does not occur. Therefore, we call the global localization algorithm to complete the search in the local area near the pose ξ_{pt} to correct the accumulated errors.

3. When the confidence is less than the set threshold T_{h1}, the robot kidnapping problem is considered to occur. We invoke the global localization algorithm to search the whole map. Specifically, the search window of the branch-and-bound algorithm covers the occupancy grid map to complete the localization recovery.

6.2. Relocalization judgment based on finite state machine

To monitor the localization state in real time, we use the idea of a finite state machine to model the relocalization judgment process. The mathematical model for a certain finite state machine can be defined as

$$M \quad Q, \Sigma, \delta, q_0, F \tag{23}$$

where Q is a nonempty set consisting of a finite number of states. According to the results of the position tracking algorithm, the states of the whole algorithm are divided into three categories: normal localization q_{norm}, large localization error q_{err}, and localization failure q_{kid}, which correspond to three cases of the dual-threshold judgment. Therefore, Q can be defined as

$$Q \quad q_{norm}, q_{err}, q_{kid} \tag{24}$$

where Σ represents the set of all inputs that can be accepted by each state, that is, the set of trigger conditions that cause the state transition. In this algorithm, we use the result of the dual-threshold judgment as the trigger condition. Additionally, we use e_{norm}, e_{err} and e_{kid} to represent the inputs of the algorithm in the transition between q_{norm}, q_{err} and q_{kid}. At this time, Σ is defined as

$$\Sigma \quad e_{norm}, e_{err}, e_{kid} \tag{25}$$

where $\delta : Q \times \Sigma \rightarrow Q$ represents the state transition function, which is mainly based on the current trigger condition e to complete the state transition of the algorithm from the current state q_{cur} to the second state q_{sec}:

$$q_{sec} \quad \delta q_{cur}, e \tag{26}$$

where q_0 is the initial state. F is the set of termination states, which is a subset of Q that represents that the algorithm is acceptable in this state (for instance, q_{norm}).

At the beginning of the algorithm operation, the robot is normally located. We first define the initial state q_0 as the

state q_{norm} and subsequently determine the trigger condition according to the result of the confidence calculation.

1. If the result of the confidence calculation is greater than T_{h2}, the condition e_{norm} is triggered. The algorithm maintains the state q_{norm} and outputs the result of the position tracking algorithm.

2. When the result of the confidence calculation is between T_{h1} and T_{h2} $T_{h2} > T_{h1}$, the condition e_{err} is triggered. The algorithm executes the function $\delta q_{norm}, e_{err}$ to achieve the transition from q_{norm} to q_{err}, that is, the global localization algorithm is called to perform a search in the local range.

3. When the result of the confidence calculation is less than T_{h1}, the condition e_{kid} is triggered. The algorithm executes the function $\delta q_{norm}, e_{kid}$ for the transition between the two states of q_{norm} to q_{kid}. Specifically, the global localization algorithm is invoked to perform a search on the global map.

The state transition relationship in the finite state machine is shown in Figure 6. The specific steps of the FSM-based relocalization judgment algorithm are shown in Algorithm 3.
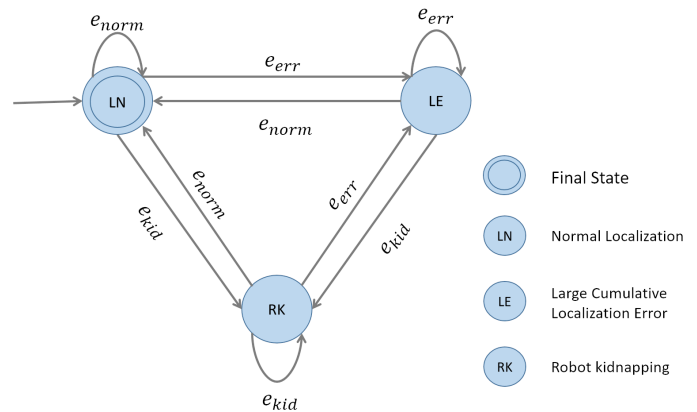

Figure 6: State transition relationship in the finite state machine.

This algorithm is expected to solve the problem of robot kidnapping. Hence, it is necessary to search for the best matches on the global map. To ensure the stability of the algorithm, we limit the number of calls to the global localization algorithm to manage the errors in the confidence calculation caused by environmental changes (such as dynamic environments). Our confidence calculation method averages the matching probabilities of each LiDAR point participating in the scan matching. The method exhibits a certain degree of robustness in scenarios involving slight environmental changes; however, its performance is limited in cases involving severe environmental changes. Thus, it is preferable to limit the number of calls to global localization. When the set maximum number of times is reached, the relocalization judgment algorithm is automatically terminated.

7. Experiments

As described in this section, we validate the robustness and accuracy of our algorithm through extensive experiments. First, we present the implementation details, including the experimental environment and preparation steps. Second, we describe the evaluation of our algorithm in a simulated laboratory environment and analysis of the performance of different parts. Finally, we assess the performance of our algorithm in an actual workshop environment.

Algorithm 3: Relocalization judgment based on finite state machine.

Input: current period t, current scan S_t, inflated occupancy grid map m, position tracking pose ξ_{pt}

Parameters: confidence thresholds T_{h1}, T_{h2}, Number of relocalization N_{rel}

Output: optimal robot pose ξ_t^*

initialization;
$score \leftarrow 0$;
$StatusFlag \leftarrow false$;
$count \leftarrow 0$;
while $StatusFlag\ false$ **do**
  $score \leftarrow Score\xi_{pt}$;
  if $score < T_{h2}$ **then**
    if $T_{h1} \leq score \leq T_{h2}$ **then**
      $\xi_t^* \leftarrow GlobalLocalization\xi_{pt}, S_t$;
      $count \leftarrow count\ 1$;
    end
    else
      $\xi_t^* \leftarrow GlobalLocalizationS_t$;
      $count \leftarrow count\ 1$;
    end
  end
  else
    $\xi_t^* \leftarrow \xi_{pt}$;
    $count \leftarrow 0$;
  end
  if $count \geq N_{rel}$ **then**
    $StatusFlag \leftarrow true$;
  end
end

---

7.1. Implementation Details

Using the Gazebo physical simulation platform, we build a virtual laboratory environment that mimics the layout and dimensions of the real-world laboratory. In such a typical structured environment, we use a simulated jackal robot with basic sensors (e.g., 2D LiDAR, IMU, and wheel encoders) to perform the experiments. To perform the assessment in an actual workshop environment, we use the IR300 commercial logistics robot to conduct the experiments. The environments are shown in Figure 7(a) and Figure 7(b).

In the preparation stage, we use an open-source 2D LiDAR SLAM algorithm to build a point cloud map of the environment. The process can be divided into three stages:

1. Data preprocessing: Raw sensor data for time synchro-

nization are collected to alleviate the errors caused by the difference in the working frequency of different sensors;

2. Mapping: The handle is used to ensure that the robot can traverse the complete environment to build a point cloud map in real time;

3. Postprocessing: The built point cloud map is filtered to eliminate anomalies and outliers.
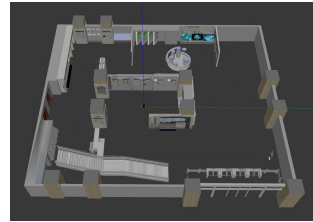
(a) Simulated laboratory environment with dimensions of 20 m×20 m.

(b) Actual workshop environment with dimensions of 30 m×60 m

Figure 7: Experiment environment.

7.2. Localization experiment in the simulated laboratory environment

We first test the global localization in the simulated laboratory environment. The size of the laboratory is approximately 20 m×20 m; thus, we set the linear search window sizes in the x- and y-directions as 30 m, respectively, and the angular search window size is set as 2π. The depth of the search tree in the branch-and-bound algorithm is 7. Correspondingly, there exist seven built occupancy grid maps, in which the highest resolution of the occupancy grid map is r_0 0.4 m. To ensure that the iterative nearest point algorithm can achieve the highest accuracy, we set the maximum number of iterations as 100 and maximum tolerance of two consecutive iterations as 10^{-13}.

In the experiment, we select six positions on the map to test the performance of the algorithm. To uniformly cover the free space of the environment, the selected adjacent positions are separated by Δd 5 m, and the orientations of each position are uniformly distributed in $-\pi, \pi$, as shown in Figure 8(a). When the robot starts operating, it automatically implements the global localization algorithm to obtain the robot's initial pose based on the current LiDAR data, as shown in Figure 8(b) and Figure 8(c).

e_x and e_y denote the position error between the real position and estimated position of the robot, and e_φ represents the difference between the real and estimated orientations. In addition to these standard criteria, we consider the runtime and success rate of the algorithm. The runtime refers to the time from the beginning of the algorithm to the time at which the final result is obtained. The success rate describes the probability of successful localization at the specified position. When the error between the real position and estimated position of the robot is less than 0.05 m and the orientation error is less than $2°$, the localization is considered successful. We perform 20 experiments for each specified position.

(a) Positions selected on the map for the global localization experiment

(b) Before global localization at #3
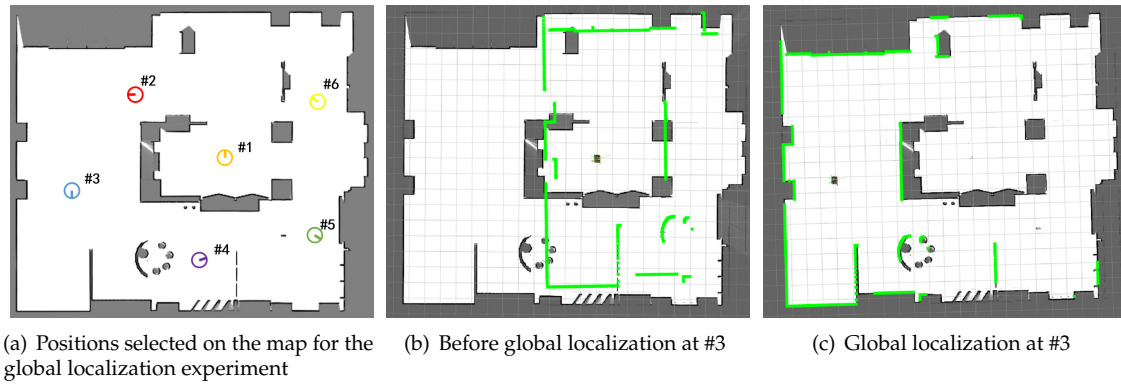
(c) Global localization at #3

Figure 8: Evaluation of the global localization algorithm in the simulated laboratory environment.

In the test, we verify the performance of the proposed algorithm. Hence, a comparison experiment is not conducted for the following reasons:

1. The localization result is compared with the real position of the robot;

2. Few open-source algorithms can achieve global localization. Actual results for the few algorithms that can accomplish this function have been extensively reported. Therefore, the details do not need to be presented.

According to Table 1, the average orientation error is less than 0.2°, the average position errors in the x- and y-directions are less than 0.03 m and 0.01 m, respectively. As described in Section 4, the search accuracy of the branch-and-bound algorithm is limited by the highest resolution of the occupancy grid map (0.4 m). However, the two-stage matching algorithm achieves a localization accuracy that is higher than that of algorithms that use an occupancy grid map with a resolution of 0.05 m for scan matching. Moreover, we achieve a 100% localization success rate in each position.

The runtime varies considerably across positions (Figure 9). According to the runtime of each stage in the global localization algorithm, the most notable time consumption pertains to the determination of the initial pose by the branch-and-bound algorithm. In contrast, the runtime of the iterative closest point algorithm is stable and occupies only a small proportion. Although the runtime does not meet the requirements of real-time localization, considering the actual size of the map used in the search process, our algorithm can promptly find the global pose of the robot and dramatically decrease the time associated with redundant calculations.

In the algorithm, when the depth (d 7) is constant, the resolution r_0 of map_0 used in the branch-and-bound algorithm directly influences the localization accuracy and runtime. We analyze the impact of the different resolutions r_0 on the algorithm at position 4 $-6.33, 1.23, -45°$. The results are shown in Table 2. When r_0 is small, although the solution obtained by the branch-and-bound algorithm is closer to the optimal solution, the search time is large. In contrast, the proposed algorithm achieves a reasonable balance between the efficiency and localization accuracy. The localization result obtained by the proposed algorithm

does not considerably fluctuate with the change in r_0, and the runtime is exponentially decreased.
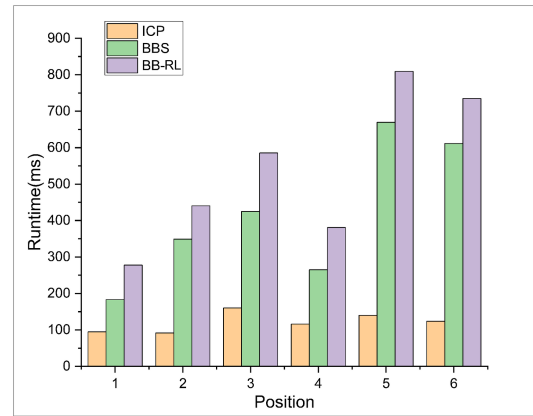

Figure 9: Runtime distribution for specific positions (BBS: branch-and-bound algorithm, ICP: iterative closest point algorithm, BB-RL: proposed algorithm).

To assess the accuracy of our algorithm, we conducted 50 experimental runs in the simulation environment, and for each run, we randomly selected a position on the map to measure the error. The results are shown in Figure 10. The average position errors in the x- and y-directions are 0.02037 m and 0.00648 m, respectively. The average orientation error is 0.00129 rad, and the average runtime is 576.35 ms. Additionally, the maximum position error in the x- and y-directions are 0.0317 m and 0.0185 m, respectively. The maximum orientation error is 0.00353 rad, and the maximum runtime is 1027.67 ms.

Next, we conduct the position tracking experiment. We assume that the robot's initial pose is known (automatically obtained by Gazebo). In the test, the robot moves in a circle around the indoor environment. The starting and ending points coincide. We evaluate the error of the robot between the starting and ending points. The process is shown in Figure 11. As a reference, we compare the AMCL and Cartographer frameworks to verify the accuracy of the algorithm.

In the parameter settings, the number of local maps for multi-local-map-based scan matching was established as 3. For loop-closure detection, the linear search window size was set at 20 m and the angular search window size for loop detection at 2π radians. Additionally, the search depth was defined as 7.

The trajectory of each algorithm is shown in Figure 12.

Table 1: Global localization results for specific positions in the simulated laboratory environment.
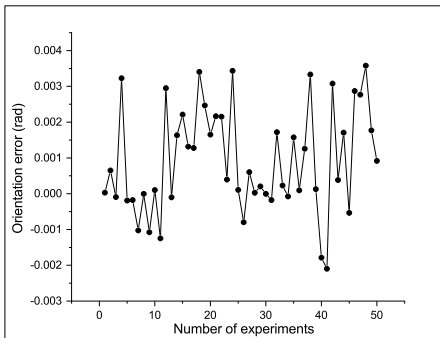
Position	$e_x m$	$e_y m$	$e_\varphi rad$	Runtimems	Success Rate%
#1	0.0249	-0.00631	0.000119	277.806	100
#2	0.0130	-0.00529	0.00123	440.500	100
#3	0.0191	-0.00455	0.000581	585.314	100
#4	0.0236	-0.00971	0.00267	380.872	100
#5	0.0246	-0.00933	0.000609	809.102	100
#6	0.0180	-0.00303	0.000237	734.903	100
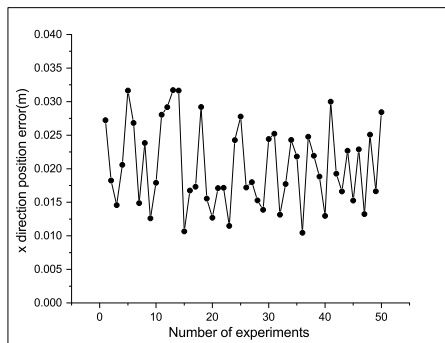
(a) Position error in the x-direction
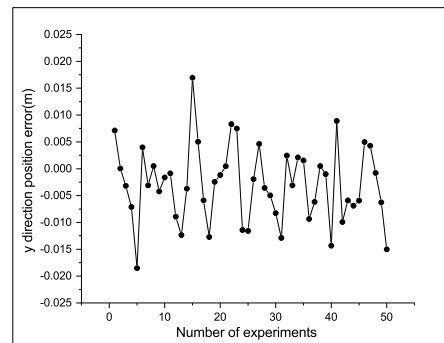
(b) Position error in the y-direction

(c) Orientation error
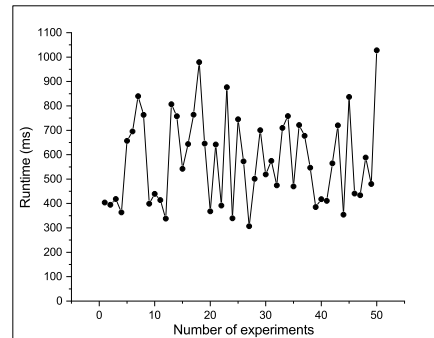
(d) Runtime

Figure 10: Experimental results of 50 positions randomly selected for global localization in the simulated laboratory environment.

(a) Operation of the robot in the simulated laboratory environment
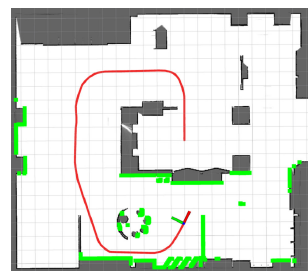
(b) Real-time trajectory of the robot shown on the map

Figure 11: Evaluation of the position tracking algorithm in the simulated laboratory environment.

Table 2: Experimental results of global localization algorithm at position 4 with different resolutions r_0.

r_0		$e_x m$	$e_y m$	$e_\varphi rad$	Runtime ms
0.5m	BB-RL	0.02319	0.00626	0.00426	329.356
	BBS	0.33	0.27	0.03045	262.846
0.4m	BB-RL	0.02236	0.00546	0.00271	411.043
	BBS	0.07	0.03	0.01378	295.019
0.3m	BB-RL	0.02332	0.00480	0.00609	647.166
	BBS	0.03	0.03	-0.03621	531.401
0.2m	BB-RL	0.02331	0.00633	0.00209	1069.53
	BBS	0.07	0.03	0.00163	1016.26
0.1m	BB-RL	0.02019	0.00332	0.00584	6069.81
	BBS	0.03	0.03	-0.00288	5980.87
0.05m	BB-RL	0.02148	0.00370	0.00198	31851
	BBS	0.02	0.02	0.00211	31808.9

Results obtained using AMCL, Cartographer, and the proposed algorithm are relatively close to the ground truth because the sensor data obtained in the simulation environment are ideal, and no sensor failures or other emergencies occur. However, according to the analysis of trajectory details, the proposed algorithm fits the ground truth more closely. According to the trajectory error comparison shown in Table 3, the proposed algorithm outperforms the compared algorithms in terms of the accuracy. The Figure 13 shows the time-based error of the position on both the x-axis and y-axis, as well as the orientation error during the position tracking experiment.

Figure 12: Comparison of trajectories of different position tracking algorithms in a simulated laboratory environment.

Finally, the relocalization experiment is conducted. Since the correction of the accumulated errors is reflected in the experimental results of the position tracking, we test only the localization recovery ability of the algorithm in the case of robot kidnapping. First, we initialize the robot and control it to move in the environment. Second, we suddenly move the robot to positions A, B, C, and D (Figure 14) to artificially create a robot kidnapping situation to verify the effectiveness of the relocalization. Due to only a few existing open-source algorithms can solve the robot kidnapping problem. Additionally, no uniform standard for the experimental procedure exists. Hence, we do not conduct a comparison experiment in this test.

Table 3: Comparison of the position tracking error in the simulated laboratory environment.

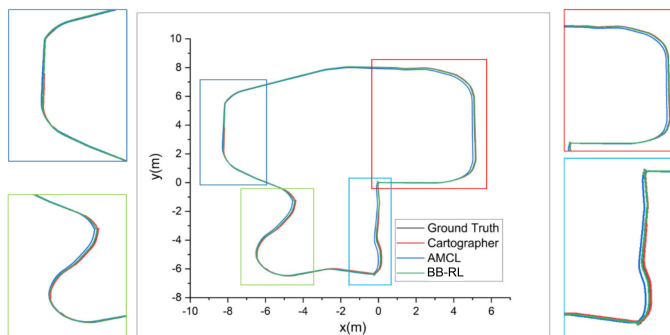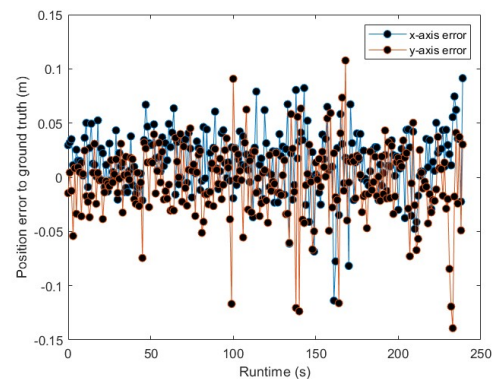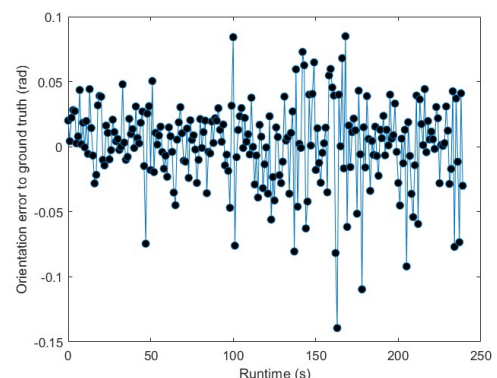|	$e_x m$	$e_y m$	$e_\varphi rad$
BB-RL	**0.01398**	**-0.00176**	**0.00108**
AMCL	-0.06515	-0.070497	-0.0278
Cartographer	-0.05141	0.043688	0.00232

(a) Position error in the x-direction and y-direction

(b) Orientation error in the y-direction

Figure 13: Time-based error analysis of the BB-RL position tracking algorithm compared to ground truth data.

Before the test, to ensure that the map has the same resolution as that of the local map used in the position tracking

algorithm, we convert the prebuilt point cloud map into an occupancy grid map with a resolution of 0.05 m. According to the range accuracy of the LiDAR, the expansion radius r_{inf} is set as 0.1 m, the scale factor is set as 1, and the thresholds T_{h1} and T_{h2} are set as 0.5 and 0.8. The experimental results are shown in Figure 15.
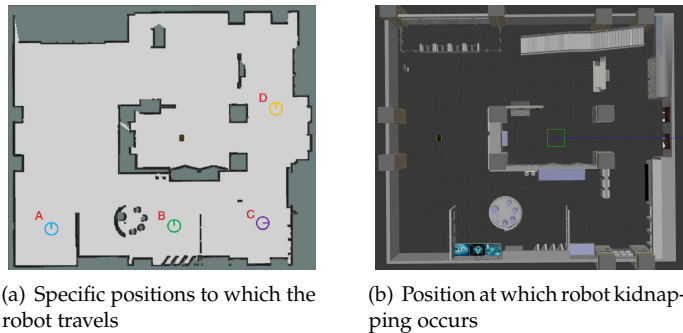

(a) Specific positions to which the robot travels

(b) Position at which robot kidnapping occurs

Figure 14: Process of relocalization experiment in the simulated laboratory environment.

(a) Relocalization at #A

(b) Relocalization at #B

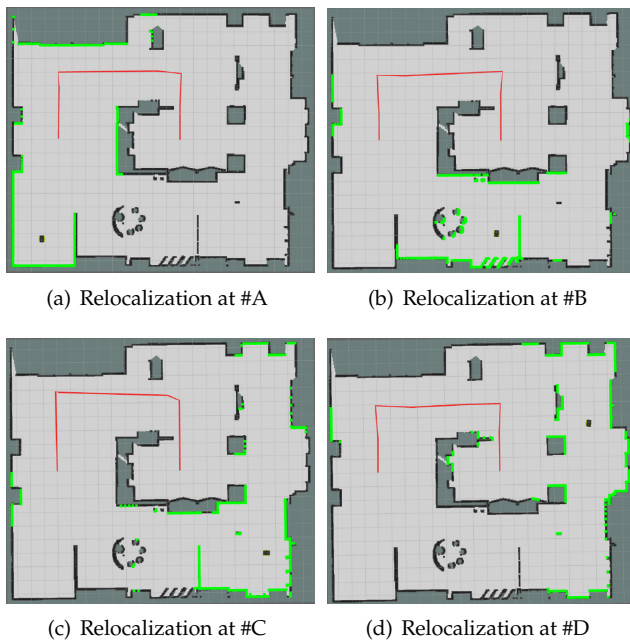(c) Relocalization at #C

(d) Relocalization at #D

Figure 15: Relocalization results for positions A, B, C, and D following a robot-kidnapping.

The quantitative results are shown in Table 4. Among these results, the average position errors in the x- and y-directions are less than 0.03 m and 0.01 m, respectively, the orientation error is less than 0.1°, the runtime is within 600 ms, and the success rate at each position is consistent with global localization, remaining at 100%. From the overall perspective, the relocalization results are similar to those of the global localization in the simulation environment. When the relocalization judge algorithm is used to identify if the robot is kidnapped, localization recovery can be effectively realized by calling the global localization algorithm.

7.3. Localization experiment in the actual workshop environment

A global localization experiment is conducted in the actual workshop environment. In this experiment, the parameters

of the branch-and-bound algorithm are changed. Because the size of the workshop is approximately 60 m ×30 m, we set the linear search window sizes in the x- and y-directions as 70 m and 40 m, respectively. All other parameter settings are the same as those in the global localization experiment in the simulated laboratory environment.

Similarly, we select six positions on the map to analyze the performance of the algorithm. Each adjacent position is separated by Δd 15 m, and the orientation of each position is uniformly distributed in $-\pi, \pi$. The selected positions are shown in Figure 16. The localization process of position 3 is shown in Figure 17 and Figure 18. The evaluation criteria and number of experiments are the same as those in the global localization experiment in the simulated laboratory environment.

Figure 16: Positions selected on the map for the global localization experiment.
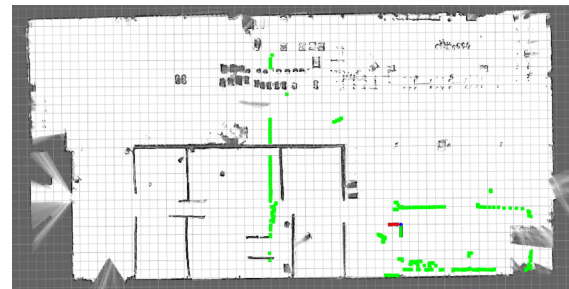
Figure 17: Robot-kidnapping on position #3.
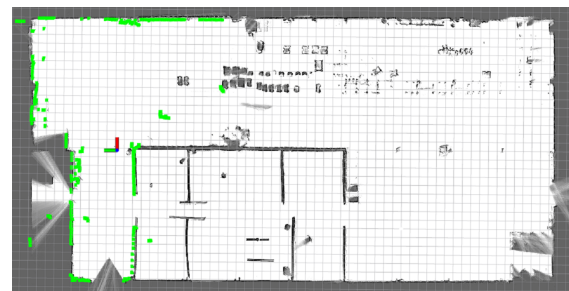
Figure 18: Global localization on position #3.

According to Table 5, the average position errors in the x- and y-directions are less than 0.032 m and 0.02 m, respectively, and the average orientation error is less than 1.2°. Compared with the experimental results of global localization in the simulated laboratory environment, the error of global localization in the workshop environment is significantly larger. The sensor noise and interference of the dynamic environment in the actual environment are more

Table 4: Relocalization results for specific positions in the simulated laboratory environment.

Position	$e_x m$	$e_y m$	$e_\varphi rad$	Runtime ms	Succuess Rate%
A	0.02448	0.000870	-0.000313	401.946	100
B	0.02017	-0.00485	0.000605	376.736	100
C	0.02452	0.00723	-0.00116	538.637	100
D	0.02205	0.00374	0.00114	329.169	100

Table 5: Global localization results for specific positions in the actual workshop environment.

Position	$e_x m$	$e_y m$	$e_\varphi rad$	Runtime ms	Succuess Rate%
#1	0.02261	-0.00402	0.00711	459.686	100
#2	0.02289	-0.00326	0.00884	605.213	100
#3	0.02382	0.01919	0.01673	633.351	95
#4	0.03064	0.01212	0.01193	1260.876	90
#5	0.02819	0.00895	0.00416	833.633	95
#6	0.02775	-0.01226	0.01938	671.117	95

unpredictable than those in the simulation environment and directly affect the localization accuracy.

The success rate is slightly decreased at positions 3-6 because the current LiDAR data tend to produce mismatches with the occupancy grid map. The runtime associated with each stage in the global localization algorithm (Figure 19) shows that the overall runtime at each position increases. Especially, at position 4, the overall running time is 1260.87 ms, 1226.81 ms of which correspond to the branch-and-bound algorithm. This finding demonstrates that most of the time consumed by the global localization algorithm pertains to the branch-and-bound algorithm implementation.
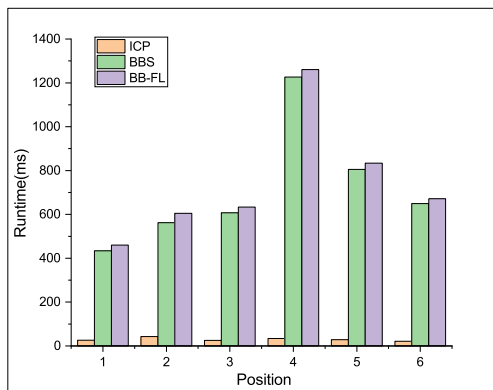

Figure 19: Runtime distribution for specific positions.

Moreover, in this experiment, we test the impact of different resolutions r_0 of map_0 used in the branch-and-bound algorithm on the localization accuracy and runtime when the depth (d 7) remains unchanged. The experimental results at position 1 $-0.43, -0.365, 0°$ are shown in Table 6. Compared with the results of the simulated laboratory environment, the runtime at different resolutions r_0 is higher due to the increased size of map_0. However, the proposed algorithm exhibits similar localization accuracies at different resolutions r_0. Therefore, we can choose r_0 0.4 m to balance localization efficiency and accuracy.

Table 6: Experimental results of global localization algorithm at position 1 with different resolutions r_0.

r_0		$e_x m$	$e_y m$	$e_\varphi rad$	Runtime ms
$0.5m$	BB-RL	0.02313	-0.00623	0.00505	398.397
	BBS	-0.145	0.31	0.0333	369.458
$0.4m$	BB-RL	0.02281	-0.00172	0.00545	532.387
	BBS	-0.145	0.11	0.0133	507.262
$0.3m$	BB-RL	0.02273	-0.00901	0.00462	934.256
	BBS	-0.145	-0.09	0.03	910.888
$0.2m$	BB-RL	0.02205	-0.01520	0.00489	1878.96
	BBS	0.055	-0.09	0.00667	1864.33
$0.1m$	BB-RL	0.01898	-0.01287	0.00465	14806.3
	BBS	0.055	0.01	0.0133	14796.1
$0.05m$	BB-RL	0.02157	-0.00126	0.00537	296631
	BBS	0.005	0.01	0.01167	296612

To assess the accuracy of the global localization algorithm, we conducted 50 experiments in a real-world environment. For each experiment, we randomly selected a position on the map to evaluate the error. The results are shown in Figure 20. The average position errors in the x- and y-directions are 0.02516 m and 0.0079 m, respectively. The average orientation error is 0.0089 rad, and the average runtime is 734.18 ms. Additionally, the maximum position errors in the x- and y-directions are 0.03675 m and 0.02669 m, respectively. The maximum orientation error is 0.0193 rad, and the maximum runtime is 1407.48 ms. Compared with the results in the simulated laboratory environment, the position error and runtime are higher, although the actual engineering needs can still be satisfied.

Next, we perform the position tracking experiment. First, we assume that the robot's initial pose is the origin of the map in this experiment. Subsequently, we control the robot to move in a circular path in the workshop to return to the starting point. Finally, the error between the starting point and ending point is calculated as the accuracy criterion. As a reference, we compare the results of EKF fused with IMU and wheel odometry, AMCL, and Cartographer to verify the accuracy of the algorithm. The experiment is shown in Figure 21 and Figure 22 .

(a) Position error in the x-direction

(b) Position error in the y-direction

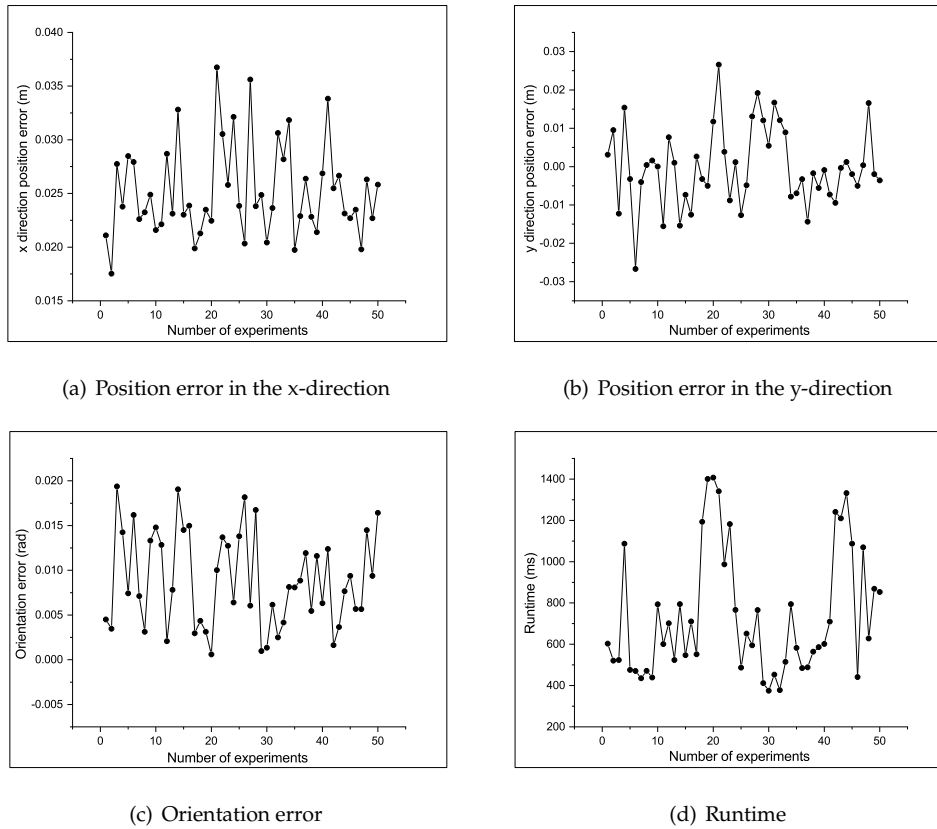
(c) Orientation error

(d) Runtime

Figure 20: Experimental results of 50 positions randomly selected for global localization in the actual workshop environment.

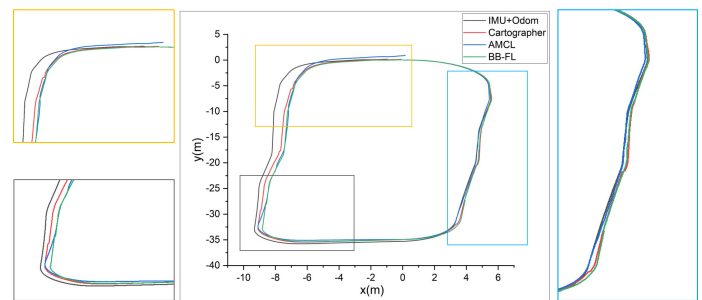Figure 21: Operation of the robot in the actual workshop environment

Figure 23: Comparison of trajectories of different position tracking algorithms in an actual workshop environment.

According to Table 7, the position error in the x-direction of EKF fusion is approximately 1 m, the position error in the y-direction of AMCL is approximately 0.9 m, and the orientation error of AMCL exceeds 4.5°. In contrast, the proposed algorithm achieves satisfactory results in all aspects: the position errors in the x- and y-directions are both less than 0.05 m, and the orientation error is less than 1°.

Table 7: Comparison of position tracking errors in the actual workshop environment.

	$e_x m$	$e_y m$	$e_\varphi rad$
BB-RL	**-0.03780**	**0.04696**	0.01111
AMCL	0.16055	0.87677	0.08407
Cartographer	-0.08248	0.12581	**0.01017**
IMUOdom	-0.96486	0.16832	0.05129

Figure 22: Real-time trajectory of the robot shown on the map in the actual workshop environment.

All the parameter settings are the same as those in the position tracking experiment in the simulated laboratory environment. The trajectory of each algorithm is shown in Figure 23. Notably, (1) the trajectory error associated with the EKF fusion is the largest; (2) there exists a certain deviation in the local details between each trajectory; and (3) the trajectory of the AMCL near the starting point is not closed.

Finally, a relocalization experiment is conducted in the

(a) Specific positions to which the robot travels (b) Position at which robot kidnapping occurs (c) Relocalization at #A

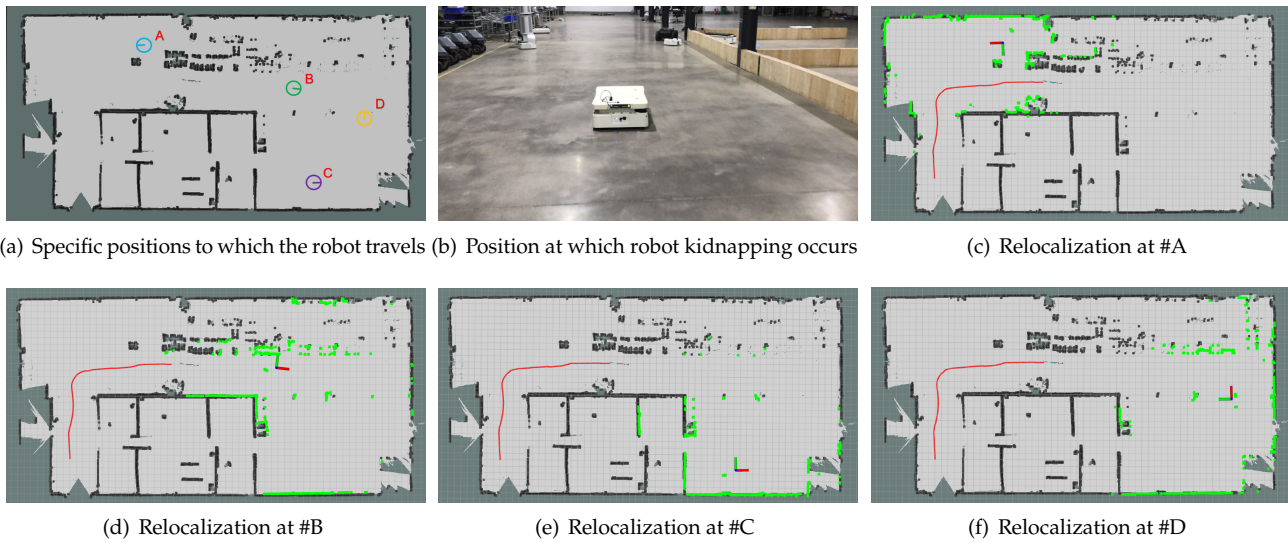(d) Relocalization at #B (e) Relocalization at #C (f) Relocalization at #D

Figure 24: Relocalization results for positions A, B, C, and D (the red line represents the trajectory of the robot before robot kidnapping occurs, the measurement data of the LiDAR are represented by the green line, and the position of the robot is represented by the orthogonal coordinate axes)

Table 8: Relocalization results for specific positions in the actual workshop environment.

Position	$e_x m$	$e_y m$	$e_\varphi rad$	Runtimems	Succuess Rate%
A	0.02819	0.00895	0.00416	904.561	95
B	0.02686	-0.00881	0.00632	630.238	95
C	0.02246	-0.00195	0.00937	374.754	100
D	0.02302	-0.00736	0.00207	434.718	100

actual workshop environment. The same experimental method as that of the relocalization experiment in the simulated laboratory environment is followed: First, the robot is controlled to move in the workshop through the handle. Second, a robot kidnapping situation is created by artificially moving the robot to positions A, B, C, and D (Figure 24(a) and Figure 24(b)). Finally, the position error and orientation error of different positions are calculated. In terms of the parameter settings, the thresholds T_{h1} and T_{h2} are set as 0.5 and 0.75, respectively. The resolution of the inflated occupancy grid map is 0.05 m, the expansion radius r_{inf} is set as 0.2 m, and the scale factor k is set as 1. The experimental results are shown in Figure 24(c), Figure 24(d), Figure 24(e) and Figure 24(f).

According to Table 8, the error in the actual workshop environment is higher than that in the simulated laboratory environment. At position A, the position error in the x-direction exceeds 0.028 m, the orientation error exceeds 0.2°, and the runtime is close to 1 s. Additionally, the runtime at positions C and D is significantly decreased with values of only 374.754 ms and 434.718 ms, respectively. For the success rate, relocalization failures occur at positions A and B. However, overall, the success rate is maintained at each selected position.

Building on the introduction of the Branch-and-Bound for Robust Localization (BB-RL) algorithm, the experimental findings can be effectively summarized. The BB-RL algorithm offers a potent solution for indoor robot localization by harmoniously integrating position tracking, global local-

ization, and the resolution of the kidnapped robot dilemma within a cohesive framework. The evaluation shows that BB-RL achieves a balance among speed, accuracy, and robustness, establishing it as an effective and practical choice for indoor robot localization scenarios.

In summary, the proposed trajectory aligns more closely with the ground truth compared to those generated by other compared algorithms. The BB-RL algorithm surpasses competing algorithms in accuracy. Regarding the kidnapping problem, robots equipped with BB-RL successfully overcome localization failures, maintaining a commendable success rate. The effectiveness of the BB-RL algorithm in solving the three core localization challenges has been confirmed in real-world settings, achieving sustained accuracy and an appropriate execution frequency. This underscores the algorithm's viability and efficiency in practical applications, particularly in navigating and localizing within indoor environments.

8. Conclusion and Future Work

A robust and accurate localization is crucial for effective path planning, precise motion control, and reliable obstacle avoidance in the field of autonomous robotics. Recognizing the need for accurate and robust localization in real-world applications, this paper presents a BB-RL (Branch-and-Bound for Robust Localization) algorithm for indoor mobile robots. Its novelty lies in the comprehensive and integrated approach to addressing the three key localization tasks: global

localization, position tracking, and the kidnapped robot problem.

The approach begins with a two-stage global localization algorithm to determine the robot's initial pose. A DFS-based branch-and-bound algorithm ensures the search solution is globally optimal. To achieve localization precision beyond grid resolution, the iterative closest point (ICP) algorithm refines this solution locally.

For continuous position tracking, a local map-based scan matching technique is used. To achieve reliable results, a two-tier prediction method combining an Extended Kalman Filter (EKF) with multi-local map-based scan matching is proposed, ensuring initial guesses converge to the global optimum. Additionally, a global pose graph is constructed to minimize accumulated errors across local maps, while a DFS-based branch-and-bound algorithm accelerates loop-closure detection.

Long-term stability of the algorithm is maintained through an innovative Finite State Machine (FSM)-based relocalization judgment method, which uses an inflated occupancy grid map to reduce LiDAR measurement noise effects on confidence calculations. A dual-threshold judgment strategy accurately identifies the robot's localization state, triggering the global localization algorithm as needed for timely localization recovery.

In conclusion, our algorithm shows out for its robustness, scalability, and practicality, underscored by its fast processing capabilities. Extensively tested in both simulated laboratory environments and real-world workshops, it has also been successfully implemented on a commercial logistics robot platform. This deployment demonstrates not only its high localization accuracy but also its robust and rapid performance in diverse operational contexts.

Finally, we have underscored the advantages of our localization framework, especially in indoor environments prone to localization difficulties, such as logistics warehouses and factory inspections. These environments require a robust and accurate localization algorithm. By integrating existing sensor data with advanced algorithms, our framework significantly improves localization accuracy and robustness in these complex scenarios.

In the future, our research will focus on utilizing a broader array of features for robot localization, including the features from 3D point cloud maps and camera sensors. These data types promise to enhance localization accuracy by providing a richer set of environmental information. However, incorporating these algorithms and features is expected to increase computational demands. A key direction for our future work will be to find a balance between integrating these diverse and multi-dimensional features and maintaining efficient processing speeds. We aim to integrate 3D point cloud features for improved relocalization without compromising computational efficiency.

Another aspect of our future work will address the challenges posed by complex, dynamic environments, such as scenarios where robots are surrounded by crowds. Identifying the cause of localization failures—whether due to actual kidnapping scenarios or temporary disruptions caused by dynamic environmental factors—and deciding whether to initiate relocalization presents a challenge we plan to address. This involves differentiating between true kidnapping situations and temporary conditions caused by dynamic environments, thereby guiding the decision on whether relocalization is necessary.

This comprehensive approach, leveraging a variety of data sources and technologies, is designed to ensure that localization challenges, even in the most demanding environments, can be effectively addressed. Our goal is to provide a more comprehensive and reliable solution for indoor robot localization, overcoming current limitations and preparing for future challenges.

Conflict of Interest The authors declare no conflict of interest.

References

[1] DeSouza, Guilherme N and Kak, Avinash C, "Vision for mobile robot navigation: A survey", *IEEE transactions on pattern analysis and machine intelligence*, vol. 24, no. 2, pp. 237–267, 2002.

[2] Georgiev, Atanas and Allen, Peter K, "Localization methods for a mobile robot in urban environments", *IEEE Transactions on Robotics*, vol. 20, no. 5, pp. 851–864, 2004.

[3] Alatise, Mary B and Hancke, Gerhard P, "A review on challenges of autonomous mobile robot and sensor fusion methods", *IEEE Access*, vol. 8, pp. 39830–39846, 2020.

[4] Altan, Aytaç and Bayraktar, Köksal and Hacıoğlu, Rıfat, "Simultaneous localization and mapping of mines with unmanned aerial vehicle", *2016 24th Signal Processing and Communication Application Conference (SIU)*, pp. 1433–1436, 2016, doi:10.1109/SIU.2016.7496019.

[5] Aytaç Altan and Rıfat Hacıoğlu, "Model predictive control of three-axis gimbal system mounted on uav for real-time target tracking under external disturbances", *Mechanical Systems and Signal Processing*, vol. 138, p. 106548, 2020, doi:https://doi.org/10.1016/j.ymssp.2019.106548.

[6] Cox, Ingemar Johansson and Wilfong, Gordon Thomas, *Autonomous robot vehicles*, Springer, Schweiz, 1990.

[7] Thrun, Sebastian and Beetz, Michael and Bennewitz, Maren and Burgard, Wolfram and Cremers, Armin B and Dellaert, Frank and Fox, Dieter and Haehnel, Dirk and Rosenberg, Chuck and Roy, Nicholas and others, "Probabilistic algorithms and the interactive museum tour-guide robot minerva", *The international journal of robotics research*, vol. 19, no. 11, pp. 972–999, 2000.

[8] Alqahtani, Ebtesam J and Alshamrani, Fatimah H and Syed, Hajra F and Alhaidari, Fahd A, "Survey on algorithms and techniques for indoor navigation systems.", *2018 21st Saudi Computer Society National Computer Conference (NCC)*, pp. 1–9, 2018, doi: 10.1109/NCG.2018.8593096.

[9] Zafari, Faheem and Gkelias, Athanasios and Leung, Kin K, "A survey of indoor localization systems and technologies", *IEEE Communications Surveys & Tutorials*, vol. 21, no. 3, pp. 2568–2599, 2019, doi:10.1109/COMST.2019.2911558.

[10] Liu, Wenxin and Caruso, David and Ilg, Eddy and Dong, Jing and Mourikis, Anastasios I and Daniilidis, Kostas and Kumar, Vijay and Engel, Jakob, "Tlio: Tight learned inertial odometry", *IEEE Robotics and Automation Letters*, vol. 5, no. 4, pp. 5653–5660, 2020, doi:10.1109/LRA.2020.3007421.

[11] Brossard, Martin and Bonnabel, Silvere, "Learning wheel odometry and imu errors for localization", *2019 International Conference on Robotics and Automation (ICRA)*, pp. 291–297, 2019, doi: 10.1109/ICRA.2019.8794237.

[12] Moore, Thomas and Stouch, Daniel, "Intelligent autonomous systems 13", pp. 335–348, Springer, Padua, 2016, doi:10.1007/978-3-319-08338-4_25.

[13] He, Chengyang and Tang, Chao and Yu, Chengpu, "A federated derivative cubature kalman filter for imu-uwb indoor positioning", *Sensors*, vol. 20, no. 12, p. 3514, 2020, doi:10.3390/s20123514.

[14] Liu, Fei and Li, Xin and Wang, Jian and Zhang, Jixian, "An adaptive uwb/mems-imu complementary kalman filter for indoor location in nlos environment", *Remote Sensing*, vol. 11, no. 22, p. 2628, 2019, doi:10.3390/rs11222628.

[15] Cui, Jishi and Li, Bin and Yang, Lyuxiao and Wu, Nan, "Multi-source data fusion method for indoor localization system", *2020 IEEE/CIC International Conference on Communications in China (ICCC)*, pp. 29–33, 2020, doi:10.1109/ICCC49849.2020.9238826.

[16] Yang, Xiaofei and Wang, Jun and Song, Dapeng and Feng, Beizhen and Ye, Hui, "A novel nlos error compensation method based imu for uwb indoor positioning system", *IEEE Sensors Journal*, vol. 21, no. 9, pp. 11203–11212, 2021, doi:10.1109/JSEN.2021.3061468.

[17] Davison, Andrew J and Reid, Ian D and Molton, Nicholas D and Stasse, Olivier, "Monoslam: Real-time single camera slam", *IEEE transactions on pattern analysis and machine intelligence*, vol. 29, no. 6, pp. 1052–1067, 2007, doi:10.1109/TPAMI.2007.1049.

[18] Pire, Taihú and Fischer, Thomas and Castro, Gastón and De Cristóforis, Pablo and Civera, Javier and Berlles, Julio Jacobo, "S-ptam: Stereo parallel tracking and mapping", *Robotics and Autonomous Systems*, vol. 93, pp. 27–42, 2017, doi:10.1016/j.robot.2017.03.019.

[19] Kerl, Christian and Sturm, Jürgen and Cremers, Daniel, "Dense visual slam for rgb-d cameras", *2013 IEEE/RSJ International Conference on Intelligent Robots and Systems*, pp. 2100–2106, 2013, doi:10.1109/IROS.2013.6696650.

[20] Mur-Artal, Raul and Montiel, Jose Maria Martinez and Tardos, Juan D, "Orb-slam: a versatile and accurate monocular slam system", *IEEE transactions on robotics*, vol. 31, no. 5, pp. 1147–1163, 2015, doi:10.1109/TRO.2015.2463671.

[21] Engel, Jakob and Koltun, Vladlen and Cremers, Daniel, "Direct sparse odometry", *IEEE transactions on pattern analysis and machine intelligence*, vol. 40, no. 3, pp. 611–625, 2017, doi:10.1109/TPAMI.2017.2658577.

[22] Engel, Jakob and Schöps, Thomas and Cremers, Daniel, "Lsd-slam: Large-scale direct monocular slam", *European conference on computer vision*, pp. 834–849, 2014, doi:10.1007/978-3-319-10605-2_54.

[23] Forster, Christian and Pizzoli, Matia and Scaramuzza, Davide, "Svo: Fast semi-direct monocular visual odometry", *2014 IEEE international conference on robotics and automation (ICRA)*, pp. 15–22, 2014, doi:10.1109/ICRA.2014.6906584.

[24] Campos, Carlos and Elvira, Richard and Rodríguez, Juan J Gómez and Montiel, José MM and Tardós, Juan D, "Orb-slam3: An accurate open-source library for visual, visual–inertial, and multimap slam", *IEEE Transactions on Robotics*, 2021, doi:10.1109/TRO.2021.3075644.

[25] Schubert, David and Demmel, Nikolaus and von Stumberg, Lukas and Usenko, Vladyslav and Cremers, Daniel, "Rolling-shutter modelling for direct visual-inertial odometry", *2019 IEEE/RSJ International Conference on Intelligent Robots and Systems (IROS)*, pp. 2462–2469, 2019, doi:10.1109/IROS40897.2019.8968539.

[26] Li, Guangqiang and Yu, Lei and Fei, Shumin, "A deep-learning real-time visual slam system based on multi-task feature extraction network and self-supervised feature points", *Measurement*, vol. 168, p. 108403, 2021, doi:10.1016/j.measurement.2020.108403.

[27] Kang, Rong and Shi, Jieqi and Li, Xueming and Liu, Yang and Liu, Xiao, "Df-slam: A deep-learning enhanced visual slam system based on deep local features", *arXiv preprint arXiv:1901.07223*, 2019.

[28] Li, Ruihao and Wang, Sen and Long, Zhiqiang and Gu, Dongbing, "Undeepvo: Monocular visual odometry through unsupervised deep learning", *2018 IEEE international conference on robotics and automation (ICRA)*, pp. 7286–7291, 2018, doi:10.1109/ICRA.2018.8461251.

[29] Mur-Artal, Raul and Tardós, Juan D, "Orb-slam2: An open-source slam system for monocular, stereo, and rgb-d cameras", *IEEE transactions on robotics*, vol. 33, no. 5, pp. 1255–1262, 2017, doi:10.1109/TRO.2017.2705103.

[30] Campos, Carlos and Elvira, Richard and Rodríguez, Juan J Gómez and Montiel, José MM and Tardós, Juan D, "Orb-slam3: An accurate open-source library for visual, visual–inertial, and multimap slam", *IEEE Transactions on Robotics*, vol. 37, no. 6, pp. 1874–1890, 2021.

[31] Gomez-Ojeda, Ruben and Moreno, Francisco-Angel and Zuniga-Noël, David and Scaramuzza, Davide and Gonzalez-Jimenez, Javier, "Pl-slam: A stereo slam system through the combination of points and line segments", *IEEE Transactions on Robotics*, vol. 35, no. 3, pp. 734–746, 2019, doi:10.1109/TRO.2019.2899783.

[32] Cvišić, Igor and Marković, Ivan and Petrović, Ivan, "Soft2: Stereo visual odometry for road vehicles based on a point-to-epipolar-line metric", *IEEE Transactions on Robotics*, pp. 273–288, 2023, doi:10.1109/TRO.2022.3188121.

[33] Zhou, Yi and Gallego, Guillermo and Shen, Shaojie, "Event-based stereo visual odometry", *IEEE Transactions on Robotics*, 2021, doi:10.1109/TRO.2021.3062252.

[34] Labbé, Mathieu and Michaud, François, "Rtab-map as an open-source lidar and visual simultaneous localization and mapping library for large-scale and long-term online operation", *Journal of Field Robotics*, vol. 36, no. 2, pp. 416–446, 2019, doi:10.1002/rob.21831.

[35] Dai, Angela and Nießner, Matthias and Zollhöfer, Michael and Izadi, Shahram and Theobalt, Christian, "Bundlefusion: Real-time globally consistent 3d reconstruction using on-the-fly surface reintegration", *ACM Transactions on Graphics (ToG)*, vol. 36, no. 4, p. 1, 2017, doi:10.1145/3072959.3054739.

[36] Whelan, Thomas and Kaess, Michael and Fallon, Maurice and Johannsson, Hordur and Leonard, John and McDonald, John, "Kintinuous: Spatially extended kinectfusion", 2012.

[37] Rosinol, Antoni and Abate, Marcus and Chang, Yun and Carlone, Luca, "Kimera: an open-source library for real-time metric-semantic localization and mapping", *2020 IEEE International Conference on Robotics and Automation (ICRA)*, pp. 1689–1696, 2020, doi:10.1109/ICRA40945.2020.9196885.

[38] Bruno, Hudson and Colombini, Esther, "Lift-slam: a deep-learning feature-based monocular visual slam method", *Neurocomputing*, vol. 455, 2021, doi:10.1016/j.neucom.2021.05.027.

[39] "Objectfusion: Accurate object-level slam with neural object priors", *Graphical Models*, vol. 123, p. 101165, 2022, doi:https://doi.org/10.1016/j.gmod.2022.101165.

[40] Qing Li and Rui Cao and Jiasong Zhu and Hao Fu and Baoding Zhou and Xu Fang and Sen Jia and Shenman Zhang and Kanglin Liu and Qingquan Li, "Learn then match: A fast coarse-to-fine depth image-based indoor localization framework for dark environments via deep learning and keypoint-based geometry alignment", *ISPRS Journal of Photogrammetry and Remote Sensing*, vol. 195, pp. 169–177, 2023, doi:https://doi.org/10.1016/j.isprsjprs.2022.10.015.

[41] Zhang, Ji and Singh, Sanjiv, "Loam: Lidar odometry and mapping in real-time.", *Robotics: Science and Systems*, vol. 2, 2014.

[42] Koide, Kenji and Miura, Jun and Menegatti, Emanuele, "A portable 3d lidar-based system for long-term and wide-area people behavior measurement", *IEEE Trans. Hum. Mach. Syst*, 2018, doi:10.1177/1729881419841532.

[43] Chen, Xieyuanli and Milioto, Andres and Palazzolo, Emanuele and Giguere, Philippe and Behley, Jens and Stachniss, Cyrill, "Suma++: Efficient lidar-based semantic slam", *2019 IEEE/RSJ International Conference on Intelligent Robots and Systems (IROS)*, pp. 4530–4537, 2019, doi:10.1109/IROS40897.2019.8967704.

[44] Shan, Tixiao and Englot, Brendan, "Lego-loam: Lightweight and ground-optimized lidar odometry and mapping on variable terrain", *2018 IEEE/RSJ International Conference on Intelligent Robots and Systems (IROS)*, pp. 4758–4765, 2018, doi:10.1109/IROS.2018.8594299.

[45] Shan, Tixiao and Englot, Brendan and Meyers, Drew and Wang, Wei and Ratti, Carlo and Rus, Daniela, "Lio-sam: Tightly-coupled lidar inertial odometry via smoothing and mapping", *2020 IEEE/RSJ International Conference on Intelligent Robots and Systems (IROS)*, pp. 5135–5142, 2020, doi:10.1109/IROS45743.2020.9341176.

[46] Montemerlo, Michael and Thrun, Sebastian and Koller, Daphne and Wegbreit, Ben and others, "Fastslam: A factored solution to the simultaneous localization and mapping problem", *Aaai/iaai*, vol. 593598, 2002.

[47] Grisetti, Giorgio and Stachniss, Cyrill and Burgard, Wolfram, "Improved techniques for grid mapping with rao-blackwellized particle filters", *IEEE transactions on Robotics*, vol. 23, no. 1, pp. 34–46, 2007, doi:10.1109/TRO.2006.889486.

[48] Konolige, Kurt and Grisetti, Giorgio and Kümmerle, Rainer and Burgard, Wolfram and Limketkai, Benson and Vincent, Regis, "Efficient sparse pose adjustment for 2d mapping", *2010 IEEE/RSJ International Conference on Intelligent Robots and Systems*, pp. 22–29, 2010, doi:10.1109/IROS.2010.5649043.

[49] Hess, Wolfgang and Kohler, Damon and Rapp, Holger and Andor, Daniel, "Real-time loop closure in 2d lidar slam", *2016 IEEE International Conference on Robotics and Automation (ICRA)*, pp. 1271–1278, 2016, doi:10.1109/ICRA.2016.7487258.

[50] Konolige, Kurt and Grisetti, Giorgio and Kümmerle, Rainer and Burgard, Wolfram and Limketkai, Benson and Vincent, Regis, "Efficient sparse pose adjustment for 2d mapping", *2010 IEEE/RSJ International Conference on Intelligent Robots and Systems*, pp. 22–29, 2010, doi:10.1109/IROS.2010.5649043.

[51] Kohlbrecher, Stefan and Von Stryk, Oskar and Meyer, Johannes and Klingauf, Uwe, "A flexible and scalable slam system with full 3d motion estimation", *2011 IEEE international symposium on safety, security, and rescue robotics*, pp. 155–160, 2011, doi:10.1109/SSRR.2011.6106777.

[52] Lv, Wenjun and Kang, Yu and Qin, Jiahu, "Indoor localization for skid-steering mobile robot by fusing encoder, gyroscope, and magnetometer", *IEEE Transactions on Systems, Man, and Cybernetics: Systems*, vol. 49, no. 6, pp. 1241–1253, 2017, doi:10.1109/TSMC.2017.2701353.

[53] Jiang, Ping and Chen, Liang and Guo, Hang and Yu, Min and Xiong, Jian, "Novel indoor positioning algorithm based on lidar/inertial measurement unit integrated system", *International Journal of Advanced Robotic Systems*, vol. 18, no. 2, p. 1729881421999923, 2021, doi:10.1177/1729881421999923.

[54] Ismail, Zool H and Bukhori, Iksan, "Efficient detection of robot kidnapping in range finder-based indoor localization using quasi-standardized 2d dynamic time warping", *Applied Sciences*, vol. 11, no. 4, p. 1580, 2021, doi:10.3390/app11041580.

[55] Zhang, Lei, "Self-adaptive markov localization for single-robot and multi-robot systems", Ph.D. thesis, Université Montpellier II-Sciences et Techniques du Languedoc, 2010.

[56] Zhang, Lei and Zapata, Rene and Lepinay, Pascal, "Self-adaptive monte carlo localization for mobile robots using range finders", *Robotica*, vol. 30, no. 2, pp. 229–244, 2012, doi:10.1017/S0263574711000567.

[57] Zhang, Lei and Zapata, René and Lépinay, Pascal, "Self-adaptive monte carlo localization for mobile robots using range sensors", *2009 IEEE/RSJ International Conference on Intelligent Robots and Systems*, pp. 1541–1546, 2009, doi:10.1109/IROS.2009.5354298.

[58] Zhang, Lei and Zapata, René, "A three-step localization method for mobile robots", *Proceedings of International Conference on Automation, Robotics and Control Systems (ARCS 2009)*, pp. 50–56, 2009.

[59] Zhang, Lei and Zapata, René, "Probabilistic localization methods of a mobile robot using ultrasonic perception system", *2009 International Conference on Information and Automation*, pp. 1062–1067, 2009, doi:10.1109/ICINFA.2009.5205075.

[60] Yu, Wei and Li, Jie and Yuan, Jing and Ji, Xi, "Indoor mobile robot positioning based on uwb and low cost imu", *2021 IEEE 5th Advanced Information Technology, Electronic and Automation Control Conference (IAEAC)*, vol. 5, pp. 1239–1246, 2021, doi:10.1109/IAEAC50856.2021.9390754.

[61] Liu, Jianfeng and Pu, Jiexin and Sun, Lifan and He, Zishu, "An approach to robust ins/uwb integrated positioning for autonomous indoor mobile robots", *Sensors*, vol. 19, no. 4, p. 950, 2019, doi:10.3390/s19040950.

[62] Cui, Wei and Liu, Qingde and Zhang, Linhan and Wang, Haixia and Lu, Xiao and Li, Junliang, "A robust mobile robot indoor positioning system based on wi-fi", *International Journal of Advanced Robotic Systems*, vol. 17, no. 1, p. 1729881419896660, 2020, doi:10.1177/1729881419896660.

[63] Motroni, Andrea and Nepa, Paolo and Buffi, Alice and Tellini, Bernardo, "Robot localization via passive uhf-rfid technology: State-of-the-art and challenges", *2020 IEEE International Conference on RFID (RFID)*, pp. 1–8, 2020, doi:10.1109/RFID49298.2020.9244884.

[64] Bernardini, Fabio and Buffi, Alice and Fontanelli, Daniele and Macii, David and Magnago, Valerio and Marracci, Mirko and Motroni, Andrea and Nepa, Paolo and Tellini, Bernardo, "Robot-based indoor positioning of uhf-rfid tags: The sar method with multiple trajectories", *IEEE Transactions on Instrumentation and Measurement*, vol. 70, pp. 1–15, 2020, doi:10.1109/TIM.2020.3033728.

[65] Al-Forati, Israa Sabri Abdulameer and Rashid, Abdulmuttalib, "Design and implementation an indoor robot localization system using minimum bounded circle algorithm", *2019 8th International Conference on Modeling Simulation and Applied Optimization (ICMSAO)*, pp. 1–6, 2019, doi:10.1109/ICMSAO.2019.8880404.

[66] Alfurati, IS and Rashid, Abdulmuttalib T, "An efficient mathematical approach for an indoor robot localization system", *Iraqi Journal of Electrical and Electronic Engineering*, vol. 15, no. 2, pp. 61–70, 2019, doi:10.37917/ijeee.15.2.7.

[67] Albuquerque, Daniel F and Gonçalves, Edgar S and Pedrosa, Eurico F and Teixeira, Francisco C and Vieira, José N, "Robot self position based on asynchronous millimetre wave radar interference", *2019 International Conference on Indoor Positioning and Indoor Navigation (IPIN)*, pp. 1–6, 2019, doi:10.1109/IPIN.2019.8911809.

[68] Perez-Grau, Francisco J and Caballero, Fernando and Viguria, Antidio and Ollero, Anibal, "Multi-sensor three-dimensional monte carlo localization for long-term aerial robot navigation", *International Journal of Advanced Robotic Systems*, vol. 14, no. 5, p. 1729881417732757, 2017.

[69] Chen, Xieyuanli and Läbe, Thomas and Nardi, Lorenzo and Behley, Jens and Stachniss, Cyrill, "Learning an overlap-based observation model for 3d lidar localization", *2020 IEEE/RSJ International Conference on Intelligent Robots and Systems (IROS)*, pp. 4602–4608, IEEE, 2020.

[70] Wolfgang Hess and Damon Kohler and Holger Rapp and Daniel Andor, "Real-time loop closure in 2d LIDAR SLAM", *2016 IEEE International Conference on Robotics and Automation, ICRA 2016, Stockholm, Sweden, May 16-21, 2016*, pp. 1271–1278, IEEE, 2016, doi:10.1109/ICRA.2016.7487258.

[71] Koki Aoki and Kenji Koide and Shuji Oishi and Masashi Yokozuka and Atsuhiko Banno and Junichi Meguro, "3d-bbs: Global localization for 3d point cloud scan matching using branch-and-bound algorithm", *CoRR*, vol. abs/2310.10023, 2023, doi:10.48550/ARXIV.2310.10023.